Title
The specific heat of pure and hydrogenated amorphous silicon

Author
Queen, Daniel Robert

Publication Date
2011

Peer reviewed|Thesis/dissertation

The specific heat of pure and hydrogenated amorphous silicon

by

Daniel Robert Queen

A dissertation submitted in partial satisfaction of the

requirements for the degree of

Doctor of Philosophy

in

Physics

in the

Graduate Division

of the

University of California, Berkeley

Committee in charge:

Professor F. Hellman, Chair

Professor S. G. Louie

Professor J.A. Reimer

Fall 2011

The specific heat of pure and hydrogenated amorphous silicon

Abstract

The specific heat of pure and hydrogenated amorphous silicon

by

Daniel Robert Queen

Doctor of Philosophy in Physics

University of California, Berkeley

Professor F. Hellman, Chair

At low temperature, amorphous materials have low energy excitations that result in a heat capacity that is in excess of the Debye heat capacity calculated from the sound velocity [1]. These excitations are ubiquitous to the glassy state and occur with roughly the same density for all glasses [2]. The specific heat has a linear temperature dependence below 1K that has been described by the phenomenological two-level systems (TLS) model [3, 4] in addition to a T^3 temperature dependence which is in excess of the T^3 Debye specific heat. It is still unknown what exact mechanism gives rise to the TLS but it is assumed that groups of atoms have configurations that are close in energy and, at low temperature, these atoms can change configurations by tunneling through the energy barrier separating them. It has been an open question as to whether tetrahedrally bonded materials, like amorphous silicon, can support TLS due to the over-constrained nature of their bonding.

It is shown in this work that amorphous silicon (*a*-Si) and hydrogenated amorphous silicon (*a*-Si:H) have specific heat C_P in excess of the Debye specific heat which depends on the details of the growth process. There is a linear term that is due to TLS in addition to an excess T^3 contribution. We find that the TLS density depends on number density of atoms in the *a*-Si film and that the presence of hydrogen in *a*-Si:H increases C_P further. We suggest that regions of low density are sufficiently under-constrained to support tunneling between structural configurations at low temperature as described by the TLS model. The presence of H further lowers the energy barriers for the tunneling process resulting in an increase in TLS density in *a*-Si:H. The presence of H in *a*-Si:H network is found to be metastable. Annealing causes H to diffuse away from clustered regions which reduces the density of TLS. A low temperature anomaly is found in the *a*-Si:H films in their as prepared state that is of unknown origin but appears to take the form of a broadened Schottky anomaly. This feature is removed upon annealing. We find that there is a clear link between density of TLS and the excess T^3 heat capacity. This correlation is not currently addressed by models of the glassy state.

Additionally, a reversible increase in the heat capacity is found upon light soaking in both *a*-Si and *a*-Si:H. This increase occurs over the entire measured temperature range $2 - 300$K and can be removed by annealing at 200°C. The light soaked heat capacity at low temperatures has the form of the low energy excitations that are found in glasses. We suggest that the dangling bond defects responsible for the Staebler-Wronski effect are a consequence of the photo-induced structural states.

To Karen and Grey

Contents

List of Figures **iv**

List of Tables **xii**

1 Introduction **1**

2 Previous Work **4**
2.1 Low-temperature properties of glasses 4
2.2 Two-level systems model 5
2.3 Literature summary of TLS in amorphous silicon 7
2.4 Staebler-Wronski Effect 9

3 Survey of experimental methods **10**
3.1 Thin film growth techniques 10
3.1.1 Electron beam evaporation 10
3.1.2 Hot-wire chemical vapor deposition 10
3.2 Materials Characterization 11
3.2.1 Raman Scattering 11
3.2.2 Ion-beam Analysis 11
3.2.3 Sound velocity and thermal conductivity 11
3.2.4 Internal Friction 12
3.2.5 Electron spin resonance 13
3.3 Calorimetry 13
3.3.1 Sample preparation 13
3.3.2 Patterning samples on the calorimeter 14
3.3.3 Measurement Apparatus 14
3.3.4 Light-soaking 14
3.3.5 Annealing 15

4 Thin-film nanocalorimetry **16**
4.1 Introduction 16
4.2 Device Description 17
4.3 Fabrication 19
4.4 Experimental Method 21
4.5 Results 25

4.6 Conclusions 30

5 Specific heat of electron beam evaporated amorphous silicon 31
5.1 Introduction 31
5.2 Experimental Procedure 33
5.3 Results 34
5.4 Discussion 47
5.5 Conclusions 51

6 Specific heat of hydrogenated amorphous silicon prepared by the hot-wire CVD technique 53
6.1 Introduction 53
6.2 Experimental Procedure 55
6.3 Results 57
6.4 Discussion 70
6.5 Conclusions 72

7 Light induced thermodynamic metastability in amorphous silicon 74
7.1 Introduction 74
7.2 Experimental Procedure 75
7.3 Results 76
7.4 Discussion 84
7.5 Conclusions 86

8 Conclusions 87

Bibliography 90

A Surface roughness of silicon nitride membranes 100
A.1 Sample Preparation 100
A.2 Experimental procedure 101
A.3 Results and Discussion 101
A.4 Conclusions 103

List of Figures

2.1 Specific heat and thermal conductivity of α-quartz and vitreous silica (a-SiO_2) from Ref. [1]. The Debye specific heats (- - -) are calculated from the sound velocity. 5

3.1 Raman scattering for crystalline and amorphous silicon. The peak at 521cm^{-1} is the first order Raman mode in crystalline silicon. The Raman spectrum of a-Si is proportional to the phonon DOS. The upturn in the spectrum below 75cm^{-1} is due to Rayleigh scattered light from the laser. 12

4.1 Schematic of the nanocalorimeter. (a) The sample and conduction layer are in the 1×1 mm^2 square at the center of the 2×2 mm^2 membrane. The silicon chip is 5×5 mm^2. Three sample thermometers (two a-Nb_ySi_{1-y} and one Pt) are located on the sample area with impedance matched thermometers on the frame. Each thermometer's resistance is optimized for a different temperature range. A Pt sample heater is used for all T_0 to heat the sample area with respect to the frame. Lead resistances are <2% of the measured resistance for the heater and over the range of each thermometer. The Pt heater and thermometer are 12 μm wide. The a-Nb_ySi_{1-y} thermometers have the same doping y and resistances that differ by a factor of 12.5 due to geometry. (b) The 30-50 nm thick low stress, amorphous Si-N membrane is released by etching the Si wafer in KOH and then removing the 100 nm oxide layer in buffered HF. The 10-20 nm thick Pt film is lithographically patterned and etched prior to releasing the membrane. a-Nb_ySi_{1-y} is deposited on the wafer with released membranes, patterned, and then etched. The sample is patterned in the center of the membrane by depositing the film through a separately micromachined deposition mask. 18

4.2 Low temperature sensitivity figure of merit FOM = $\left(\frac{t}{t_{th}}\right)^{1/2} \frac{T^{3/2}}{\rho^{1/2}} \frac{\mathrm{d}\rho}{\mathrm{d}T}$ of the nanocalorimeter using a-Nb_ySi_{1-y} thermometers. The predicted nanocalorimeter FOM (solid line) which is the same as the microcalorimeter, FOM for $\frac{t}{t_{th}} = \frac{1}{6}$ and $\rho = constant$ (dashed line), and the measured FOM with $\frac{t}{t_{th}} = constant$ and ρ decreased to reduce the thermometer resistance below 1MΩ. 20

4.3 Total measured heat capacity c_T of a 50 nm thick device with 86.4 nm of Cu [contributions from: Cu conduction layer; Si-N membrane; Pt heater, thermometer, and leads; and a-Nb_ySi_{1-y} thermometers (small and not shown)]. c_{Cu} and c_{Pt} are calculated from bulk data [5]. c_{Si-N} is calculated from $c_T - c_{Cu} - c_{Pt}$. [6] 22
4.4 Measured total thermal link $K = P/\Delta T$ of a 50 nm nanocalorimeter shown with the contributions from Si-N membrane, Pt leads, and radiation. K_{Pt} is calculated using the Wiedemann-Franz law with the measured $\sigma(T)$ of the Pt heater. K_{Si-N} is calculated by subtracting the contributions from Pt leads and radiation. K_{rad} is taken as the T^3 term in $K - K_{Pt}$. [6] Inset: K for two devices from different wafers in same process lot. 24
4.5 Specific heat of Cu (a) and Au (b) films of various thicknesses. Bulk values (solid lines) are from Ref. [5]. Data in (a) is the difference between devices with thick and thin Cu films. The specific heat of Au (b) was determined as described in the text. Insets: C/T vs. T^2 for 56.1 nm Cu (a) and 56.3 nm Au (b). 26
4.6 Thermal conductivity (a) from 50 nm Si-N membranes (◆) compared to values for 200 nm membranes (□) grown in the same furnace as the 50 nm membranes and previously reported 200nm films (circles and triangles) [6]. Room temperature values for 200 nm (×) and 50 nm (+) are measured by the time-domain thermoreflectance technique [7]. Specific heat (b) from 50 nm (◆) and 200 nm (□) Si-N membranes. 28
4.7 Reduced specific heat (J mol^{-1} K^{-1}) of silicon nitride (50 nm, 200 nm) and vitreous silica [1] plotted as $C_P \times (\theta_D/T)^3$ versus reduced temperature T/θ_D. The dashed line is the Debye specific heat. Debye temperatures were calculated from the measured sound velocities [8, 7, 1] 29

5.1 Raman scattering spectra for a-Si measured at room temperature with the Rayleigh scattered light subtracted. The film thicknesses are $\sim$ 3000Å. The TA-like modes result in the Boson peak at 150cm^{-1} and the TO-like peak is visible at 475cm^{-1}. The TO and LA peaks sharpen with increasing T_S indicating that the local structural order in the film is increasing. The bond angle disorder is obtained by fitting the half-width of the TO-like peak as described in the text and shown in Table 5.1. There is no significant change in the TA peak with T_S. 36

5.2 RBS spectra for films grown on MgO substrates at (a) 45°C and (b) 200°C as a function of incident energy E_0. The silicon number density in the film is determined from the area of the silicon peak which has an onset energy ~ 1750keV. By setting the energy to $E_0 = 3.040$MeV α-particles resonantly scatter from oxygen in the top ~ 50Å of the film. Increasing E_0 probes deeper in the bulk of the film at the oxygen resonant energy by compensating for the energy loss of the α-particles as they interact with the electrons in the film. The 45°C film has $\sim 2\%$ oxygen throughout the bulk of the film while the 200°C sample has only an oxide layer near the surface. Only a $\sim 10 - 30$Å surface layer can be attributed to a-SiO_2 and the remainder is due to an oxygen concentration gradient in the bulk of the film. 37

5.3 RBS Oxygen spectra for a-Si grown on MgO at 45°C (2775Å), 200°C (3191Å), and 400°C (1497Å) with the incident energy at the oxygen resonance $E_0 =$ 3.040MeV. The oxygen spectrum is obtained by subtracting the model data for Si and Mg from the measured spectrum. The resonant peak is due to oxygen near the surface of the film. Films grown at higher temperature are found to have a higher Si density and lower oxygen content. The oxygen in the bulk of the film is measured by increasing E_0 as is shown in Fig. 5.2. The vertical arrows indicate the onset of the oxygen signal from the MgO substrate which shifts to lower energy due to increased energy loss in the thicker a-Si films. 38

5.4 RBS oxygen spectra for a-Si grown on MgO at (a) 45°C and (b) 200°C for several different film thicknesses. The 4150Å film is the sample from Ref. [9] which only has a film is a 30Å surface layer of SiO_2 with no oxygen detected in the bulk of the film. This film is grown on a Si-N substrate and does not have an oxygen signal from the substrate. In the films prepared for this study the oxygen content decreases with increasing T_S. 39

5.5 Internal friction Q^{-1} for several ~ 3000Å evaporated a-Si films measured at 5500Hz. The plateau below 10K is due to those TLS with the appropriate energy splitting to scatter acoustic waves. Also shown is Q^{-1} from Ref. [10] for an e-beam evaporated a-Si film grown at room temperature (dashed line) and the same film after annealing at 350°C for 5h (dotted line). 42

5.6 The transverse and longitudinal sound velocity of a-Si compared to the average of the [100] and [110] longitudinal (dashed line) and transverse (dotted line) sound velocities of crystalline silicon calculated from the elastic constants [11]. v_t (■) was determined from the shear modulus G and density ρ and are listed in Table 5.1. v_l was measured by an ultrasonic picosecond acoustic technique [12] v_l are shown for the thin (◇) and thick (▲) samples listed in Table 5.3. v_l for the sample from Ref. [9] is shown for comparison (●). 43

5.7 The Debye temperature θ_D as a function of growth temperature T_S for the thin ($\triangle$) and thick ($\blacklozenge$) a-Si films listed in Table 5.3. The Debye temperature is calculated from the measured transverse and longitudinal sound velocities and the total number density from RBS. Using only the silicon number density changes θ_D by $< 5\%$. The error bars are due to the uncertainties in film thickness and RBS areal density. The Debye temperature of crystalline silicon (- - -) with $\theta_D = 645$K and the film from Ref. [9] ($\blacksquare$) with $\theta_D = 487$K are shown for comparison. 44

5.8 Specific heat of ~ 3000Å thick a-Si films plotted as C/T^3 versus T for several growth temperatures. Only representative error bars are shown for clarity. The Debye heat capacities were calculated from the measured sound velocity as described in the text and at low temperature appear as a constant on this plot. The calculated θ_D are listed in the figure. The data for a-Si from Ref [9] (dashed-dotted line) and crystalline silicon (solid line) are shown as a reference [5]. $\theta_D = 645$K for crystalline silicon. The specific heat of the 45°C and 200°C films is in excess of the Debye specific heat as is typical of an amorphous material while the 400°C sample is comparable to its Debye specific heat. The vertical arrow identifies the location of the Boson peak which shows no substantial dependence on T_S. 45

5.9 The specific heat of thick and thin films of a-Si grown at (a) 200°C and (b) 45°C. Closed symbols are as-prepared films. Only representative error bars are shown for clarity. The 200°C (3191Å) and 45°C (2775Å) films were annealed at 200°C (open symbols) for 10^4s. Annealing the 3191Å45°C at 200°C resulted in a decrease in n_0 by a factor of 2.5 but c_{ex} changed by less than 2%. Changes in the specific heat of the $T_S = 200$°C film after annealing were negligible. Also shown are the Debye specific heats (dashed line) calculated from the sound velocities of the ~ 3000Å thick films. The data from Ref [9] are shown for comparison (solid line) which has film density ρ comparable to the 400°C sample (not shown) as seen in Table 5.3. A linear temperature dependence is shown for comparison (dotted line). 46

5.10 Heat capacity of the 2775Å film grown at $T_S = 45$°C plotted as C/T^3 compared to the heat capacity of a-SiO_2 assuming all of the oxygen in the film is in the form of a-SiO_2. The film is shown before ($\blacksquare$) and after ($\square$) subtracting the calculated heat capacity of a-SiO_2 (solid line). The bulk heat capacity of a-SiO_2 is from Ref. [1]. 48

5.11 Specific heat fitting parameters n_0 ($\blacksquare$) and $c_{ex} = c_3 - c_{Debye}$ ($\bigcirc$) as a function of the Si number density as determined from RBS illustrating the correlation between the excess heat capacity and the silicon number density. There is no correlation when n_0 and c_{ex} are plotted against oxygen content. The lines are a guide to the eye. Inset: $\overline{P}\gamma^2$ from Q^{-1} plotted versus the silicon number density. 49

5.12 n_0 and c_{ex} determined from fits to the specific heat as described in the text. The data are identified by growth temperature 45°C (■), 200°C (▲), and 400°C (●). Open symbols are annealed samples. n_0 is the density of two-level systems (TLS) that are responsible for the linear heat capacity in amorphous materials. $c_{ex} = c_3 - c_{deb}$ is the excess T^3 specific heat presumably due to localized harmonic excitations. 50

6.1 Longitudinal sound velocity measured at room temperature for several 700Å (▲) and 6000Å (■) thick HWCVD *a*-Si:H films prepared at NREL as a function of growth temperature T_S. The data from Ref. [13] for ∼ 2000 HWCVD films grown at UIUC (▽) are shown for comparison. The average longitudinal sound velocity of crystalline silicon is shown as a reference (- - -). The error bars are due to the uncertainty in the film thickness. 58

6.2 Room temperature thermal conductivity of 6000Å HWCVD *a*-Si:H films (■) prepared at NREL as a function of growth temperature T_S from this work. Shown for comparison are HWCVD films from UIUC (○) and NREL (△) from Ref. [13]. The two high thermal conductivity films are the low Q^{-1} films from Ref. [14]. 59

6.3 Specific heat of as-deposited HWCVD *a*-Si:H films for various growth temperatures. Plotted as (a) C/T^3 versus T to show the deviation from the Debye heat capacity and (b) C/T versus T^2 to show the sublinear temperature dependence. The error bars for the HWCVD samples are the same size as the data points and not shown. Increasing growth temperature corresponds to decreasing H content as shown in Table 6.1. Shown for comparison are the specific heats of c-Si [5], *a*-SiO_2 [1], and e-beam evaporated *a*-Si grown at $T_S = 400$°C (◇). The dashed lines in (a) are the maximum and minimum Debye heat capacities for the *a*-Si:H films shown and have been calculated from the measured longitudinal sound velocity as described in the text. The solid lines in (b) are a fit to Eq. 6.2 for the HWCVD films and Eq. 6.1 for the *e*-beam film. 61

6.4 Specific heat of *a*-Si:H prepared at various T_S after annealing at $T_A = 200$°C. Only representative error bars are shown for clarity. Shown for comparison are the specific heats of c-Si [5], *a*-SiO_2 [1], and e-beam evaporated *a*-Si grown at $T_S = 400$°C (◇). The dashed lines are the maximum and minimum Debye heat capacities for the *a*-Si:H films shown and have been calculated from sound velocity as described in the text. The $T_S = 430$°C and 370°C films were fast quenched and the 300° film was slow cooled from $T_A = 200$°C. The dashed lines in (a) are the maximum and minimum Debye heat capacities for the *a*-Si:H films shown and have been calculated from sound velocity as described in the text. The solid lines in (b) are a fit to Eq. 6.1. 62

6.5 n_{Sch} versus T_S for as-prepared HWCVD films determined from the fit to Eq. 6.2. 63

6.6 Specific heat of a HWCVD a-Si:H film grown at (a) $T_S = 430°$C (4 at.% H) and (b) $T_S = 370°$C (7 at.% H) in the as-prepared (■) and 200°C (●) and 300°C (▲)annealed states. The film was either fast-quenched (open symbols) or slow-cooled (closed symbols) after annealing as described in the text. The insets show the same data at high temperature on a linear scale. The Debye specific heat (- - -) is calculated from sound velocity measurements. The line labeled T is for comparison to a linear temperature dependence. 64

6.7 Specific heat of a HWCVD a-Si:H film grown at $T_S = 430°$C (4 at.% H) plotted as C/T versus T^2 in the unannealed (■) and 200°C (●) and 300°C (▲) annealed states. The film was either fast-quenched (open symbols) or slow-cooled (closed symbols) after annealing as described in the text. The Debye specific heat (- - -) is calculated from sound velocity measurements. All of the as-prepared films have a low temperature anomaly that has been fit to a Schottky anomaly. The as-prepared state is fit to Eq. 6.2 and is shown as the solid line through the data. The two contributions to the fit are also show separately and are labeled C_{Sch} for the Schottky term and $C_G = c_1T + c_3T^3$ for the glass term. There was no decrease in the total hydrogen content or density after annealing as measured by HFS and RBS. The annealed films are fit to Eq. 6.1 and the fit to the 200°C slow cooled state is shown. 65

6.8 Q^{-1}_{film} of a 1μm thick HWCVD a-Si:H film grown at $T_S = 370°$C and measured with the antisymmetric mode of the double paddle oscillator at 5500Hz. The film is measured in the as-prepared and 200°C annealed states. The NREL run number for this film is T3536. 67

6.9 (a) n_0 and (b) c_{ex} versus total film density n as determined from RBS for HWCVD films in the as-prepared (■) fit to Eq. 6.2 and annealed states: 200°C (●) and 300°C (▲) fit to Eq. 6.1. The data point labels identify the values from Table 6.2. Open symbols correspond to fast quenching through T_E. n_0 is determined from the linear term in the specific heat and $c_{ex} = c_3 - c_{Debye}$ is the excess T^3 specific heat that is not due to phonons. 68

6.10 n_0 versus c_{ex} as determined from fits to the low temperature heat capacity as explained in the text. HWCVD films in the as-prepared (blue) and annealed (black) states are shown along with values for e-beam evaporated (red) films. The data are for films in the as-prepared (■) and annealed states: 200°C (●) and 300°C (▲). The data point labels identify the values from Table 6.2. Open symbols correspond to fast quenching through T_E. n_0 is determined from the linear term in the specific heat and $c_{ex} = c_3 - c_{Debye}$ is the excess T^3 specific heat that is not due to phonons. 69

7.1 Heat capacity of a-Si:H grown by the HWCVD at (a) $T_S = 430°$C (4 at.% H) and (b) $T_S = 370°$C in the as-prepared, light soaked and annealed states. The film was either slow cooled (◆) by a controlled current ramp of the sample heater on the device or fast quenched (▲) by setting the sample heater current to zero. The photo and thermal treatments were performed in the order given in the legend. The Debye T^3 heat capacity (dashed line) is calculated from the measured longitudinal sound velocity as explained in the text and is assumed not to change upon light soaking and annealing. Crystalline silicon (heavy solid line) is shown as a reference [5]. The line labeled T is shown for comparison of the temperature dependence and is not a fit. The mole is defined as a mole of SiH_x where x is the hydrogen content in the film. The atomic density is determined from RBS. 77

7.2 Heat capacity of an evaporated a-Si film grown at $T_S = 45°$C. The thermal and photo treatments were performed in the order listed in the legend. The film was cooled at 5K/min after annealing. The Debye heat capacity (dashed line) is calculated from the measured sound velocity. Crystalline silicon [5] and the as-prepared HWCVD film ($T_S = 430°$C) from Fig. 7.1 (heavy solid lines) are shown for reference. The line labeled T is shown for comparison of the temperature dependence and is not a fit. The mole is defined as a mole of SiO_x where x is the average concentration of oxygen in the film. The atomic density is determined from RBS. 78

7.3 The high temperature specific heat of HWCVD a-Si:H grown at $T_S = 430°$C and e-beam evaporated a-Si (inset) grown at $T_S = 45°$C. The order of the thermal and photo treatments is given in the legend. 79

7.4 The excess specific heat $\Delta C = C^{LS} - C^{Initial}$ between the light soaked and initial states of HWCVD a-Si:H ($T_S = 430°$C and 370°C) and evaporated a-Si ($T_S = 45°$C and 200°C) upon light soaking. ΔC below 7K for the as-prepared $T_S = 430°$C is no dominated by error due to the large signal from the clustered H and is not shown. Samples were light soaked through the transparent membrane of the nanocalorimeter for 7 days under an AM1.5G solar simulator. The lines labeled T and T^3 are shown as a reference for the temperature dependence and are not fits. 81

7.5 The change in (a) n_0 and (b) c_{ex} between the initial and light soaked states as a function of their initial values. The data points are identified by the labels given in Table 7.1. There is large uncertainty in n_0 and c_{ex} for the as-prepared HWCVD films due to the low temperature anomaly and the data is not shown. The annealed e-beam films were not light soaked. 82

7.6 Δn_0 versus Δc_{ex} after light soaking (green) showing that light soaking increases the density of glassy excitations. The data points are identified by the labels given in Table 7.1 with the unprimed numbers identifying the initial state and the primed numbers the change upon light soaking. Shown on the same scale is n_0 versus c_{ex} for the HWCVD films in the as-prepared (blue) and annealed (black) states along with the e-beam evaporated (red) films. The data are for films in the as-prepared (■) and annealed states: $T_A = 200°C$ (●) and 300°C (▲). Open symbols correspond to fast quenching as described in Chapter 6. n_0 is determined from the linear term in the specific heat and $c_{ex} = c_3 - c_{Debye}$ is the excess T^3 specific heat that is not due to phonons. There is large uncertainty in n_0 and c_{ex} for the as-prepared HWCVD films due to the low temperature anomaly and the data is not shown. The annealed e-beam films were not light soaked. 83

7.7 Magnetic field dependent specific heat of a-Si grown at $T_S = 45°C$ in 4T (●) and 8T (○) along with a-Si:H grown at $T_S = 430°C$ in 8T (□). The a-Si:H film was measured in field after the second light soaking step shown in Fig. 7.1. 84

8.1 Specific heat of HWCVD a-Si:H and e-beam evaporated a-Si are plotted as C/T^3 versus T. The HWCVD sample was grown at $T_S = 430°C$ and is shown in the as-prepared and the 200°C annealed states. The annealed film is shown both before and after light soaking. The evaporated films shown were grown at $T_S = 45°C$ and 400°C. The films grown at $T_S = 45°C$ are shown for two thicknesses: 1120Å (1.98 g/cm^3) and 2775Å (2.08 g/cm^3). The 2775Å film is shown in the as-prepared and light soaked states. The $T_S = 400°C$ film (2.09 g/cm^3) is in the as-prepared state. The dashed lines are the maximum and minimum Debye heat capacities for the samples shown. The Debye specific heats are calculated from the sound velocity. The maximum Debye specific heat ($\theta_D = 480K$) is from the 2775Å $T_S = 45°C$ evaporated a-Si film. The minimum Debye specific heat ($\theta_D = 620K$) is from the $T_S = 400°C$ evaporated a-Si film. $\theta_D = 570K$ for the HWCVD film. Crystalline silicon is shown as well ($\theta_D = 645K$) [5]. 88

List of Tables

5.1 Summary of data for Q^{-1} and Raman scattering samples. Samples are identified by run number. T_S is the growth temperature. t is the sample thickness. ρ is the density. G is the shear modulus determined during the Q^{-1} measurements. The values of Q^{-1} at 2K are listed. The transverse sound velocity v_t is calculated from G as described in the text. Γ is the width at half maximum of the TO-like peak in Raman scattering and $\Delta\theta$ is the calculated bond angle deviation. 35

5.2 Results from fits to the RBS spectra using SIMNRA. Samples are identified by run number. T_S is the growth temperature. t is the total film thickness. The data were modeled as multiple layers with decreasing oxygen content with layer 1 at the top and composed of SiO_2. The relative silicon and oxygen concentrations for a model layer are given along with the thickness of the layer t_l. The average number density of the film was used to calculate the model layer thicknesses. ρ is the mass density of the film and n_{Si} is the silicon number density. 41

5.3 Summary of data for heat capacity samples. T_S is the growth temperature. t is the sample thickness. ρ is the mass density determined from RBS and thickness measurements. v_l is the longitudinal sound velocity determined from picosecond acoustic measurements. θ_D is the Debye temperature calculated from the sound velocity. n_0 is the density of states of TLS as determined from heat capacity measurements. $c_{ex} = c_3 - c_{Debye}$ is the excess T^3 specific heat as explained in the text. n_{ESR} is the dangling bond defect density from ESR measurements. Sample T03-09 is the a-Si film reported in Ref. [9]. . . 47

6.1 HWCVD *a*-Si:H results summary for 700Å samples. Samples are identified by their NREL run number. T_S is the substrate temperature during growth. v_l is the longitudinal sound velocity measured by the picosecond ultrasonic pump-probe technique. n_{Si} is the silicon number density determined from RBS. c_H is the hydrogen content determined from growth calibration and verified by RBS. n is the total number density and ρ is the mass density which are both calculated from n_{Si} and c_H. For crystalline silicon $n_{Si} = 5.00 \times 10^{22}$ atoms/cm^3 and $\rho = 2.33$g/cm^3. The error on c_H is $\pm 1\%$ and is estimated from the relative difference in the intensity of the hydrogen peak HFS as compared to the expected differences from the growth calibration. An absolute measure of c_H was not possible due to charging of the mylar film in the HFS detector. 57

6.2 Summary of HWCVD *a*-Si:H heat capacity results. The data for *a*-SiO2 are taken from Ref. [2]. The samples are identified by the NREL run number. The sample state is listed as either the as-prepared state (i), the slow-cooled state (s), or the fast-quenched state (f). Samples are listed in the order that they were annealed. T_S is the growth temperature. T_A is the annealing temperature. P is the power applied to the sample heater during the anneal. T_b is the temperature of the sample block during the anneal. θ_D is the Debye temperature calculated from the measured longitudinal sound velocity and density for the as-prepared state as described in the text. c_{Debye} was assumed not to change upon annealing and these values are shown in parenthesis. n_0 is the density of TLS determined from the linear term in the specific heat. $c_{ex} = c_3 - c_{Debye}$ is the excess T^3 specific heat that is not due to phonons. n_{Sch} is the density of systems in the as-prepared films with energy splitting δ assuming that anomaly can be modeled as a Schottky anomaly. The as-prepared films were fit to Eq. 6.2 and the annealed films were fit to Eq. 6.1. 66

7.1 Summary of low temperature heat capacity results from fits to Eq. 7.1. The unannealed *a*-Si:H films were fit to a modified form of Eq. 7.1 that includes a Schottky anomaly and is described in Chapter 6. Samples are identified by their run number, preparation technique, and the initial state before light soaking: as-prepared (AP) or annealed (AN) at 200°C. The labels identify the data points in the figures. The state of the sample is listed in the order that the light soaking and annealing occurred. T_S is the substrate temperature during growth. c_{Debye} is the Debye heat capacity calculated from the measured sound velocity as described in the text and values shown in parenthesis have been assumed not to change upon light soaking and annealing. n_0 is the density of TLS and $c_{ex} = c_3 - c_{Debye}$ is magnitude of the T^3 specific heat that is in excess of the Debye specific heat. Δn_0 and Δc_{ex} are the change in n_0 and c_{ex} between the light soaked and initial states. 80

A.1 Summary of film roughness results. Film thicknesses were measured by reflectometry. Roughnesses were determined from the analysis of AFM images. All of the membrane roughnesses were measured on the back surface of the membrane unless otherwise noted. 102

Acknowledgments

Any work of this scale cannot be completed without the assistance and support of others. I would like to thank my advisor, Frances Hellman, for providing me with the resources and guidance necessary to complete this project and her support throughout my academic career. My thanks also go to the members of my thesis committee, Steven Louie and Jeff Reimer, for taking time out of their busy schedules to offer advice and feedback in addition to reviewing this manuscript.

I am forever indebted to the past and present members of the Hellman lab that have helped me at every step in this project. I would like to especially thank Dave Cooke for being my friend and my partner in crime in the lab. Your help and support has been invaluable. Thanks go to Erik Helgren for his continued assistance and mentorship; Julie Karel for growing the *a*-Si films; Cathy Bordel for reviewing this manuscript; Micol Alemani, Li Zeng, Zoe Boekelheide, and Chloé Baldasseroni for many stimulating and useful conversations; and Barry Zink for teaching me the ropes of microfabrication and heat capacity along with many useful discussions on this project.

This work would not have been possible without the support of my collaborators. Thanks go to Xiao Liu and Tom Metcalf at the Naval Research Laboratory (NRL) for providing the internal friction measurements and many stimulating conversations; Joe Feldman, also at NRL, for many useful discussions and his continued interest in this project; Katherine Jenkins, Elke Arenholz, and David Kilcoyne at the Advanced Light Source for their assistance; David Cahill and the members of his lab for the room temperature sound velocity and thermal conductivity measurements; Joel Ager at Lawrence Berkeley Lab for use of his Raman scattering equipment and useful discussions; and Dick Crandall, Qi Wang, and Eugene Iwaniczko at the National Renewable Energy Lab (NREL) for their help in preparing the *a*-Si:H films and their hospitality during my visit.

The design and fabrication of the nanocalorimeter was made possible by the help and support of the Students and Staff of the Berkeley Microfabrication Facility. A special thank you goes to Jay Morford, Sia Parsa, Bob Hamilton and Katalin Voros for their dedication and support.

My success in academia was made possible by the commitment and support of the Faculty and Staff of the Ventura College Math and Science department; especially Colin Terry and David Doreo who kindled my interest in physics. My appreciation also goes to the Faculty and Staff of the U.C. San Diego Department of Physics who provided me with a rigorous physics education and created a vibrant atmosphere in the department, Andy Pommer for teaching me the fundamentals of working in a machine shop, Jeff Patterson for his support and friendship, and Fred Driscoll for teaching me everything that I needed to know about electronic circuits; it has been the gift that keeps on giving. Special thanks goes to the Faculty and Staff of the U.C. Berkeley Department of Physics for making us feel welcome after we arrived and who have provided invaluable support ever since including Irfan Siddiqi, John Clarke, Eleanor Crump, Don Orlando, and the staff of the electronics and machine shops.

There have been several people that have taken the time to act as mentors; either opening new doors for me or provided guidance to keep me on course. Dr. Terry deserves my thanks for introducing me to physics and taking the time to encouraging me to pursue

a degree in the field. Thank you Katalin Voros for giving me the opportunity to work with you in the Microlab and your continued encouragement. Congratulations on a job well done in creating the environment that makes the Microlab unique and good luck on your new endeavors. Thank you also goes to Joel Ager whose enthusiasm and support came at a much needed time in my graduate career.

Finally I would like to thank my family and friends for their love, patience, and encouragement through this process. Thank you to my parents for instilling a sense of wonder and inquisitiveness in me at a young age. And finally, I thank my wonderful wife Karen and our beautiful daughter Grey. Your love and support has kept me going through the highs and the lows. I can never thank you enough for what you have given me.

Thank you also goes to the funding agencies and the American people who choose to make the support of basic research a priority. The amorphous silicon measurements were supported under NSF Grant No. DMR-0907724 and the sample growth and development and fabrication of the nanocalorimeter was supported by the Director, Office of Science, Office of Basic Energy Sciences, Materials Sciences and Engineering Division, of the U.S. Department of Energy under Contract No. DE-AC02-05CH11231.

Daniel Queen

Department of Physics
University of California, Berkeley
373 Birge Hall
Berkeley, CA 94720
(510) 643-4113

611 Lexington Ave. Apt. D
El Cerrito, CA 94530
(510) 260-7657 cell
(510) 559-1833 home

Education

Ph.D **University of California, Berkeley**
Physics, May 2011.
Area of specialization: Thermodynamics of amorphous materials and MEMS fabrication.

M.S. **University of California, San Diego**
Physics, July 2004.

B.S. **University of California, San Diego**
Physics with departmental honors, July 2001.

Research Projects

Thermodynamic universality and the Staebler-Wronski Effect in a-Si and a-Si:H
Glassy materials have a heat capacity at low temperature in excess of the Debye heat capacity due to vibrational modes. The excess is due to tunneling of groups atoms between configurations that are close in energy. These states are not predicted to occur in tetrahedrally bonded materials, such as, a-Si and a-Si:H.

Major findings:
1) The tetrahedrally bonded network of pure amorphous silicon does not support the excess modes found in traditional glasses such as a-SiO_2.
2) Low energy excitations are present in a-Si but only in low density films suggesting that excitations occur in under-coordinated regions or voids.
3) Low energy excitations are present in dense a-Si:H films and H catalyzes the formation of low energy states by lowering the energy barrier for tunneling.

4) An increase tunneling states also results in an increase of harmonic excitations. This correlation is currently not described by the tunneling model.
5) Light soaking reversibly creates metastable low energy structural states in both a-Si and a-Si:H. This result suggests that the Staebler-Wronski Effect may have a structural origin.

Collaborators:
Richard Crandall, *National Renewable Energy Lab*
Qi Wang, *National Renewable Energy Lab*
Xiao Liu, *Naval Research Lab*
Joe Feldman, *Naval Research Lab*
Barry Zink, *University of Denver*
Joel Ager, *Lawrence Berkeley National Lab*
Catherine Jenkins, *Lawrence Berkeley National Lab*

Heat Capacity of Silicon nanowires

Crystalline silicon nanowires are known to have a thermal conductivity that is suppressed relative to bulk silicon. Boundary scattering of phonons has been suggested as the mechanism for this suppression but the role that quantum confinement of phonons plays in this system has not been investigated. We are measuring the heat capacity of a range of silicon nanowires diameters and lengths to see if there are any changes in the phonon density of states associated with quantum confinement.

Preliminary results:
The heat capacity of silicon nanowires appears to be close to the crystalline value in the temperature range of 2-300K. Further measurements below 2K will clarify this result.

Collaborators:
Tom Picraux, *Center for Integrated Nanotechnologies, Los Alamos National Lab*

Microfabricated, membrane-based measurement platforms

Nanocalorimeters

- Fabrication of our membrane-based calorimeters at the U.C. Berkeley Microlab.
- Design and fabrication of next generation calorimeters to measure 30nm thick films and small bulk samples (~200ng).
- Adapt calorimeters for use as an x-ray and electron transparent heater stage for use in synchrotrons and TEMs.

Soft X-ray photovoltaic platform

- Designed, fabricated, and performed measurements with an x-ray transparent photovoltaic platform to study the charge transport efficiency in polymer blends by simultaneously mapping composition and photocurrent as a function of X-ray energy.

Bolometers for International Thermonuclear Experimental Reactor (ITER)

- Collaboration with L. Giannone at the Max Plank Institute to extend the calorimeter design for use as a radiation hard bolometer in the ITER tokamak to characterize the VUV and soft x-ray output from the plasma.

Professional Experience

2006 – 2009 Junior Development Engineer at U.C. Berkeley Microlab. Part-time position. Responsibilities included developing new processing capabilities, qualifying new equipment for general use, writing and updating operating instructions for lab equipment, providing training and support for lab members, and processing for the MEMS and Nanotechnology Exchange.

2004 Assisted in designing a new 2000 sq. ft. lab space and coordinated and supervised moving the research labs of Dr. Frances Hellman and Dr. Robert Dynes from U.C. San Diego to U.C. Berkeley.

2003 – 2004 Department of Physics representative to the U.C. San Diego Graduate Student Council. Member of the Graduate Student Housing Committee.

2003 Boulder School for Condensed Matter Physics, "Frontiers of Magnetism." The program focused on advanced topics in magnetism and facilitated interactions between faculty and students.

2002 Graduate student representative to the U.C. San Diego Department of Physics external program review committee. Collected student comments, chaired meeting between review committee and students, and formulated graduate student response to the committee's report.

Awards and Honors

2010 Department of Physics, U.C. Berkeley. Lars Commins Award in Experimental Physics
2010 Department of Physics, U.C. Berkeley. Haas Scholars Mentorship Award
2005 Department of Physics, U.C. Berkeley. Segre Fellowship
2005 Department of Physics, U.C. Berkeley. Teaching Assistant Excellence Award
2002 Department of Physics, U.C. San Diego. Materials Physics Experimentalist Fellowship
2002 Department of Physics, U.C. San Diego. Teaching Assistant Excellence Award

Grants

"Thermodynamics of amorphous and nanocrystalline Si and Si:H thin films" Accepted by NSF (DMR-0907724) Total award: $375,000. This grant was based on my proposed thesis research and I co-authored the grant with Prof. Hellman.

User Facility Proposals

"Thermodynamic universality and local disorder in thin films of a-Si and a-Si:H." *Advanced Light Source, Lawrence Berkeley National Lab.*

"Specific heat measurements of VLS nanowires." *Center for Integrated Nanotechnologies, Los Alamos National Lab.*

Teaching Experience

Graduate Student Instructor U.C. Berkeley,

Physics 7B. Thermal Physics, Electricity, and Magnetism for science and engineering students. 2004.

Advanced Physics Lab. Senior Laboratory course with experiments in atomic, optical, condensed matter, and particle physics. 2005 – 2007.

Lab Instructor U.C. San Diego

Physics 1. Year long course in calculus based physics for life-sciences majors. Responsibilities included teaching, curriculum development, and training and supervising Teaching Assistants. 2001 – 2004.

Teaching Assistant U.C. San Diego

Physics 2CL. Laboratory course in Electricity and Magnetism for physical science and engineering students. 2002.

Physics Education Research Group U.C. San Diego

This group focused on the development of new curriculum for the undergraduate physics program. During my tenure, we designed and tested a program that emphasized an increase in hands on lab experience and interactive lecture discussions. 2001—2004.

Outreach

2006 – 2009 Microlab summer internship for high school students. U.C. Berkeley.

2006 Mentored Salvador Barriga. UCLeads program. U.C. Berkeley.

2010 – 2011 Mentoring Jason Ross. Haas Scholars program. U.C. Berkeley.

Publications

D.R. Queen, J. Karel, X. Liu, and F. Hellman, "Specific heat of e-beam evaporated amorphous silicon" In preparation.

D.R. Queen, Q. Wang, R.S. Crandall, and F. Hellman, "Specific heat of a-Si:H prepared by Hot-Wire CVD" In preparation.

D.R. Queen, J. Karel, Q. Wang, E. Iwanizcko, R.S. Crandall, and F. Hellman, "Photo-induced thermodynamic metastability in amorphous silicon" In preparation.

D.R. Queen and F. Hellman, "Two-Level Systems in amorphous silicon" In preparation.

C. Baldasseroni, D.R. Queen, David W. Cooke, K. Maize, A. Shakouri, and F. Hellman, "Heat transfer simulation and thermal measurements of microfabricated X-ray transparent heater stages," Submitted.

D.R. Queen, C.A. Jenkins, E. Arenholz, Q. Wang, R.S. Crandall, and F. Hellman, "XAS study of disorder in a-Si:H films prepared by Hot-wire CVD" In preparation.

M. Alemani, A. Huegel, E. Helgren, D.R. Queen, and F. Hellman, "Effect of magnetic Gd adatoms on the transport properties of ultrathin gold films" *Physical Review B* **82**, 195447, (2010).

D.R. Queen and F. Hellman, "Thin film nanocalorimeter for heat capacity measurements of 30 nm films" *Review of Scientific Instruments* **80**, 063901 (2009): selected for the June 15, 2009 issue of *Virtual Journal of Nanoscale Science & Technology*.

B. Watts, D.R. Queen, A.L.D. Kilcoyne, T. Tyliszczak, F. Hellman, H. Ade, "Soft X-ray Beam Induced Current Technique" 9th International Conference on X-ray Microscopy, 21-25 July 2008. *Journal of Physics: Conference Series,* **186**, 012023 (2009).

David W.Cooke, Z. Boelkelheide, D.R. Queen, and F. Hellman, "The role of the spin-density wave and disorder in the density of states of sputtered Cr films" *Journal of Applied Physics* **105**, 07C314 (2009).

E. Helgren, D. R. Queen, F. Hellman, L. Zeng, R. Islam, David J. Smith, "Concentration dependent microstructure and transport properties of the magnetic semiconductor Gd-Si" *Journal of Applied Physics*, **101**, 093712 (2007).

L. Giannone, D. Queen, F. Hellman, J. C. Fuchs, "Prototype of a radiation hard resistive bolometer for ITER" *Plasma Physics and Controlled Fusion*, **47**, 2123 (2005). (Giannone was the lead plasma scientist; I designed and fabricated the device)

D. Querlioz, E. Helgren, D.R. Queen, F. Hellman, R. Islam, David J. Smith, "Beneficial Effects of Annealing on Amorphous Nb-Si Thin Film Thermometer" *Applied Physics Letters*, **87**, 221901 (2005). (Querlioz was a visiting undergraduate who I co-supervised with Helgren)

B.L. Zink, V. Preisler, D.R. Queen, F. Hellman, "Magnetic moments and interactions near the metal-insulator transition in amorphous magnetic semiconductors." *Physical Review B*, **66**, 195208 (2002). (undergraduate honors thesis at UCSD)

F. Hellman, D.R. Queen, R.M. Potok, B.L. Zink. "Spin-glass freezing and RKKY interactions near the metal-insulator transition in amorphous Gd-Si alloys." *Physical Review Letters*, **84**, 5411 (2000). (undergraduate honors thesis at UCSD)

Presentations

Invited

"Thermodynamics of amorphous silicon for semiconductor and photovoltaic applications" Solid State Technology and Devices Seminar, Department of Electrical Engineering and Computer Science, University of California, Berkeley. November 2009.

"Thermodynamic Metastability in Amorphous Silicon"
Materials Science Division, Lawrence Berkeley National Lab. May 2011.

Contributed

"Excess low temperature heat capacity in a-Si:H thin films prepared by hot-wire CVD." APS March Meeting 2010.

"Specific heat of amorphous materials outside of the universal regime: a-Si, a-Si:H, and a-SiN." APS March Meeting 2009.

"Thin film nanocalorimeter for measuring the heat capacity of 30 nm films from 300 mK to 500K." APS March Meeting 2007.

"Enhanced Electron Density of States in thin films of Cr." APS March Meeting 2006.

"The Role that Varying Nanocrystallinity Plays in the Thermodynamics of CoO Films." APS March Meeting 2005.

Chapter 1

Introduction

Amorphous silicon *a*-Si is a glass consisting of a single element. While chemically simple, the complexity of its behavior has kept it a topic of interest for the last 50 years. In the liquid state silicon is a metal and is thought to have a first order liquid-liquid phase transition just prior to crystallization where the melt changes from a fragile [1], high density hexavalent liquid to a strong, low density tetragonal liquid [16]. This process is related to the density maximum seen in water at its freezing point and is found in other tetrahedral liquids [17].The strong nature of liquid silicon has an important consequence, it cannot be quenched rapidly enough from the melt to avoid crystal nucleation and form a glass. However, it is possible to prepare silicon in the amorphous state by avoiding the liquid to solid phase transition all together through vapor deposition. Here atoms are taken directly from the vapor phase and condensed into the solid phase. The crystalline phase is avoided when the substrate temperature is kept below 600°C and the silicon atoms from the gas are rapidly quenched to the solid phase. Amorphous silicon can be prepared either as pure *a*-Si or as an alloy, typically with hydrogen *a*-Si:H were the hydrogen is used to passivate dangling bonds. Much of the research on amorphous silicon has focused on optimizing the deposition process of the hydrogenated alloy because of its technological importance as a low cost method of depositing a semiconductor on transparent substrates for use in photovoltaic devices, flat panel displays, and flexible substrate electronics.

From an experimental standpoint, the availability of amorphous silicon solely in thin film form can be problematic. While electrical and optical probes are well suited to thin film measurements, thermodynamic measurements are not. The primary limitations are the difficulty in thermally isolating the microscopic thin film from the macroscopic measurement apparatus and the large background addenda of the substrate, heaters, and thermometers. A survey of the experimental and theoretical results that are relevant to this work will be presented in Chapter 2. In Chapter 4 we will discuss the design and fabrication of a micromachined, thin film nanocalorimeter that is designed specifically to address the problem of measuring the heat capacity of a thin film. The remaining chapters will describe our findings but first we motivate this work with a brief introduction to two outstanding

[1] The concept of strong and fragile glass formers describes the kinetics on approaching the glass transition from the liquid state; Angell demonstrated a fundamental link between these kinetic properties and the thermodynamic properties of the system, connected through the energy landscape of the structure [15].

questions regarding amorphous silicon: do the two-level systems that are found in all other glasses occur in amorphous silicon and what is the mechanism that causes the light-induced degradation of amorphous silicon known as the Staebler-Wronski Effect?

The low temperature thermodynamic properties of amorphous materials are known to differ markedly from their crystalline counterparts [1, 18]. The heat capacity is orders of magnitude larger than that predicted for acoustic waves by the Debye model and the thermal conductivity is orders of magnitude lower than the corresponding crystalline values. This striking difference between the amorphous and crystalline states is attributed to the random atomic configurations that are frozen in at the glass transition and can be described by the phenomenological two-level systems, or tunneling, model. It is assumed that groups of atoms sit in a local energy minimum that is separated from a neighboring minimum by a large energy barrier (up to several eV) but that a finite probability to tunnel through the barrier exists. This leads to a splitting of the ground state energy on the order of 0.1 meV that is responsible for the low temperature properties. In contrast to the glass transition where the fragility is material dependent, the low temperature properties are relatively insensitive to the preparation conditions or the chemical components of the glass [2, 19]. The one exception to this is thin films of tetrahedrally coordinated materials: *a*-C, *a*-Si, *a*-Ge and some of their alloys [20, 10, 14, 19]. Perhaps the most interesting of these is *a*-Si:H where the excess low energy states can be created and destroyed by light-soaking and annealing [21].

The properties of *a*-Si:H under illumination are well documented in the literature due to its technological importance as a photovoltaic material. In particular, a great deal of effort has gone into minimizing the density of dangling bond defects that result from the deposition process as they act as recombination centers for photo-excited electron-hole pairs. Materials with a low dangling bond density have two common properties: the amorphous matrix has less electronic and structural disorder and the material is hydrogenated to passivate the dangling bonds. One source of dangling bonds that is not fully understood is the Staebler-Wronski Effect (SWE) where the density of dangling bonds increases with exposure to light. These light-induced defects can be removed upon annealing at $T \approx 150^{\circ}$C. The process is entirely reversible and is thought to result from weak Si-Si bonds breaking upon absorbing a photon and possibly the movement of hydrogen into the broken bond to stabilize it.

Unique among *a*-Si:H preparation methods is the hot-wire chemical vapor deposition (HWCVD) technique which has been shown to produce films with fewer dangling bond defects, a more locally ordered structure, and that are less susceptible to the Staebler-Wronski Effect [22, 23, 24, 25]. Also, the density of two-level systems in these films is thought to be orders of magnitude lower than in any other amorphous material and that their density is tunable with growth conditions [20, 14, 19]. More recent measurements have shown that the room temperature thermal conductivity is larger than any other amorphous material [26, 13]. Thus, HWCVD *a*-Si:H may provide insight into the source of the universal properties that are found in all other glasses and have yet to be completely explained.

The goal of this work then is two-fold: investigate the origin of two-level systems in amorphous silicon and determine if the Staebler-Wronski Effect is related to the two-level systems. In answer to the first question, we have found that the TLS are present in

a-Si and *a*-Si:H and that the presence of hydrogen lowers the barrier for their formation. The answer to the second question is an emphatic yes. We find that the Staebler-Wronski Effect is intimately related to the presence of TLS in *a*-Si:H and we suggest that large scale structural rearrangements occur upon light-soaking and that these are the driving force for the SWE. Thus the resulting dangling bonds that affect the electronic properties are a result of these structural changes. This work represents the first systematic study of the low temperature specific heat of amorphous silicon and has only recently been possible with the design and fabrication of the thin-film nanocalorimeter.

Chapter 2

Previous Work

2.1 Low-temperature properties of glasses

The periodic array of atoms that defines a crystal is absent in a glass but on average the neighborhood of any given atom differs little from that of an atom in a crystalline environment [27, 28]. The Debye model assumes that the material can be treated as an elastic continuum with an average sound velocity and appears isotropic to long wavelength phonons and the heat capacity at low temperatures is

$$C_{Debye}(T) = \frac{12\pi^4}{5} N k_B \left(\frac{T}{\theta_D}\right)^3 \tag{2.1}$$

where,

$$\theta_D = \frac{\hbar v}{k_B}\left(\frac{6\pi^2 N}{V}\right)^{1/3} \tag{2.2}$$

is the Debye temperature, v is the sound velocity, and N/V is the number density of atoms [11]. At high temperatures C approaches the Dulong-Petit limit $C = 3Nk_B$ for fully populated oscillators. For a non-crystalline, dielectric material then it might seem reasonable to assume that the low temperature specific heat should have the T^3 temperature dependence that is characteristic of phonons in an isotropic material. However, in 1971 Zeller and Pohl published their survey of the low temperature specific heat and thermal conductivity for a variety of glasses which all showed behavior that was strikingly different from their crystalline counterparts. Figure 2.1 reproduces their results for crystalline α-quartz and the glass vitreous silica plotted as C/T^3 versus T on a log-log scale to emphasize the deviation from the Debye heat capacity.

The specific heat of α-quartz follows the prediction of the Debye model at low temperatures but with a peak at 20K. This feature is due to non-propagating modes with zero group velocity that occur at the Brillouin zone boundaries where the phonon dispersion curve is flat. The Debye model makes the assumption that the dispersion relation is linear which is suitable at very low energies (temperature). For higher temperatures one must use the Born-von Kármán model which considers the full phonon dispersion curve [29]. In the amorphous material, the low temperature specific heat is considerably larger than the Debye

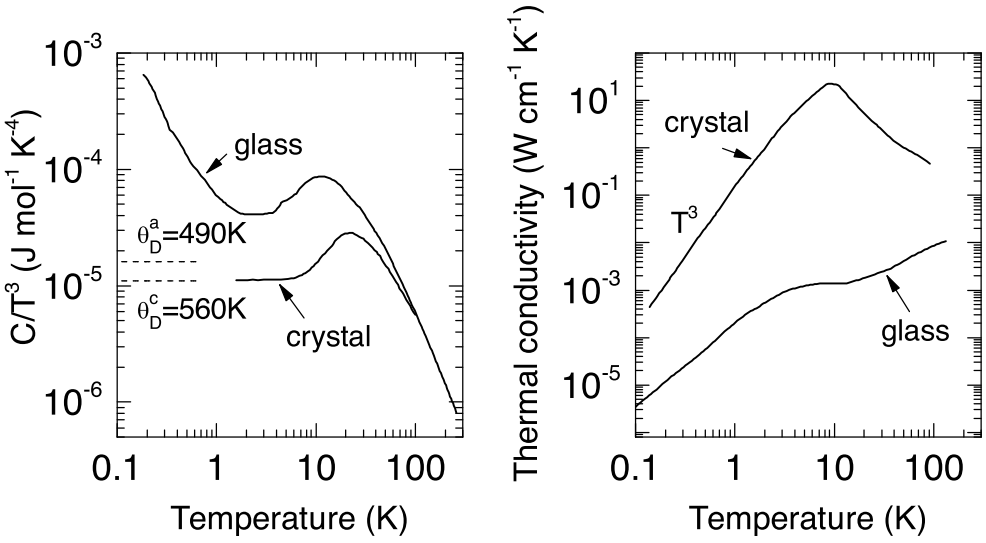

Figure 2.1: Specific heat and thermal conductivity of α-quartz and vitreous silica (a-SiO_2) from Ref. [1]. The Debye specific heats (- - -) are calculated from the sound velocity.

prediction. Three features are prominent: a peak around 10K, a large excess below 1K, and the specific heat is in excess of the Debye specific heat at intermediate temperatures. The 10K peak, often called the Boson peak, is thought to be due to non-propagating modes as in the crystalline case but the origin must be different as the concept of a Brillouin zone is meaningless in a material without translational invariance [30]. The excess specific heat below 1K has a temperature dependence of T^n where $n \approx 1 - 1.5$ and comes from a very low energy excitation (≤ 0.1 meV) [31]. The excess T^3 heat capacity between $1 - 10$K is thought to come from a harmonic excitation of a Boson-like mode that does not carry heat.

In a crystalline material the thermal conductivity k can be divided into three regions: high temperatures where the phonon mean free path ℓ is dominated by Umklapp scattering, a peak where ℓ is on the order of the impurity concentration or the sample dimension, and a low temperature region where the phonon population decreases as T^3. In an amorphous material k decreases with temperature but then reaches a plateau between $1 - 10$K after which the thermal conductivity decreases as T^δ where $\delta \approx 1.6 - 1.8$. The drop in k is as expected for phonon scattering from the disordered matrix where ℓ is on the order of an interatomic spacing. The plateau region can be modeled as a Rayleigh scattering of phonons [1] from the disorder but this scattering mechanism cannot reproduce the $T < 1$K behavior [18].

2.2 Two-level systems model

The phenomenological two-level systems (TLS) model, also referred to as the tunneling model, was developed to describe the $T < 1$K properties. This model is based on similar experimental results from the doped alkali-halide crystals where a set of TLS re-

sults from doping of the crystal. Classic examples are the Li^+ ion in KCl which has eight degenerate positions on the K^+ site or the eight rotationally degenerate configurations of CN^- along the diagonal of the Cl^- site. The energy barrier separating the states is on the order of several electron volts but the finite probability to tunnel through the barrier leads to an energy splitting of the ground state on the order of 0.1meV [32, 33]. This energy splitting then leads to a contribution to the heat capacity and suppression of the thermal conductivity both below 1K.

It was with the alkali-halides in mind that, independently, Phillips [3] and Anderson, Halperin, and Varma [4] proposed the TLS model. This model assumes that there exists a set of TLS in an amorphous material that are distributed uniformly in energy and space. A physical model for the TLS is that at the glass transition groups of atoms are frozen into configurations that have a local energy minimum that differ only slightly in energy by an amount Δ from another configuration [34, 18, 35]. The energy barrier that needs to be overcome for structural rearrangement is on the order of $0.1 - 0.5$eV, but there is a finite probability to tunnel through the energy barrier and this leads to a tunnel splitting of the ground state Δ_0 such that the ground state energy splitting is

$$E = \sqrt{\Delta^2 + \Delta_0^2}. \tag{2.3}$$

For an individual TLS, the heat capacity is just that of a spin-$\frac{1}{2}$ system and has the Schottky form,

$$C_{\text{Sch}} = k_B \left(\frac{E}{2k_BT}\right)^2 \text{sech}^2\left(\frac{E}{2k_BT}\right). \tag{2.4}$$

By assuming that the states are uniformly distributed we can write the density of states for TLS as $n(E) = n_0$ and calculate the total heat capacity,

$$C = \int_0^\infty n_0 k_B \left(\frac{E}{2k_BT}\right)^2 \text{sech}^2\left(\frac{E}{2k_BT}\right) dE, \tag{2.5}$$

$$= \frac{\pi^2}{6} k_B^2 n_0 T, \tag{2.6}$$

thus the excess capacity has a linear temperature dependence and is proportional to the TLS density of states $n(0)$. If instead all of the TLS had the same energy splitting $n(E) = n_0\delta(E)$ then the resulting heat capacity would have the usual Schottky anomaly as in Eq. 2.4 with a maximum near $T_m = \frac{E}{2k_B}$ [29].

From the kinetic theory of gases we find that the thermal conductivity $k = \frac{1}{3}Cv\ell$ where C is the heat capacity per unit volume, v is the sound velocity, and ℓ is the mean free path of a heat carrying particle. It has been shown that phonons are the heat carriers in a glass [36] and in order to obtain the T^2 thermal conductivity, the phonon mean free path must decrease as T^{-1} below 1K. The TLS model provides a mechanism for this to occur whereby phonons are resonantly scattered by the fraction of TLS with energy splitting on the order of k_BT. A phonon is absorbed by a TLS in the ground state and then decoherently emitted at the same energy.

In addition to scattering phonons, the TLS also scatter low frequency acoustic waves. Acoustic waves may be excited either using a vibrating reed geometry, a torsional

oscillator, or a surface transducer [37]. In the TLS model, the scattering of acoustic waves is temperature independent below 1K due to the broad distribution of energy splittings of TLS. By applying an intense acoustic field it is possible to saturation absorption from TLS. Internal friction Q^{-1} which, measures the damping of a resonant oscillator due to absorption from TLS, is one of the few techniques suited form measuring the TLS density in thin films [38, 14].

2.3 Literature summary of TLS in amorphous silicon

There have been several attempts to look for TLS in *a*-Si and *a*-Ge. Löhneysen *et al.* measured the specific heat below 3K of *e*-beam evaporated, thick films of *a*-Si grown at $T_S = 200°$C and *a*-Ge grown at room temperature (RT) [39, 40, 41]. The *a*-Ge sample was found to have an excess heat capacity with a shallow maximum at 0.4K which disappeared upon annealing at 350°C along with a T^3 term that was in excess of the Debye specific heat. The *a*-Si film similarly had an excess heat capacity below 1K but with a contribution linear in T above 1K and a T^3 term in excess of the Debye heat capacity. Löhneysen *et al.* argued that the excess could not be due to TLS because the low temperature annealing does not affect the TLS density in other glasses, but instead that this excess below 1K is due to exchange coupled clusters of dangling bonds. Heat capacity measurements in magnetic fields showed that a Schottky anomaly appeared and that a 6T field was sufficient to suppress the excess heat capacity of both *a*-Ge and *a*-Si. Thus the authors concluded that a Zeeman splitting of the dangling bonds were the source of the field dependent excess heat capacity [42, 43]. Further studies were performed on neutron irradiated crystalline silicon to create divacancies. The result was an increase in the heat capacity below 1K that increased with increasing neutron dose. Above 1×10^{21} n^0 cm^{-2} the sample contained 6% amorphous regions. The heat capacity of the irradiated films was less than that of the evaporated film even though the elecron spin resonance (ESR) spin densities were comparable $\sim 10^{18}$ cm^{-3}. The mass density of the irradiated films were close to the crystalline value. The authors concluded that fewer than 10% of the total spins were exchange coupled and were responsible for the excess heat capacity.

There are two examples of the specific heat of *a*-Si:H available in the literature. The first, by Schink and Löhneysen, is a measurement of a glow-discharged film deposited at room temperature with ~ 35 at.% H [40] and a mass density of 1.5 g/cm^3. The authors found the low temperature heat capacity to be an order of magnitude higher than in crystalline Si. They report that the heat capacity dropped by a factor of two upon annealing at 210°C. ESR measurement showed that the spin density decreased from 4×10^{18} cm^{-3} to 2×10^{17} cm^{-3} after annealing. The heat capacity of the *a*-Si:H film is comparable to the evaporated *a*-Si below 0.4K including the Schottky-like anomaly. For $T > 0.4$K, the heat capacity of the unannealed *a*-Si:H film remains in excess of C_{Debye} while the *a*-Si film approaches the crystalline silicon value. The authors concluded the decrease in dangling bonds and heat capacity after annealing indicated that dangling bonds were responsible for at least part of the excess. It is not reported whether or not the Schottky anomaly disappeared. The second *a*-Si:H film was obtained by removing material from a support inside a Plasma Enhanced CVD depostion system [44]. This film 40mg sample had nominally 17 at.% H,

there was a large fraction of polysilane groups (SiH_x) indicative of low temperature growth and poor electronic quality. The ESR spin density was found to be 4.4×10^{-16} cm^{-3} and the mass density was 2.00 g/cm^3. Heat capacity measurements were reported for this film from $0.1 - 5$K. The heat capacity is of the same magnitude as the sample in [40] but without the Schottky anomaly. Graebner *et al.* interpreted their results to be due to atomic TLS as the resulting excess heat capacity was too large to be accounted for by dangling bonds. An annealing study was performed on this material and it was found that annealing above the growth temperature resulted in an increase in the heat capacity below 5K that was due to H_2 formation. The time dependence of the excess heat capacity was consistent with ortho- to para- transition in molecular hydrogen [45].

Above 2K, Mertig *et al.* measured the heat capacity of a 35μm film grown at $T_S = 300$°C from $2 - 50$K and Zink *et al.* measured the heat capacity from $4 - 300$K of a 4000Å film grown at 45°C [46, 9]. Neither film showed a contribution from TLS but both had T^3 term in excess of the Debye specific heat calculated from the sound velocity. Both films showed a decrease in the temperature of the Boson peak that is consistent with other amorphous materials [30]. The film in Ref [9] had a mass density $\rho = 2.09$g cm^{-3} with no visible voids or microstructure in TEM.

Much like heat capacity, there are very few thermal conductivity results in the literature to indicate whether TLS are present in *a*-Si. The thermal conductivity of *a*-Ge has a plateau at above 1K and decreases as expected for TLS [47, 48, 49]. Graebner *et al.* showed that the TLS contribution scaled inversely with the film density and thus the TLS were associated with low density regions in the film. The scattering from these low density regions could be modeled as cylindrical voids with their axis along the growth direction.

While the available heat capacity and thermal conductivity data for amorphous silicon is limited, there have been several measurements of the low temperature internal friction Q^{-1} [19, 20, 10, 21, 14, 50, 51]. Measurements of Q^{-1} probe the relaxation process of those TLS that can be excited by phonon absorption. Recent results have shown that TLS are present in both evaporated *a*-Si and *a*-Si:H prepared by either sputtering or CVD deposition. All tetrahedrally bonded materials are found to have a lower density of TLS as compared to bulk quenched glasses. The density of TLS as measured by Q^{-1} is sensitive to the details of the growth process. The TLS density is lowest in those materials prepared in a way that gives the best electrical properties: low dangling bond density and small Urbach edge. The Urbach edge is determined from optical absorption from band tails states and is a measure of the disorder [28]. Further, these device quality films are known to have a more ordered amorphous network as measured by the width of the Si-Si transverse optic (TO) phonon peak in Raman scattering or the first sharp diffraction peak in x-ray [52]. Measurements of Q^{-1} of evaporated *a*-Si in magnetic fields up to 6T showed only a weak magnetic field dependence and the authors concluded that TLS in *a*-Si are atomic in origin and not due to dangling bonds [53]. Molecular hydrogen has been observed in Q^{-1} measurements as a peak at $T = 13.8$K, the hydrogen triple point.

2.4 Staebler-Wronski Effect

In 1977, Staebler and Wronski reported that the photo and dark conductivities of a-Si:H decreased after prolonged exposure to light and that the original conductivity could be recovered by annealing above 150°C [54]. It was later shown that the density of dangling bond defects n_{db} increases from 10^{16} cm^{-3} before light exposure to 10^{17} cm^{-3} afterward. The dangling bond defects are neutrally charged and create states in the center of the forbidden gap that act as recombination centers for electron-hole pairs. This phenomena has come to be known as the Staebler-Wronski Effect (SWE) and it limits the efficiency of of a-Si:H photovoltaics to 10% efficiency. However, a-Si:H remains an attractive system because it supports both n-type and p-type doping and can be prepared at low cost in thin-film form.

The SWE is thought to be due to the breaking of weak Si–Si bonds upon the absorption of a photon and the stabilization of the broken bond by diffusion of hydrogen on to the site forming a Si–H bond and a dangling bond [52, 55]. Annealing studies have shown that the relaxation of the dangling bond defects obeys a stretched exponential relaxation indicating that there is a distribution of energies for the weak bonds [56]. It has recently been shown the SWE is reduced in a-Si:H films prepared by the hot-wire CVD (HWCVD) process [24]. These films have low dangling bond defect densities and are more structurally ordered as measured by the Si TO-TO like peak half-width in Raman scattering, the first sharp x-ray diffraction peak, and the Urbach-Edge parameter which measures the number of band tail states[57].

Metastable states in a-Si:H can be introduced not only by light-soaking but through charge injection [58] and extraction [59] along with quenching from elevated temperatures [56]. The light-induced metastability is typically discussed in terms of the dangling bond defects that degrade the electrical transport properties. However, there is evidence that large scale structural rearrangements are occurring as well [60]. In particular, the density of two-level systems (TLS) that are responsible for the low temperature properties of glasses have been found to increase upon light soaking in a-Si:H [61]. The TLS are thought to be due to single atoms or groups of atoms that have structural configurations that are close in energy and, at low temperature, tunnel through the energy barrier separating these configurations [4, 3]. These states have been shown to have an atomic not electronic origin in amorphous silicon [53].

Chapter 3

Survey of experimental methods

This chapter discusses the various experimental techniques employed in this work. Thin-film calorimetry will be discussed generally here but a detailed discussion of the nanocalorimeter will be delayed until Chapter 4.

3.1 Thin film growth techniques

3.1.1 Electron beam evaporation

Thin films of pure *a*-Si were prepared by electron beam evaporation in UHV deposition chamber on nanocalorimeters along with MgO, high resistivity silicon, and *a*-SiO_2 and *a*-Si-N coated silicon substrates. The chamber base pressure was $\leq 5 \times 10^{-8}$Torr for all samples and the growth rate was $0.5 - 1$Å/s. The temperature of the sample holder T_S was varied between $45° - 400°$C $\pm 15°$C during growth.

3.1.2 Hot-wire chemical vapor deposition

Samples of *a*-Si:H were prepared by hot-wire chemical vapor deposition (HWCVD) at the National Renewable Energy Laboratory (NREL) in Golden, CO. The hot-wire process uses a tungsten filament heated to 2000°C to decompose the silane gas to create Si and H radicals that react at the growth surface to form an *a*-Si:H film. The base pressure of the deposition chamber was $\leq 5 \times 10^{-7}$Torr and the process pressure was 10mTorr with a gas flow rate of 20sccm. In this system, the best quality films with a minimum in the dangling bond defect density are grown at $T_S \approx 350°$C resulting in 4 at.% H [62] while the films with the lowest internal friction correspond to the low hydrogen content films grown at the highest growth temperatures. As with other deposition methods, the H content c_H decreases with increasing growth temperature as H is driven out of the amorphous network [52]. The dangling bond defect density also decreases with increasing growth temperature but then goes through a minimum as the rate of H evolution exceeds the retention rate neccessary to passivate dangling bonds [52]. In films prepared by Plasma-Enhanced CVD and glow-discharge this minimum occurs a ~ 10 at.% H whereas in the HWCVD films this minimum occurs at ~ 4 at.% H [63]. The minimum in the defect density corresponds with a minimum in the Urbach edge which is a measure of the electronic joint density of states (JDOS)

and thus a measure of the electronic disorder. The films studied here were grown with $T_S = 300 - 500°$C.

3.2 Materials Characterization

3.2.1 Raman Scattering

Raman scattering measurements were performed with the 514.5 nm line of an Ar-ion laser at 100mW. Argon gas was flowed across the sample surface to suppress the rotational lines from ambient diatomic gases which dominate the spectra below 100 cm^{-1}. Raman spectra were recorded with a cooled R928 photomultiplier tube attached to a Jobin-Yvon U-1000 double grating monochromator. Diffraction gratings with 1800 grooves/mm were used and the entrance and exit slits were set at 500μm with the two intermediate slits set to 100μm resulting in a spectral dispersion of 4.5cm^{-1}. The relative intensity of the Rayleigh scattered light is 10^{-14} at 20cm^{-1} but is still visible in the spectra due to the high intensity of the laser. Figure 3.1 shows the measured Raman spectra for crystalline and amorphous silicon. The Rayleigh scattered light from the crystalline silicon was fit to a Lorentzian and subsequently subtracted from the amorphous spectra. The Raman active mode of crystalline silicon is visible at 521cm^{-1}. An observable peak in the amorphous spectra at 521cm^{-1} indicates the presence of a crystalline phase in the amorphous film [64]. In an amorphous material, k is no longer a good quantum number so the selection rules are relaxed and all phonon modes can couple to the incident light [65]. The resulting spectrum reflects the weighted phonon density of states that is considerably weaker than but comparable to a broadened crystalline phonon density of states [65].

3.2.2 Ion-beam Analysis

Rutherford Backscattering (RBS) and Hydrogen forward scattering (HFS) spectra were measured using the Pelletron tandem accelerator at the Lawrence Berkeley National Lab Ion Beam Facility. Spectra were acquired with incident energies from $3.0 - 3.1$ MeV where the energy was increased to probe the oxygen resonance through the depth of the film. The RBS data were acquired in the Cornell geometry at an incident beam angle of 55°. The HFS scattering spectra were collected in the IBM geometry with an incident angle of 75°. Charging of the mylar film in the detector prevented determination of an absolute value of the H content but the relative values are consistent with the growth calibration. RBS and HFS spectra were modeled with the SIMNRA software package.

3.2.3 Sound velocity and thermal conductivity

Sound velocity and room temperature thermal conductivity measurements were performed by David Cahill at the University of Illinois, Urbana-Champaign. Sound velocity was measured by picosecond acoustics [7]. The picosecond acoustic method is a pump-probe technique where the probe beam monitors the reflectivity change in an aluminum capping layer due to heating from the pump beam and the subsequent echo after the sound wave reflects from the film-substrate interface. This technique requires an acoustic impedance

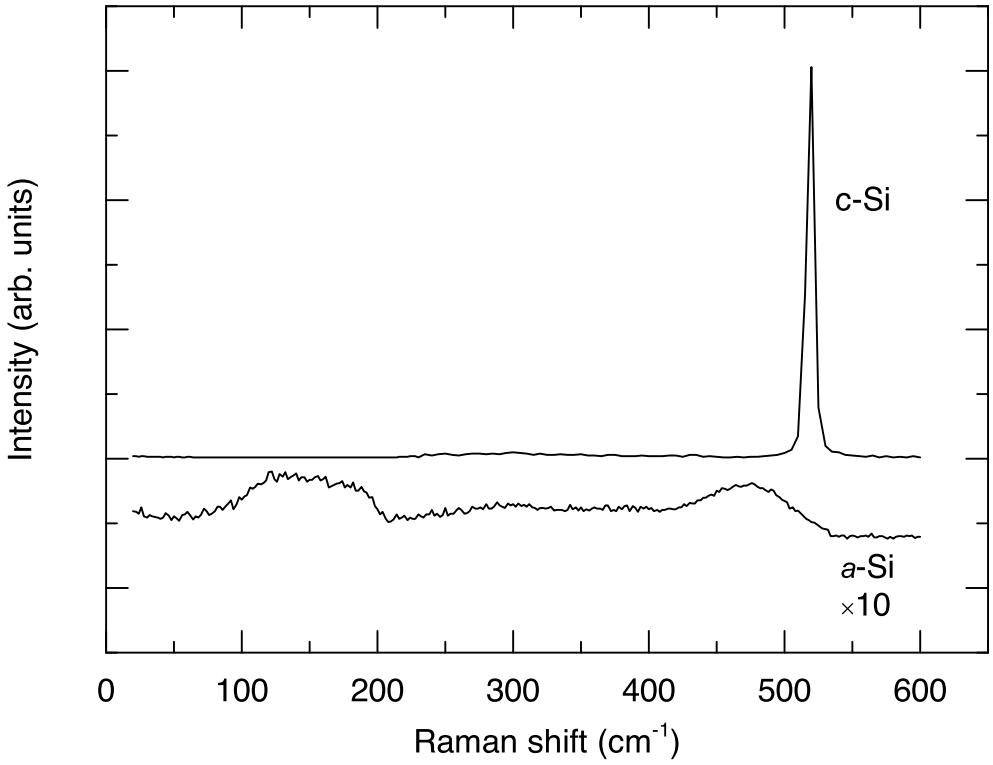

Figure 3.1: Raman scattering for crystalline and amorphous silicon. The peak at 521cm^{-1} is the first order Raman mode in crystalline silicon. The Raman spectrum of a-Si is proportional to the phonon DOS. The upturn in the spectrum below 75cm^{-1} is due to Rayleigh scattered light from the laser.

mismatch between the sample and substrate. The longitudinal sound velocity $v_l = 2l/\Delta t$ where Δt is the time delay between the pump beam and the echo, and l is the thickness of the sample. The time-domain thermal reflectance (TDTR) technique was used to measure the room temperature thermal conductivity [66, 67]. The TDTR method is also a pump-probe technique where the thermal diffusion length depends on the probe beam frequency and the thermal diffusivity of the film $D_f = k_f/C_f$ where k_f and C_f are the thermal conductivity and heat capacity of the film. The thermal conductivity in determined by comparing the cooling curve after the pump pulse to a theoretical model of the film and interfacial thermal conductances.

3.2.4 Internal Friction

Internal friction Q^{-1} measurements were performed between $0.3 - 300$K by Xiao Liu and Tom Metcalf at the Naval Research Laboratory in Washington, D.C. Q^{-1} measures the relaxation process of acoustic waves interacting with TLS [19]. From the TLS model

$Q^{-1} = \frac{\overline{P}\gamma}{\rho v_t^2}$ where $\overline{P}$ is the subset of TLS with level splittings that couple to the acoustic waves, γ is the coupling energy between the TLS and acoustic waves, ρ is the density and v_t is the transverse sound velocity. We are interested in Q^{-1} to compare the density of TLS from heat capacity to the internal friction. Measurements were made using high purity, single crystal silicon double paddle oscillators (DPO) operating in the antisymmetric mode by exciting the DPO at 5500Hz [38, 14]. Thin films of *e*-beam *a*-Si were deposited at U.C. Berkeley on the neck of the DPO. Film thicknesses were ≈ 3000Åand the thicknesses were checked with a KLA-Tencor Alphastep IQ profilometer. By measuring Q^{-1} of the DPO before and after deposition of the film, it was possible to determine the shear modulus $G = \rho v_t^2$ of the film. By measuring G and ρ we were able to calculate v_t. After the initial measurement, films were light-soaked under a PV Measurements Inc. small area solar simulator with care taken to keep the film from heating above 50°C to avoid relaxation of light induced defects. Q^{-1} was also measured on films after annealing. Heating and cooling rates were ~ 5K/min.

3.2.5 Electron spin resonance

The density of dangling bond defects can be determined by measuring the signal strength of the resonant transition between the Zeeman split energy levels of the paramagnetic dangling bond defect [52]. The electron spin resonance (ESR) technique is sensitive to dangling bond densities on the order of 10^{11}cm^{-1}. Dangling bond defect densities for the *e*-beam evaporated *a*-Si were determined by ESR measurements performed by David Bobela at the National Renewable Energy Lab. The ESR signal was found to be isotropic and have a Lande g-factor $g = 2.0055$ as is typical of dangling bonds in *a*-Si.

3.3 Calorimetry

3.3.1 Sample preparation

Thin films of *a*-Si were deposited on the nanocalorimeter through a micromachined evaporation mask. The shadow mask is designed to sit in the etch pit on the backside of the calorimeter so that films are only deposited in the central sample area of the membrane.

A special sample plate was manufactured for the growth of the hot-wire CVD films so that the membrane sample surface was exposed to the reactive gas while protecting the heaters and thermometers on the top surface. The delicate membrane of the calorimeter will break if placed in contact with any surface so a depression was cut into the plate to prevent contact. A pressure differential across the membrane could potentially cause the membrane to break so a small ventilation channel was cut from the back of the sample plate into the depression. The ventilation channel was sufficiently narrow and long to prevent radicals from depositing *a*-Si:H on the front surface of the device. While Si and H radicals were not present near the front surface, the Pt heaters and thermometers were exposed to silane gas and for $T_S > 370$°C, Pt-Si formed on the top of the Pt layer [68]. The density of the Pt-Si layer was consistent with the formation of Pt_2Si. The thickness of the Pt-Si silicide layer was determined by scratching off some of the silicide from the Pt layer and measuring the underlying Pt thickness. The heat capacity of Pt_2Si could not

be found in the literature so the addenda were corrected with the Debye and free-electron heat capacities from calculations of the elastic constants and electronic structure [69]. We estimate that the uncertainty in the Pt-Si parameters introduces a negligible error in the heat capacity since the correction to the low temperature heat capacity is dominated by the electronic heat capacity of Pt which can be corrected by knowing the thicknesses of the Pt layer on both the addenda and the sample device. The free-electron heat capacity for a metal is $C_{el} = \gamma_{el} T$ [11]. For bulk Pt, $\gamma_{el} = 6.8$mJ mol^{-1} K^{-1} and we estimate that $\gamma_{el} = 0.64$mJ mol^{-1} K^{-1} for Pt_2Si. The Pt_2Si heat capacity is $\leq 4\%$ at all temperatures and is $\leq 2\%$ below 7K.

3.3.2 Patterning samples on the calorimeter

The shadow mask was not used for the CVD films as the growth process is not directional for this process as it is for evaporation. Here the CVD film was allowed to deposit on the entire back surface of the membrane to ensure a uniform film in the sample area. Subsequently, an *a*-AlO_X was sputtered on the central sample area through a shadow mask and then a Cu film was evaporated through the deposition mask. The Cu layer acted as an etch mask when the device was placed in a reactive ion etcher to remove the *a*-Si:H from the membrane border. The *a*-Si:H layer was etched at 50W in SF_6 gas in 15 second intervals until the film was visually removed. The removal of the film was confirmed by reflectometry. Less than 5% of the total *a*-Si-N membrane thickness was etched during the process so that the change in the total addenda heat capacity was less than 1%.

3.3.3 Measurement Apparatus

Heat capacity measurements were made in a one-shot ^{4}He cryostat from $2 - 300$K [70]. The taper sealed cryostat was continuously pumped with a Turbo molecular pump to a base pressure $\leq 1 \times 10^{-7}$Torr as measured at the turbo pump. At low temperatures, the pressure in the cryostat was likely lower due to cryo-pumping to the vacuum can by the liquid He bath. The nanocalorimeter was thermally anchored to a copper sample block and electrical connections were made to device by gold wire bonding. The temperature of the cryostat was controlled with a Lakeshore 340 to better than 0.5mK at 2K.

3.3.4 Light-soaking

The heat capacity samples were light soaked under a PV Measurements Inc. small area AM1.5G solar simulator for 7 days to fully saturate the samples. The samples were light soaked through the top surface of the transparent membrane. The transmission through the calorimeter was measured at 633nm with a HeNe laser. The 500Å *a*-Si-N membrane was found to be 60% transmissive and the 500Å Pt film used for the heaters and leads was 50% transmissive. The heaters and thermomters cover $\sim 20\%$ of the sample area on the membrane and partially shadowed the device during light soaking. We believe that this is partially compensated by the reflection from the Cu conduction layer under the silicon film. The resistance of the sample heater was monitored during the light soaking the temperature remained below 30°C.

3.3.5 Annealing

Heat capacity samples were annealed to relax the amorphous network, remove light induced dangling bonds, and quench thermally induced dangling bonds. All of the heat capacity sample annealing was preformed using the Pt sample heater on the membrane in the high vacuum cryostat. Because of the low thermal mass of the membrane, the samples could be annealed to hundreds of degrees centigrade with only a few milliwatts of power. The low mass also results in a fast thermal response time. Heating and cooling rates of $\approx 10^4$K/s were possible by turning on the heater with a current step as well as $5-10$K/min rates with current ramp. Quenching from 300°C to 6K was possible by turning off the heater with a step function. The 2mW thermal load from the sample heater only raised the temperature of the cryostat from 4.2K to 6K. The sputtered $200-300$Å a-AlO_x buffer layer was sufficient to prevent diffusion of the Cu into the a-Si. Without the buffer layer, even modestly low temperature thermal treatments would result in rapid diffusion of the Cu into the a-Si and a-Si:H films.

Chapter 4

Thin-film nanocalorimetry

A silicon nitride membrane-based nanocalorimeter is described for measuring the heat capacity of 30 nm films from 300mK to 800K and in high magnetic fields with absolute accuracy $\sim 2\%$. The addenda heat capacity of the nanocalorimeter is less than 2×10^{-7} J/K at room temperature and 2×10^{-10} J/K at 2.3K. This is more than 10 times smaller than any existing calorimeter suitable for measuring thin films over this wide temperature range. The heat capacities of thin Cu and Au films are reported and agree with bulk values. The thermal conductivity of the thin low stress silicon nitride is substantially smaller than thicker membranes while the specific heat is enhanced below 20K. Design of the nanocalorimeter will be discussed along with fabrication details and calibration results. Reprinted with permission from *The Review of Scientific Instruments* **80**, 063901 (2009).

4.1 Introduction

Understanding the thermodynamic properties of nanoscale materials has become increasingly important as samples with nanometer length scales are routinely produced in the lab and semiconductor processing technologies shrink to tens of nanometers in size. Heat capacity in particular reveals information about electronic, magnetic, and structural properties. Measurements at the lowest temperatures tell us about the fundamental excitations in a system while measurements to several hundred degrees centigrade are typically most important for revealing phase transitions or determinations of total enthalpy and entropy. Many of these materials (e.g. amorphous, multilayers, nano-structured) cannot be produced as bulk samples and are not amenable to traditional measurement techniques. Calorimetry measurements necessarily require that the heat capacity of the calorimeter be measured along with the sample of interest. Heat capacity, c, is an extensive quantity and a calorimeter suitable for measuring these small quantities should have a heat capacity, and thus size, comparable magnitude to the nanoscale materials and films in addition to operating over a wide range of temperatures and fields.

Microcalorimeters based on amorphous, low stress silicon nitride (Si-N) membranes have been used for over a decade to understand the thermodynamics of thin films and small (micrograms) samples. [71, 72, 73, 74, 75] Heats of fusion and heat capacities of ultra thin

films and monolayers have previously been measured, but these measurements have been confined to high temperatures and zero magnetic field. [72, 76] Films as thin as 200 nm have been measured from 2-800K and in magnetic fields up to 8 Tesla with an absolute accuracy $\sim 2\%$. (See Ref. [77] and the references therein.)

Here we describe the design and fabrication of a thin film nanocalorimeter for use from 300mK to 800K and in high magnetic fields. This nanocalorimeter is a scaled down version of the previously reported microcalorimeter [71, 77] and has more than 10 times less addenda heat capacity over this wide temperature range, enabling the heat capacities of 30 nm films or sub-microgram samples to be measured with $\sim$2% absolute accuracy. [78, 75] Calibration measurements for the device will be discussed along with an analysis of the specific heat and thermal conductivity of the amorphous Si-N membrane.

4.2 Device Description

The low thermal conductance and heat capacity of amorphous Si-N membranes make them ideal for thin film calorimeters both because of their intrinsic properties (high Debye temperature and corresponding low C) and their mechanical strength (can be made extremely thin with a large area). [71, 79] These membranes are made from a low stress, silicon rich film that is grown by low pressure chemical vapor deposition (LPCVD) and they are commonly used for X-ray and TEM windows. [80]

Figure 4.1 shows a schematic (a) and cross section (b) of the new nanocalorimeter with the sample heaters and thermometers labeled. All of the elements on the device are lithographically patterned and their geometries are well known. The 2 mm $\times$ 2 mm $\times$ 30 nm Si-N membrane acts both as a substrate for the thin film sample and a weak thermal link between the sample and the Si frame. Samples are deposited onto the backside of the membrane in the 1 mm $\times$ 1 mm sample area through a microfabricated deposition mask, shown in Figure 4.1 (b). A Cu or Au thermal conduction layer is also deposited on the back of the membrane in the same central sample area to ensure that the sample is isothermal with the thermometers. [78] The sample heater is used to raise the temperature of the sample area from fractions of a degree to several hundred degrees above the frame temperature depending on the measurement technique.

The heat capacities of the membrane, thermal conduction layer, and sample, when present, are the dominant contributions to the total measured heat capacity, c_T. The background, or addenda, heat capacity of the calorimeter, c_a, is due to the membrane, conduction layer, and thin film heaters and thermometers. The thermal link, K, that couples the sample area to the environment includes contributions from thermal conduction and radiation. The thermal conduction term depends on the elements that connect the sample area and the frame: Si-N membrane and Pt leads for the heater and thermometers. Heat loss due to radiation becomes appreciable above 100K and depends on the membrane area and emissivity. [6]

The ability to reliably make thin membranes with a large area sets the minimum possible size for the calorimeter. Here we describe how the important device properties should scale in terms of the device parameters: membrane thickness t and width x. In scaling down the microcalorimeter to reduce c_a, the membrane's strength is kept relatively

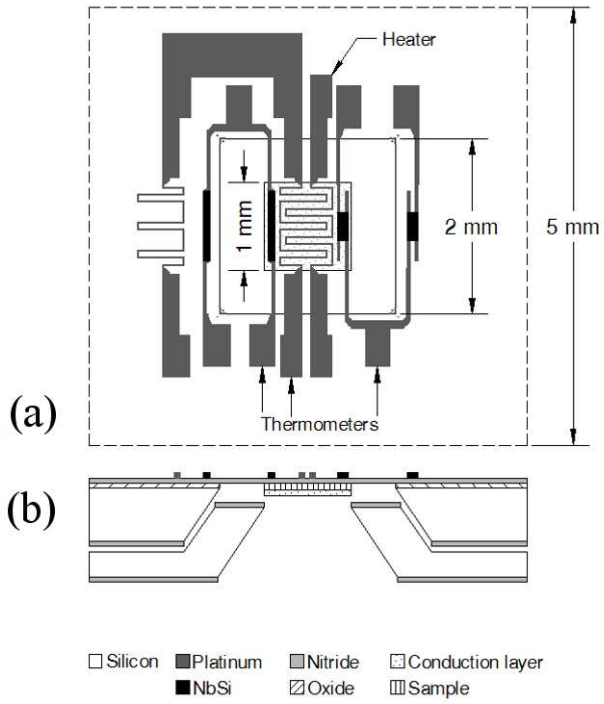

Figure 4.1: Schematic of the nanocalorimeter. (a) The sample and conduction layer are in the 1×1 mm^2 square at the center of the 2×2 mm^2 membrane. The silicon chip is 5×5 mm^2. Three sample thermometers (two a-Nb_ySi_{1-y} and one Pt) are located on the sample area with impedance matched thermometers on the frame. Each thermometer's resistance is optimized for a different temperature range. A Pt sample heater is used for all T_0 to heat the sample area with respect to the frame. Lead resistances are <2% of the measured resistance for the heater and over the range of each thermometer. The Pt heater and thermometer are 12 μm wide. The a-Nb_ySi_{1-y} thermometers have the same doping y and resistances that differ by a factor of 12.5 due to geometry. (b) The 30-50 nm thick low stress, amorphous Si-N membrane is released by etching the Si wafer in KOH and then removing the 100 nm oxide layer in buffered HF. The 10-20 nm thick Pt film is lithographically patterned and etched prior to releasing the membrane. a-Nb_ySi_{1-y} is deposited on the wafer with released membranes, patterned, and then etched. The sample is patterned in the center of the membrane by depositing the film through a separately micromachined deposition mask.

constant by maintaining the ratio of membrane area to thickness, $x^2/t \approx constant$. [80] Membranes as thin as 30 nm are strong enough to withstand fabrication, processing, and routine handling. To meet this constraint for a 30nm membrane, where t is reduced by a factor of 6 compared to the 180 nm membrane of the microcalorimeter, the membrane area must be reduced by 6, hence from 5 mm × 5 mm to 2 mm × 2 mm, therefore reducing x by 2.5.

The reduced size of the nanocalorimeter changes two thermodynamic quantities that in turn control all the other measurement parameters: the addenda heat capacity c_a and the thermal link K connecting the sample to the environment. c_a scales in a straight forward manner as it depends only on the total mass $m = \rho V$ of the elements on the membrane. The membrane contribution scales as x^2t and is reduced by a factor of 36 for a 2 mm × 2 mm × 30 nm membrane. The in-plane dimensions of the heater, thermometers, and leads were reduced by the factor as x and their thicknesses by t_i. If the scaling of $t_i \propto t$, then the overall $c_a \propto x^2t$ which is reduced by a factor of 36. K has contributions from conduction through the membrane and the Pt leads and, for $T > 100$K, a measurable contribution from radiation. Since the device is scaled uniformly in the plane of the wafer, all contributions from conduction scale as $t_i \propto t$. (x appears in both the numerator and denominator of k, hence, canceling.) The radiation contribution $K_{rad} = \sigma\epsilon AT^3$ depends on the heated area of the membrane $A \propto x^2 \propto t$. Therefore, $K \propto t$ since both contributions separately scale as t. Thus, the heat capacity of films as thin as 30 nm can be measured by scaling the microcalorimeter's membrane thickness t by 6 and area x^2 by 6 to decrease c_a. Furthermore, this scaling results in no change in systematic error for this measurement since the systematic error depends on the ratio of the thermal conductances of conduction layer and membrane which both scale at t. [77]

The measurement sensitivity is determined by the off-null voltage of the bridge circuit $\Delta V = I_{th}\Delta R$ where I_{th} is the current through the sample thermometer and $\Delta R = \Delta T(dR/dT)$ is the change in thermometer resistance upon heating the sample area. The reduction of t and x for the heaters and thermometers results in an increase in their resistance that scales as t^{-1}. (since all elements' lengths and widths scale as x) The sensitivity of the scaled thermometers is evaluated by considering the bridge response as the relevant figure of merit (FOM). It is shown in footnote [81] that FOM $= \left(\frac{t}{t_{th}}\right)^{1/2} \frac{T^{3/2}}{\rho^{1/2}} \frac{\mathrm{d}\rho}{\mathrm{d}T}$ where t and t_{th} are the thickness of the membrane and thermometer, respectively, and ρ is the resistivity of the thermometer. For the Pt thermometer, where t/t_{th} and $\rho(T)$ are both constant, FOM = *constant* and there is no loss of sensitivity upon scaling. For the low temperature *a*-Nb_ySi_{1-y} thermometers, both t/t_{th} and ρ were varied to optimize the sensitivity while keeping the resistance at a measurable value, typically, < 1 MΩ. This will be further discussed in section 4.3.

4.3 Fabrication

The thin film nanocalorimeters are fabricated in the U.C. Berkeley Microfabrication Laboratory on four inch (100) silicon wafers using MEMS processing techniques with modifications required to protect the thin Si-N before and after releasing the membranes. A 100 nm oxide layer is grown by wet oxidation of both sides of the Si wafer at 1000°C. This

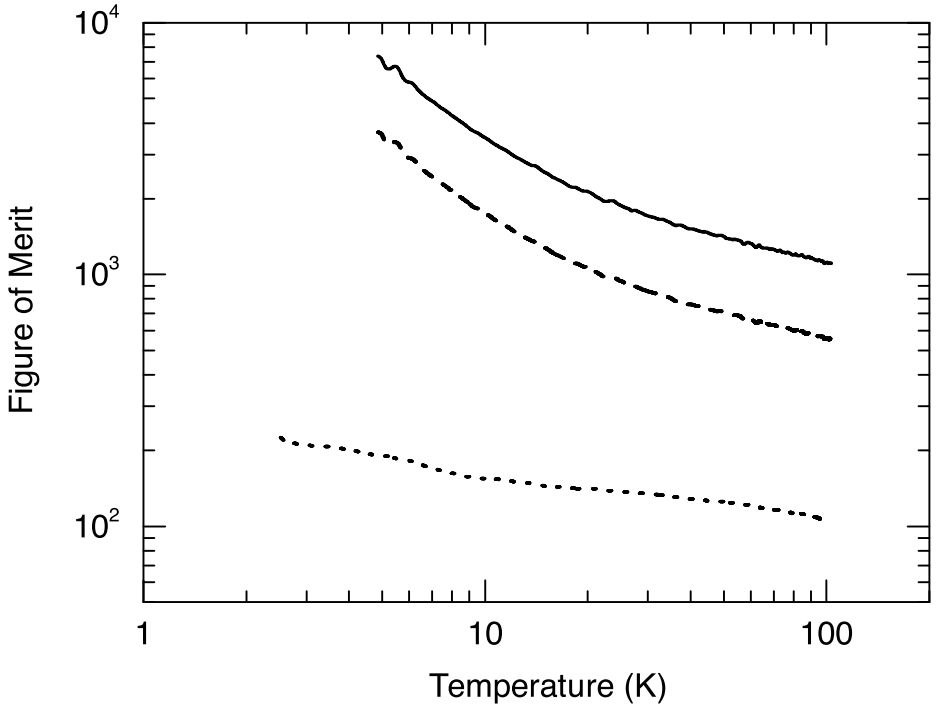

Figure 4.2: Low temperature sensitivity figure of merit FOM $= \left(\frac{t}{t_{th}}\right)^{1/2} \frac{T^{3/2}}{\rho^{1/2}} \frac{\mathrm{d}\rho}{\mathrm{d}T}$ of the nanocalorimeter using a-Nb_ySi_{1-y} thermometers. The predicted nanocalorimeter FOM (solid line) which is the same as the microcalorimeter, FOM for $\frac{t}{t_{th}} = \frac{1}{6}$ and $\rho = constant$ (dashed line), and the measured FOM with $\frac{t}{t_{th}} = constant$ and ρ decreased to reduce the thermometer resistance below 1MΩ.

oxide layer reduces the capacitive coupling between the heater, thermometers, and ground through the silicon wafer. The oxide is etched from the back of the wafer using 5:1 buffered HF (BHF) and low stress amorphous Si-N is deposited at 835°C in a low pressure chemical vapor deposition (LPCVD) furnace using a 4:1 mixture of dichlorosilane and ammonia. The Si-N on the front surface of the wafer forms the membrane and the Si-N on the back is the mask for the subsequent silicon etch. Scratches in the thin Si-N film will result in unwanted etching of the Si therefore a 200 nm film of Cr is deposited on the back surface of the wafer to protect the Si-N during processing. A Pt film is sputtered onto the front of the wafers where the heaters, thermometers, and leads are lithographically patterned and then etched in aqua-regia at 85°C. The front surface of the wafer is then protected with photoresist and the Cr film is removed from the backside. The Si-N on the back of the wafer is patterned and etched. The membranes are released by etching the exposed Si in KOH at 80°C. The top surface oxide layer is removed from the back of the membrane in 5:1 BHF leaving the clean bottom surface of the Si-N as a growth surface for future sample deposition. Vacuum

chucks are avoided for the remainder of the processing as the membranes are somewhat fragile. The low temperature a-Nb_ySi_{1-y} thermometers are cosputtered, annealed, patterned, and then etched in an SF_6 plasma. Thicknesses of the Pt, a-Nb_ySi_{1-y}, oxide, and Si-N are measured either with a profilometer or optical reflectometer. A batch consists of 6-18 wafers with each wafer holding 52 devices and yields are typically 85%.

Residual stress is kept below 200 MPa for all films to reduce strain on the membranes. The stress in the LPCVD Si-N depends on the deposition temperature and ratio of dichlorosilane and ammonia precursor gases. [80] The stress in the sputtered Pt and a-Nb_ySi_{1-y} films is controlled by varying the pressure of the argon gas. [82] Film stresses are determined by measuring the Si wafer curvature before and after film deposition with a Tencor FLX-2320.

The resistance of the a-Nb_ySi_{1-y} thermometers is a function of both doping y and annealing temperature T_A. [83] Annealing the devices ensures that they are thermodynamically stable and thus reproducible for sample preparation or measurements below T_A. A device's operating temperature range is determined by the choice of y and T_A. Thermometers with $R \simeq 1$ MΩ at 300mK can be obtained for $y \simeq 0.1$ when $T_A = 300$°C. The operating temperature range can be expanded by increasing both y and T_A. Low temperature thermometers have been reliably produced by annealing films with $y \simeq 0.13$ at 500°C. [83] Figure 4.2 shows the predicted FOM for the a-Nb_ySi_{1-y} where $\frac{t}{t_{th}}$ and ρ are both held constant. By holding ρ constant and decreasing $\frac{t}{t_{th}}$, the thermometer resistance increases above 1 MΩ and the FOM decreases. y was increased to compensate for the increased thermometer resistance but this resulted in a decrease in the FOM. The FOM for these thermometers can be further improved by annealing above 300°C and by decreasing y and increasing t_{th} for future devices.

Samples and conduction layers are vapor deposited onto the small central sample area of the membrane using a micromachined deposition mask. A 5 μm gap between the deposition mask and membrane is used to keep the error in sample area to $\leq 1\%$ from typical shadowing effects during growth. These deposition masks are fabricated from six inch silicon wafers with a nominal thickness of 650 μm. The wafers are coated with 400 nm of Si-N, patterned on the front and back, and etched in KOH at 80°C. The resulting mesa structure fits in the etch pit on the nanocalorimeter and has a through wafer opening in the center that defines the 1 mm × 1 mm sample area. Appropriate choice of convex corner compensation is required to prevent undercutting the mesa structure along the (411) planes that are exposed at the corners. The convex corner compensation method laid out by Fan [84] was found to be sufficient for this deposition mask structure.

4.4 Experimental Method

The nanocalorimeter is either mounted into a measurement system once the sample and conduction layer are deposited or the device is attached to a sample stage with a deposition mask for in-situ deposition and measurement. In either case, the device is clamped to a Cu block with a small amount of either Apiezon N or H grease applied to the block to ensure good thermal contact. The device can be operated over a temperature range of 300mK to 800K when they are prepared as described above. Electrical connections

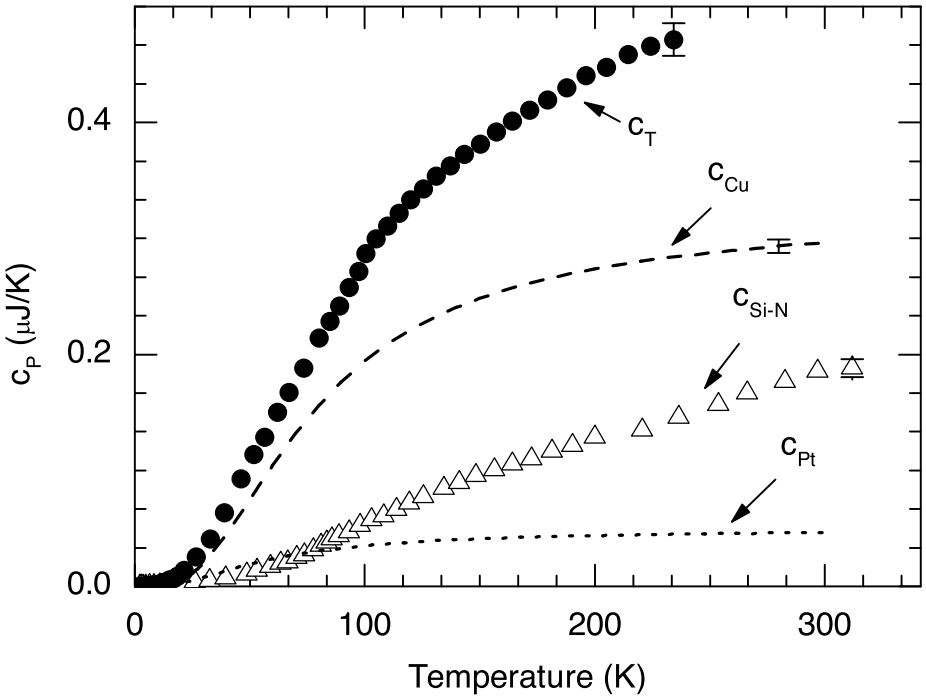

Figure 4.3: Total measured heat capacity c_T of a 50 nm thick device with 86.4 nm of Cu [contributions from: Cu conduction layer; Si-N membrane; Pt heater, thermometer, and leads; and a-Nb_ySi_{1-y} thermometers (small and not shown)]. c_{Cu} and c_{Pt} are calculated from bulk data [5]. c_{Si-N} is calculated from $c_T - c_{Cu} - c_{Pt}$. [6]

are made by gold wire bonding to the contact pads on the Si frame. A commercial Cernox thermometer and temperature controller are used to measure and control the temperature of the Cu sample block. During the measurement, each resistance thermometer on the device is calibrated to the temperature of the block thermometer. The resistance of the device sample thermometers typically vary by a small amount for devices from the same wafer. This variation is due to either thickness or, for the a-Nb_ySi_{1-y}, small composition gradients across the wafer. All measurements are made under high vacuum ($< 1 \times 10^{-7}$) to eliminate irreproducibility in c or K from small amounts of gas or ice.

The small ΔT relaxation method [85, 71, 77] is typically used for heat capacity measurements, however, the nanocalorimeter is compatible with other small sample calorimetry techniques. For this measurement, the thermal link of the calorimeter K is measured by applying a known power P to the heater and then measuring the steady state temperature rise ΔT of the sample area above the Si frame which is held at the temperature of the block T_0. Solution of the steady state heat flow equation gives $K = P/\Delta T$. P is then set to zero and the subsequent exponential temperature decay is recorded as a function of

time. The time constant of the temperature decay $\tau = c_T/K$ where $c_T = c_a + c_s$ is the total heat capacity of the calorimeter, sample, and conduction layer.

This simple model for heat flow in the device applies when the sample area is isothermal and both K and c do not change appreciably during the measurement. Temperature gradients in the sample area have been shown to be $< 2\%$ when using a conduction layer with a high thermal conductivity, such as Au or Cu, that has at least the same thickness as the membrane. [78] Changes in K and c are kept sufficiently small with the appropriate choice of ΔT. For the steady state measurement of K, ΔT in the range of $1 - 10\%$ of T_0 maintains the linearity of K over the temperature interval T_0 to $T_0 + \Delta T$. For the temperature decay, ΔT of 1-2% of T_0 is used and results in an error in c that is $\leq 0.01\%$. A detailed discussion of this technique along with a comparison to both a 1D model and 2D numerical simulation are reported elsewhere. [85, 71, 78, 77]

To measure ΔT, either the Pt or one of the a-Nb_ySi_{1-y} sample thermometers (depending on temperature T_0) is connected to a lock-in amplifier through an auto-balancing bridge which references a matching thermometer on the device's frame. (See Figure 4.1) The temperature of the block is held stable at T_0, the bridge is balanced, and the resistance of the sample thermometer is measured along with the temperature of the calibrated block thermometer. The bridge is then driven off balance by an amount ΔV when power P is supplied to the sample heater. ΔT of the sample is then determined from the measured $R(T)$ calibration for the sample thermometer. [71, 86] For a given T_0, several heater powers are applied corresponding to $\frac{1}{2}\Delta T, \Delta T, \frac{3}{2}\Delta T, 2\Delta T$ to test linearity of K around $T_0 + \Delta T$.

A Signal Recovery model 7265 DSP Lock-in amplifier provides the excitation voltage for the bridge and records the relaxation time constant τ using an internal fast A/D converter. An excitation frequency of several hundred Hz to a few kHz is used for measurement of the decay. Between 25 and 100 decays are averaged at a single temperature. The resistance of the a-Nb_ySi_{1-y} sample thermometer is 500 kΩ-1 MΩ at low temperatures and this leads to an RC attenuation of the off-null voltage of the bridge for frequencies above ~ 3 kHz. This attenuation is acceptable for the time dependent measurement as only the time constant of the decay is important but it is unacceptable for K where an accurate measure of ΔV of the bridge is needed to determine ΔT. A low frequency, typically 17 Hz, is therefore used for the steady state measurement to avoid this RC attenuation.

Usually, one nanocalorimeter per wafer is measured (with a conduction layer) to determine c_a for all devices from the wafer. The remaining devices have both a sample and a conduction layer deposited on them. The sample's heat capacity, c_s, is determined by subtracting the addenda from the total measured heat capacity, $c_s = c_T - c_a$. The small variations in c_a for each device due to differences in Pt and conduction layer thicknesses between the addenda and sample devices are calculated and corrected.

The data presented below are for devices with varying conduction layer thicknesses and materials. The membrane thickness for these nanocalorimeters is 50 nm though devices with 30 nm membranes have been fabricated. Additionally, process variations resulted in the thickness of the Pt heater and thermometers being greater than the desired value from scaling. The increased thickness of Pt increases c_a and the conduction term in K. All measurements were performed in a ^{4}He cryostat over the temperature range 2-300K. The resistance of the a-Nb_ySi_{1-y} thermometers were successfully measured down to 300mK in

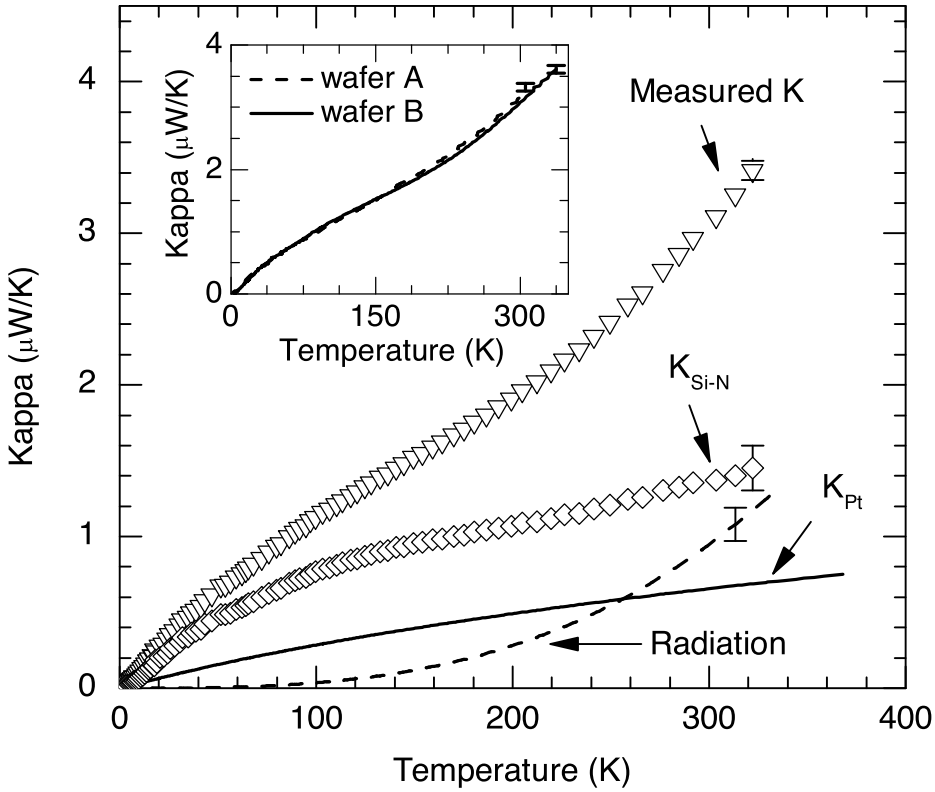

Figure 4.4: Measured total thermal link $K = P/\Delta T$ of a 50 nm nanocalorimeter shown with the contributions from Si-N membrane, Pt leads, and radiation. K_{Pt} is calculated using the Wiedemann-Franz law with the measured $\sigma(T)$ of the Pt heater. K_{Si-N} is calculated by subtracting the contributions from Pt leads and radiation. K_{rad} is taken as the T^3 term in $K - K_{Pt}$. [6] Inset: K for two devices from different wafers in same process lot.

a ^{3}He cryostat. The Pt thermometers were tested up to 800K in vacuum both by raising the temperature of the sample block and monitoring the resistance of thermometer and also by holding the sample block and silicon frame of the calorimeter at room temperature and heating the sample area of the membrane up to 800K. For the remainder of the paper, we will refer to the heat capacity of the Si-N membrane, heaters, and thermometers as the addenda and treat the conduction layer as the sample. It should be noted that a measurement of a device without a conduction layer is not meaningful since the isothermal criterion is not satisfied.

4.5 Results

Figure 4.3 shows c_T for a device with 86.4 nm thick Cu conduction layer. Also shown are calculated c for each component; Si-N membrane, Pt elements, and Cu conduction layer. The heat capacity of the a-Nb_ySi_{1-y} thermometers is not shown; as previously discussed in Ref. [6] as it makes a negligible contribution. For this sample, the bulk specific heats of Cu and Pt are used to calculate the corresponding thin film contributions which is a reasonable assumption given the results presented below [5]. c_{Cu} is shown for the thickness of Cu in the 1 mm $\times$ 1 mm sample area. c_{Pt} is a combination of c for all of the Pt in the sample area along with 29% of c for the Pt on the membrane border. This geometric factor for the border contribution is a result from 2D heat flow simulations. [78] The Si-N's heat capacity is calculated from $c_{Si-N} = c_T - c_{Cu} - c_{Pt}$. Knowing each of these contributions allows c_a to be calculated for any device to within 2% as is demonstrated below.

Figure 4.4 shows the temperature dependence of K, the measured thermal link of the nanocalorimeter, and the various components that contribute to this value. Measurements of K for devices from the same wafer agree to within 3%. The inset in Figure 4.4 shows K for devices from wafers A and B that are from the same process lot. Variations in the thickness of the Pt and Si-N account for the difference between the measured K. The thickness differences between wafers for the Si-N and Pt are 1.5% and $\leq$ 10%, respectively. Correcting for these different thicknesses reduces the variation to $\leq$ 2% which is within the measurement error.

The contributions to K shown in Figure 4.4 were calculated following the procedure detailed in Ref. [79]. The thermal conductance of the Pt leads K_{Pt} is calculated from the thermal conductivity given by the Wiedemann-Franz law ($k/\sigma = L_0T$). The electrical conductivity σ of the Pt is calculated from the measured $R(T)$ of the Pt heater which, along with the thermometers and leads, is lithographically patterned and its geometry well known. K_{Pt} is subtracted from K and the resulting curve is fit to a functional form $a+bT+cT^3$ above 100K. The cubic term is assumed to be due to the leading term in the radiation contribution $P_{rad} = A_{eff}\epsilon\sigma[(T_0 + \Delta T)^4 - T_0^4] \approx A_{eff}\epsilon\sigma T^3\Delta T \equiv K_{rad}\Delta T$ with $K_{rad} = A_{eff}\epsilon\sigma T_0^3$. From this we can find the contribution from the Si-N $K_{Si-N} = K - K_{rad} - K_{Pt}$. [6] The contribution from K_{rad} scales as the exposed surface area A_{eff} and is in good agreement with the predicted reduction of x^2.

Heat capacity measurements were also made on 52.5 nm and 30.3 nm thick Cu films and a 54.6 nm Au film. In all cases, the temperature decays were verified to be single exponential over 6τ. The nanocalorimeter for the Au film was from wafer A and the nanocalorimeters for the Cu films were from wafer B. All of the sample films were grown by thermal evaporation at a base pressure of 2×10^{-6} Torr and a deposition rate of 2-5 Å/s. Film thicknesses were monitored during growth with a quartz crystal thickness monitor and verified by measuring the thickness of a neighboring sample with a KLA-Tencor Alphastep IQ surface profilometer. The uncertainty in film thickness is 1.5% for these samples.

Figure 4.5(a) shows C_s for several thicknesses of Cu. Here we choose to find C_s by taking the difference between τ for each of the measured samples and multiplying the result by an average K for this wafer. This subtraction removes the contribution of c_a and the thinner conduction layer by treating the extra Cu of the thicker layer as the sample,

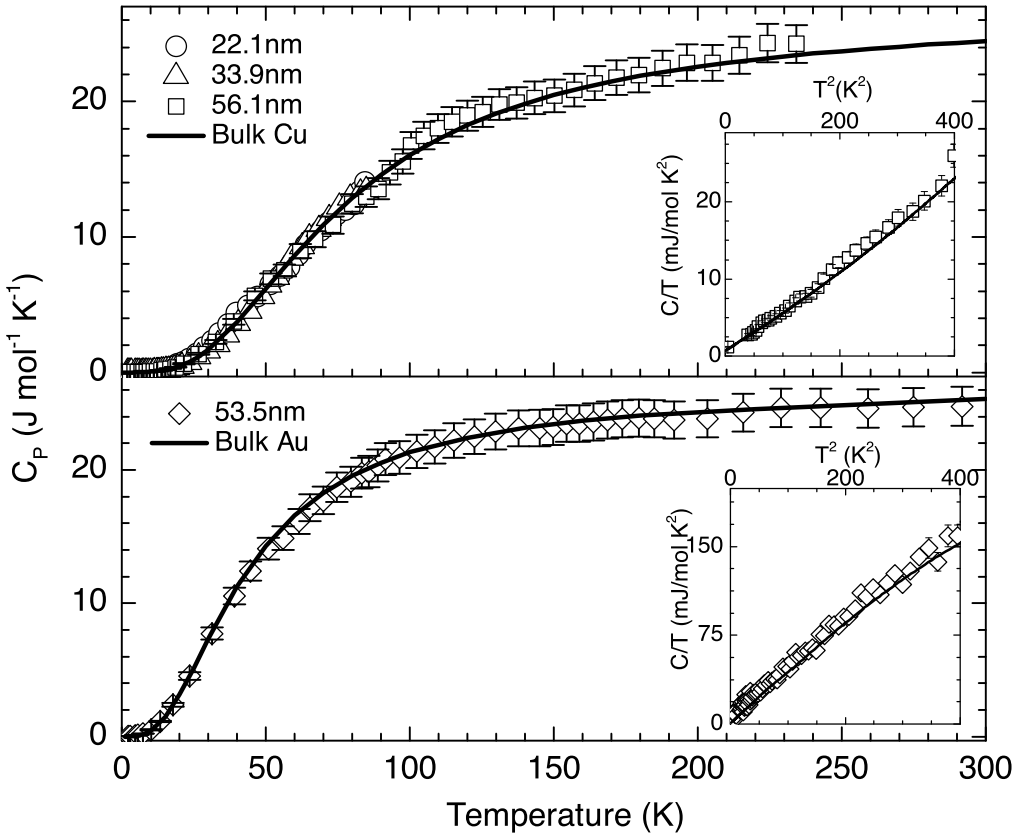

Figure 4.5: Specific heat of Cu (a) and Au (b) films of various thicknesses. Bulk values (solid lines) are from Ref. [5]. Data in (a) is the difference between devices with thick and thin Cu films. The specific heat of Au (b) was determined as described in the text. Insets: C/T vs. T^2 for 56.1 nm Cu (a) and 56.3 nm Au (b).

e.g.

$$\begin{aligned} c_{\mathrm{Cu}}^{33.9\ \mathrm{nm}} &= c_T^{86.4\ \mathrm{nm}} - c_T^{52.5\ \mathrm{nm}} \\ &= K^{86.4\ \mathrm{nm}}\tau^{86.4\ \mathrm{nm}} - K^{52.5\ \mathrm{nm}}\tau^{52.5\ \mathrm{nm}} \\ &= K\left(\tau^{86.4\ \mathrm{nm}} - \tau^{52.5\ \mathrm{nm}}\right) \end{aligned}$$

since K for each device was measured to be the same, and similarly for 56.1 nm = 86.4 nm − 30.3 nm and 22.2 nm = 52.5 nm − 30.3 nm. The assumption of an average K, and thus c_a, introduces an additional error that depends on small differences in Pt lead thickness for each device. The resulting data are normalized to their molar mass and are in good agreement with the literature values for bulk Cu which is shown as well [5].

Figure 4.5(b) shows C_s for a 54.6 nm thick Au film. For this sample, c_a was calculated as described above based on the measured thicknesses of the Si-N and Pt for this

wafer compared to wafer B. The specific heat for bulk Au (Ref. [5]) is shown and is in good agreement with the measured value. This agreement validates the differential method for measuring heat capacity along with verifying that the extracted heat capacity of the Si-N is correct since $C_{\mathrm{Cu}}(T)$ is very different than $C_{\mathrm{Au}}(T)$. The agreement of the Cu and Au films with bulk specific heat values also indicates that both electronic and lattice contributions to the specific heat are not changed for films as thin as 30 nm.

We turn now to the intrinsic values of k and C for the Si-N extracted from the measured values of K and c_a. [79] We use the results of 2D heat flow simulations that show how contributions from the membrane border area need to be considered. [78] The intrinsic thermal conductivity of the Si-N $k_{Si-N} = K_{Si-N}/\alpha t$ where t is the thickness of the Si-N and $\alpha = 10.33$ is a geometric constant obtained from the simulations, somewhat equivalent to the ratio of the path length to width. The intrinsic specific heat of the Si-N, C_{Si-N}, is calculated from c_{Si-N}. From the 2D simulations, the effective volume of Si-N is the sum of the central sample area and border contributions, $V_{eff} = [1\ \mathrm{mm}^2 + 0.24((2\times2)-(1\times1))\ \mathrm{mm}^2]\times 50$ nm where 0.24 is a geometric factor taken from the simulations in the limit of a good thermal conduction layer, as here.

Figure 4.6(a) shows the thermal conductivity of Si-N for a 50 nm and several 200 nm membranes. [79] The thermal conductivity for 200 nm membranes below 10K was reported to be sensitive to the surface roughness of the membrane which is primarily determined by oxide preparation technique. [79] Phonon scattering from the rougher surfaces is believed to be diffuse and leads to a decrease in thermal conductivity. k for the nanocalorimeter's 50nm membranes is reduced over the entire measured temperature range up to a factor of 3 when compared to 200 nm membranes prepared under similar conditions. The reduction in k is likely due to boundary scattering of long wavelength phonons from the surfaces of the membrane. Recent thermal conductivity measurements of an a-Si:H film using time-domain thermoreflectance have shown that a large fraction of the room temperature thermal conductivity is due to phonons with wavelengths of several nanometers and mean free paths of hundreds of nanometers. [26] We suggest therefore that boundary scattering in the thinner nitride films reduces the mean free path of the phonons which in turn reduces k over the entire measured temperature range.

Figure 4.6(b) shows the specific heat (J g^{-1} K^{-1}) of the 50 nm Si-N compared to 200 nm Si-N membranes. Above 20K, C_{Si-N} for both samples agrees to within a few percent and rules out any thickness errors that might account for the discrepancy seen in k. Below 20K, the 50 nm films show an increase in C as compared to 200 nm films.

Rutherford Backscattering (RBS) measurements for Si-N films reported here and previously [6] show the stoichiometry to be $\mathrm{SiN}_{1.15\pm0.05}$ with ≤ 1 at. % hydrogen as measured by hydrogen forward scattering (HFS) in agreement with previous results. [87] The density, also determined from RBS, for these films is $\rho = 2.68 \pm 0.07$ g/cm^3. There was no depth dependance to the composition found from the RBS measurements. The index of refraction, which is a measure of film composition and stress, measured by spectroscopic ellipsometry is 2.15 ± 0.05 for all of these films as well. [80] From these measurements, all of the films in Fig. 4.6 appear to be very similar chemically and it seems unlikely that any remaining small variations in stoichiometry or density would lead to the differences seen in k and C.

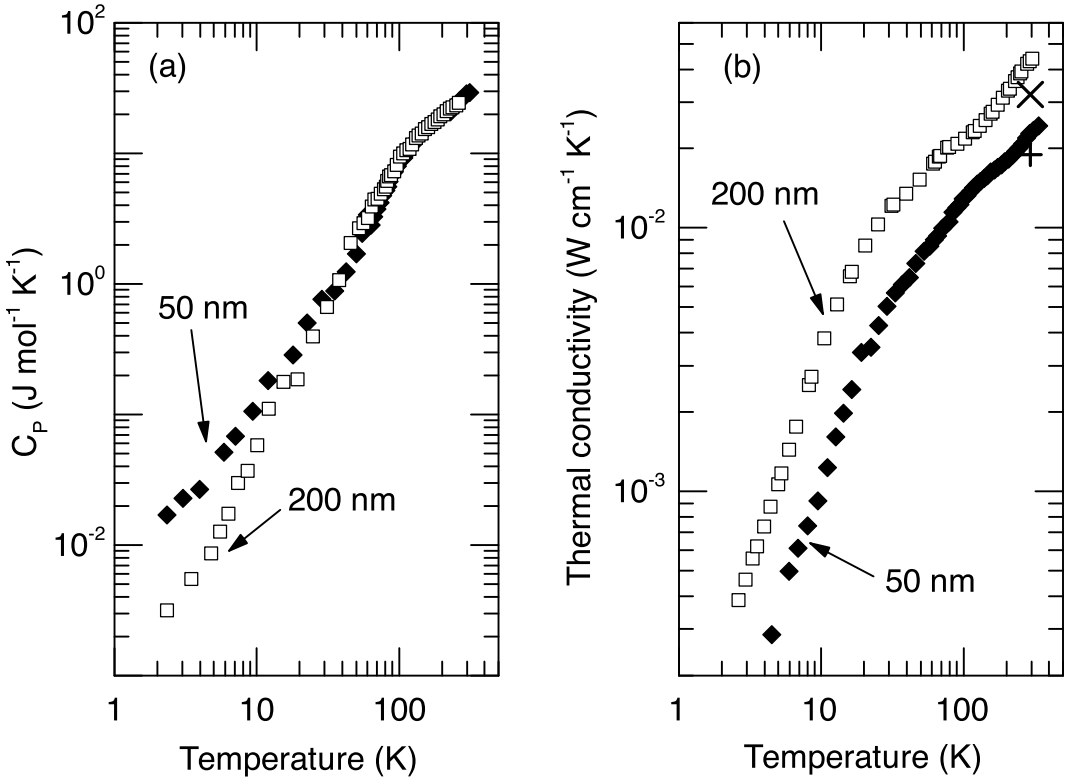

Figure 4.6: Thermal conductivity (a) from 50 nm Si-N membranes (◆) compared to values for 200 nm membranes (□) grown in the same furnace as the 50 nm membranes and previously reported 200nm films (circles and triangles) [6]. Room temperature values for 200 nm (×) and 50 nm (+) are measured by the time-domain thermoreflectance technique [7]. Specific heat (b) from 50 nm (◆) and 200 nm (□) Si-N membranes.

Room temperature acoustic measurements on the 50 nm films give the longitudinal speed of sound $v_l = 11.7 \times 10^5$ cm/s which is $\sim 6\%$ larger than v_l for 200 nm thick Si-N [6, 8]. The previous result from Ref. [8] are corrected here for the measured density. Room temperature measurements of k have been made on 50 nm and 200 nm Si-N films using the time-domain thermal reflectance technique. These values are systematically 14% lower than the values determined from calorimetry measurements and lie slightly outside of the room temperature 10% error bar in k that is dominated by uncertainty in the model for radiation. All of these differences are negligible compared to the factor of 3 change in k at all temperatures and the factor of 5 change in C by 2K.

Figure 4.7 shows the specific heat of Si-N plotted as $C \times \theta_D/T^3$ versus T/θ_D along with vitreous silica from Ref. [1]. Deviations from Debye like specific heat, such as a linear term below 1K in C, are commonly seen in amorphous materials [1]. The linear term, which appears as an upturn in C/T^3, is attributed to degeneracies in the amorphous matrix that

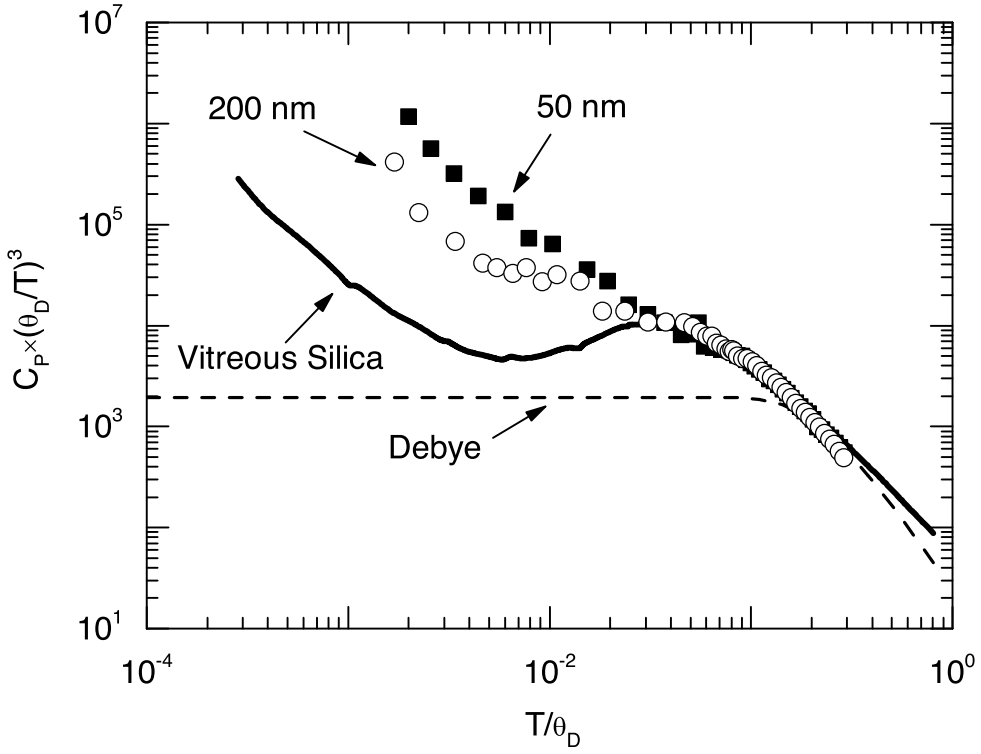

Figure 4.7: Reduced specific heat (J mol^{-1} K^{-1}) of silicon nitride (50 nm, 200 nm) and vitreous silica [1] plotted as $C_P \times (\theta_D/T)^3$ versus reduced temperature T/θ_D. The dashed line is the Debye specific heat. Debye temperatures were calculated from the measured sound velocities [8, 7, 1]

.

give rise to tunneling states and is believed to be universal to all amorphous materials [18]. The linear term in Si-N is appreciable below 6K in 200 nm films and 20K in the 50 nm films. [6] The large linear term and high onset temperature are both surprising given that Si-N appears to have a low density of tunneling states, as measured by internal friction, which is well outside of the universal regime [88, 19]. Measurements below 2K are still needed to confirm these results.

From a measurement perspective, the reduction of k_{Si-N} is beneficial as a decreased thermal conductance leads to increased thermal isolation of the sample. This means that c_a can be reduced by using a thinner conduction layer and still satisfy the isothermal condition for 2% accuracy. [78] However, the increase in C_{Si-N} below 20K results in an addenda that is 5 times larger than expected at 2K.

4.6 Conclusions

A thin film nanocalorimeter for measuring the heat capacities of 30 nm thin films with $\sim 2\%$ absolute accuracy has been designed, fabricated, and tested. We present heat capacity measurements from 2-300K; device thermometry has been tested from 300mK to 800K. Heat capacities of several Cu and Au films were measured and show that the nanocalorimeter can be used to measure the heat capacities of films as thin as 30 nm with absolute accuracy $<5\%$, limited by a combination of electrical noise, film thickness uncertainty, and $\leq 2\%$ systematic error from the measurement technique. The specific heat and thermal conductivity of the thin amorphous silicon Si-N membrane have been extracted and compared to data on thicker membranes. k is reduced by approximately a factor of 3 over the entire temperature range while an increase in C is found below 20K and is a factor of 5 at 2K. The data presented here for amorphous Si-N and recent results for a-Si:H suggest that the current models for amorphous materials may need to be revisited as new measurement techniques such as this allow investigations of materials not available for bulk measurement techniques. When scaling down the thin film calorimeter, it was necessary to optimize the electrical and thermodynamic response of the device around the strength of the supporting Si-N membrane. It is possible to further reduce the size of the calorimeter, however, the ability to reliably make ultra thin membranes will determine the lower limit on the membrane thickness and, thus, set a lower bound on the heat capacity of the calorimeter.

We thank David Cahill for the room temperature sound velocity and thermal conductivity measurements, Kin Man Yu for the RBS results, Chloé Baldasseroni, Zoe Boekelheide, David Cooke, Erik Helgren, Xiao Liu, and Barry Zink for helpful discussions, and the students and staff at the U.C. Berkeley Microlab for assistance with this project. This work was supported by the Director, Office of Science, Office of Basic Energy Sciences, Materials Sciences and Engineering Division, of the U.S. Department of Energy under Contract No. DE-AC02-05CH11231.

Chapter 5

Specific heat of electron beam evaporated amorphous silicon

The specific heat and internal friction of e-beam evaporated a-Si were measured to determine if this tetrahedrally bonded, amorphous material has the low energy excitations that give rise to the universal low temperature properties found in traditional glasses. Specific heat was measured from $2 - 300$K and, below 20K, an excess heat capacity is observed in some samples. Internal friction Q^{-1} measurements from $0.3 - 300$K show a plateau below 12K. The observed linear specific heat and plateau in the internal friction indicate that the two-level systems (TLS) that ubiquitous in glasses are present in some of these a-Si films. The Debye heat capacity is calculated from the measured sound velocity and in the samples with TLS we find an additional T^3 heat capacity that is proportional to the density of TLS. The density of low energy excitations is found to be highest in low density films. The high density films have Debye like heat capacity and very low internal friction. The density dependence suggests that the low energy excitations form either in voids or low density regions and are not intrinsic to the amorphous silicon network. By comparing internal friction and heat capacity measurements we find that only $1 - 4\%$ of the TLS measured in heat capacity contribute to the internal friction.

5.1 Introduction

The low temperature thermodynamic properties of amorphous, electrically insulating materials are known to be markedly different than their crystalline counterparts [1]. In addition to the T^3 Debye heat capacity calculated from the sound velocity, there is a T^3 contribution from excess harmonic modes and a linear term that dominates at low temperature. Around 10K, the so-called Boson peak is observed in the specific heat and is associated with localized transverse acoustic like vibrational modes [37]. The thermal conductivity decreases with decreasing temperature, has a plateau near 10K that is thought to come from scattering from localized vibrational modes, and at lower T decreases as T^2. The linear heat capacity and T^2 thermal conductivity have been described by a phenomenological two-level systems (TLS) model [3, 4]. This model assumes that there are low energy excitations in an amorphous material due to single atoms or groups of atoms that have

energetically similar spatial configurations. At low temperature, thermal activation over the energy barrier separating these configurations is no longer possible but a finite probability exists to tunnel through the barrier and this splits the ground state energy. It is excitations of the tunnel split ground state energy that leads to the linear heat capacity due to a constant (energy independent) density of states. The TLS model only describes the low temperature excitations and it is not clear if the excess T^3 specific heat, Boson peak, or thermal conductivity plateau are related to the TLS. Several models have tried to capture these higher temperature features including the defect model of Ref. [89] which includes local scatterers that give rise the Boson peak in specific heat and the plateau in thermal conductivity, the soft-potential model that considers quartic potentials with continuously varying barrier heights [90], and collective vibrations resulting from groups of atoms that have structural correlations that are frozen at the glass transition [91].

The low temperature specific heat of an electrically insulating glass has been found to fit well to the form [2], $C = c_1 T + c_3 T^3$. The coefficient of the linear term $c_1 = \frac{\pi^2}{6} k_B^2 n_0$ is due to the density of TLS n_0 [3, 4]. TLS densities are $\sim 10^{45} - 10^{46} \mathrm{J}^{-1}\mathrm{m}^{-3}$ in most glasses [2]. The T^3 term $c_3 = c_{Debye} + c_{ex}$ where c_{Debye} is the prefactor for the Debye heat capacity determined from the sound velocity and c_{ex} is an excess heat capacity found to date in all glasses [37]. $c_{ex} \approx 0.1 - 1 \times 10^{-4} \mathrm{J\ mol}^{-1}\ \mathrm{K}^{-4}$ and is typically within an order of magnitude of c_{Debye} [2]. A generally accepted theory for the origin of c_{ex} is missing.

The structural interpretation of the TLS model requires that the amorphous network have sufficient flexibility to accommodate structural rearrangements. Examples include the under co-ordination in certain chalcogenide glasses, Si-O-Si bridges in vitreous silica, and polymer chains. However, it should be stated that no mechanism has been identified as the source of TLS. Phillips [3] suggested that materials like *a*-Si and *a*-Ge would not have TLS due to the over-constrained nature of tetrahedral bonding. *a*-Si and *a*-Ge, however, cannot be quenched fast enough from the liquid state to form a glass so it can only be prepared by thin film deposition methods. The difficulty in preparing the several milligrams of material needed for a conventional calorimeter has meant that few results are found in the literature and these results are restricted to very low temperatures where the background heat capacity of the calorimeter is small or to thick films with poor quality.

Löhneysen's group measured the low temperature heat capacity of evaporated films of *a*-Si and *a*-Ge where they found a magnetic field dependent heat capacity below 1K [41, 42]. From the field dependence they concluded that the excess was due to exchange coupled electronic states associated with dangling bonds, not atomic TLS. The heat capacity and dangling bond density of the *a*-Ge film was reduced upon annealing and the authors interpreted this as further evidence that the excess was due to dangling bonds and not atomic TLS. By contrast, Graebner *et al.* showed that the T^2 TLS contribution to thermal conductivity of evaporated *a*-Ge scaled with the film density and suggested that the TLS were atomic in origin and associated with low density regions in the film [47, 48, 49]. The TLS in glasses may also be probed by low temperature internal friction Q^{-1} which measures the damping of acoustic waves from absorption by TLS [19]. Metcalf *et al.* showed that TLS are present in evaporated *a*-Si but at a lower density than in other glasses and that these TLS are atomic in origin since they are only weakly affected by magnetic field [53].

Above 2K, Mertig *et al.* measured the heat capacity from $2 - 50$K of 35μm sput-

tered a-Si film grown at $T_S = 300°$C with density $\rho = 2.29$g cm^{-3} and Zink *et al.* measured the heat capacity from $4 - 300$K of a 4000Å thick film grown at 45°C with $\rho = 2.09$g cm^{-3}. Neither film showed a significant linear heat capacity contribution. Mertig assumed that $c_3 = c_D$ and calculated the Debye temperature to be $\theta_D = 528$K. Zink *et al.* measured the longitudinal sound velocity from which they calculated $\theta_D = 487$K and found that $c_3 = c_{Debye}$ which implied that $c_{ex} = 0$. The disappearance of both n_0 and c_{ex} suggests that there may be a correlation between them. Both films had a Boson peak around 30K which is decreased from the peak in crystalline silicon that occurs at 40K. This decrease in the peak temperature is consistent with the decrease found in other amorphous materials [30].

In this chapter, we present specific heat C_P results from $2 - 300$K for several a-Si films grown on membrane-based nanocalorimeters by e-beam evaporation. These results show that TLS are absent in high density a-Si but present in low density a-Si with a density n_0 that depends on the Si number density n_{Si} and growth temperature T_S. These results suggest that TLS are not intrinsic to the tetrahedrally bonded network but rather occur in low density regions of the films. Additionally, there is a T^3 contribution to the specific heat that is in excess of Debye specific heat calculated from the measured sound velocities which also depends on n_{Si} and T_S. A correlation between n_0 and c_{ex} is found. No significant change in the heat capacity was found in magnetic field. Films with increased n_0 also have an increased internal friction Q^{-1} plateau below 12K indicating an increase in TLS. By comparing C_P and Q^{-1} we find that only $1 - 4\%$ of the TLS are strongly coupled to acoustic waves which is lower than what is found in traditional glasses.

5.2 Experimental Procedure

Amorphous silicon thin films were prepared by e-beam evaporation at a base pressure of $\sim 1 \times 10^{-8}$Torr, with a source to substrate distance of 36cm, and a growth rate of $0.5 - 1$Å/s. Growth temperature T_S was varied from $45° - 400°$C. Films were grown on nanocalorimeters, MgO, high resistivity silicon, oxide coated silicon and nitride coated silicon substrates. After evaporation of the a-Si onto the nanocalorimeter, a 200Å a-AlO_x film was sputtered onto the sample followed by a 300Å thermally evaporated Cu conduction layer. The a-AlO_x layer is used as a diffusion barrier between the a-Si and Cu films. One film (1120Å thickness) grown at $T_S = 45°$C did not have the a-AlO_x layer. This film was not annealed and there was no visible sign of alloying between the copper and silicon. The films were deposited through a micromachined deposition mask to confine the film to the 1×1mm^2 sample area of the nanocalorimeter [70]. A nanocalorimeter with only the a-AlO_x and Cu films was measured to determine the background heat capacity of the addenda. Details of the nanocalorimeter fabrication process and measurement principles can be found in Chapter 4. ESR measurements were performed on films grown on high resistivity Si substrates and all films were found to have spin densities of $\sim 10^{19}$cm^{-3} with an isotropic value of $g = 2.0055$ as is typical for isolated, neutral dangling bonds in a-Si [52]. Film thicknesses were measured on a neighboring substrate with a KLA-Tencor Alpha-Step IQ profilometer with an error of $2 - 5\%$ depending on the film thickness. The uncertainty in film thickness is the dominant source of error in all measurements except at low temperatures where the heat capacity below 10K of some samples was less than 10% of

the total measured heat capacity; in that case random error in the measurement dominates.

Rutherford Backscattering (RBS) spectra were measured using the Pelletron tandem accelerator at the Lawrence Berkeley National Lab Ion Beam Facility to determine the density of the films and test for oxidation. Spectra were acquired with incident energies from $3.0-3.1$ MeV where the energy was increased to probe at oxygen resonance energy through the depth of the film. RBS spectra were modeled with the SIMNRA software package. Longitudinal sound velocities v_l were measured using a picosecond ultrasonic pump/probe technique [7].

A set of 3000Å thick films were prepared with varying T_S under the same growth conditions on high purity single crystal silicon double paddle oscillators for shear modulus G and internal friction Q^{-1} measurements from $0.3-300$K at the Naval Research Laboratory [92]. Transverse sound velocities v_t were determined from G and mass density $\rho = t^{-1}\left(N_{Si}\cdot M_{Si} + N_O \cdot M_O\right)$ measured from RBS where, t is the film thickness, M_{Si} and M_O are the atomic mass, and N_{Si} and N_O are the areal density of silicon and oxygen, respectively.

Raman scattering spectra were measured on the 3000Å films with a 514.5nm line of an Ar ion laser and a Jobin-Yvon U-1000 double grating monochromator with the slits set at 500μm for a resolution of 4.5cm^{-1} [93] to compare the degree of ordering and vibrational spectra of the films. Ar gas was flowed across the surface of the samples to suppress the rotational lines of nitrogen. The background due to scattered laser light in the monochromator was determined by measuring crystalline silicon from $20-200\text{cm}^{-1}$. The scattered light was fit to a Lorentzian and subtracted from the Raman spectra of the amorphous films.

Heat capacity measurements were performed from $2-300$K in a high vacuum cryostat using the small ΔT technique [70, 71, 77, 94]. After the initial heat capacity measurements, samples were annealed at 200°C for 10^4 seconds in the vacuum cryostat using the sample heater on the device [56]. With the silicon frame of the nanocalorimeter thermally anchored to the copper sample block at room temperature, 1mW of power applied to the sample heater on the membrane was needed to anneal the sample at 200°C. The temperature of the copper sample block increased by only 1K above room temperature due to the low power needed to heat the membrane. The heater current was incremented in $\Delta I = 0.5\mu$A steps to give a heating and cooling rate of ≤ 5K/min. Constant current steps do not lead to a constant change in temperature since the temperature rise of the membrane is $\Delta T = \frac{P}{K}$ where $P = I^2R$ is the power dissipated in the heater and K is the thermal conductance between the sample area and the frame. Radiation is the dominate conductance mechanism above room temperature and increases as T^3 whereas the heater resistance $R \sim T$. The temperature dependence of R and K result in a decrease in temperature change $\Delta T \sim T^{-2}$ of the membrane sample area with increasing T for constant current steps ΔI.

5.3 Results

The room temperature Raman spectra for the 3000Å films are shown in Fig. 5.1. Due to the lack of translational invariance in an amorphous material, the momentum se-

Sample	T_S °C	t Å	ρ g cm^{-3}	G GPa	Q^{-1} $\times 10^{-4}$	v_t $\times 10^5$cm s^{-1}	Γ cm^{-1}	$\Delta\theta$ °
T10-33	45	3029	2.08	35.1	1.7	4.11	76	10.2
T11-13	200	3078	2.04	46.1	0.58	4.75	72	9.5
T11-12	400	2990	2.20	58.0	0.026	5.13	64	8.2

Table 5.1: Summary of data for Q^{-1} and Raman scattering samples. Samples are identified by run number. T_S is the growth temperature. t is the sample thickness. ρ is the density. G is the shear modulus determined during the Q^{-1} measurements. The values of Q^{-1} at 2K are listed. The transverse sound velocity v_t is calculated from G as described in the text. Γ is the width at half maximum of the TO-like peak in Raman scattering and $\Delta\theta$ is the calculated bond angle deviation.

lection rules are relaxed and all phonons are optically active [65]. The resulting spectrum is proportional to the vibrational density of states (VDOS) which is a broadened version of the crystalline phonon density of states [95]. The transverse acoustic (TA) like peak occurs below 200cm^{-1} and this feature is often referred to as the Boson peak. The longitudinal acoustic (LA) and longitudinal optic (LO) like modes occur between $200 - 420$cm^{-1} with the transverse optic (TO) like peak centered at 475cm^{-1}. Lannin *et al.* reported that the relative intensity of the TA to the TO peak increased with increasing T_S along with a sharpening of the LA like peak. We see the sharpening of the LA and TO like peaks with increasing T_S but no change in the TA peak. The TO like peak narrows and sharpens with increasing T_S. By comparing the simulated Raman scattering from several structural models of a-Si, Beeman *et al.* showed that the RMS distortion of bond angles $\Delta\theta$ with respect to the tetrahedral angle of $\theta = 109^\circ$ can be obtained from the width of the TO-like Raman peak $\Gamma = 6\Delta\theta + 15$ where Γ and $\Delta\theta$ are in units of cm^{-1} and degrees respectively [96]. The widths of the TO-like peak are determined by measuring the half-width of the peak on the high energy side as the low energy side of the peak has a shoulder from the LO peak. The peak widths and bond angle deviations are listed in Table 5.1.

The atomic density of the a-Si films was measured with RBS. Figure 5.2 shows the RBS spectra of samples grown at $T_S = 45$°C and 200°C on MgO as a function of incident energy E_0. Scattering from the silicon gives a feature with an onset of ~ 1800keV and a width due to the Si thickness. The MgO substrate results in scattering at 1500keV from the Mg and at 1000keV for the oxygen in the substrate. Scattering from oxygen in the a-Si film is weak due to the low oxygen content and it is coincident with the Mg signal. By setting the energy to the oxygen resonance $E_0 = 3.040$MeV we are sensitive to oxygen in the top ~ 50Å of the film. The resonant scattering results in a peak in the RBS spectrum. Increasing E_0 probes deeper in the bulk of the film at the oxygen resonant energy by compensating for the energy loss of the alpha particles as they interact with the electrons in the film [97]. It can be seen from Fig. 5.2 that the oxygen resonant signal for the $T_S = 45$°C persists through the entire film until the resonance from the MgO substrate is observed. This indicates that oxygen is present throughout the 45°C film whereas the 200°C film only has oxygen near the surface.

The RBS spectra of the films was fit using a $2 - 4$ layer model with different Si–O

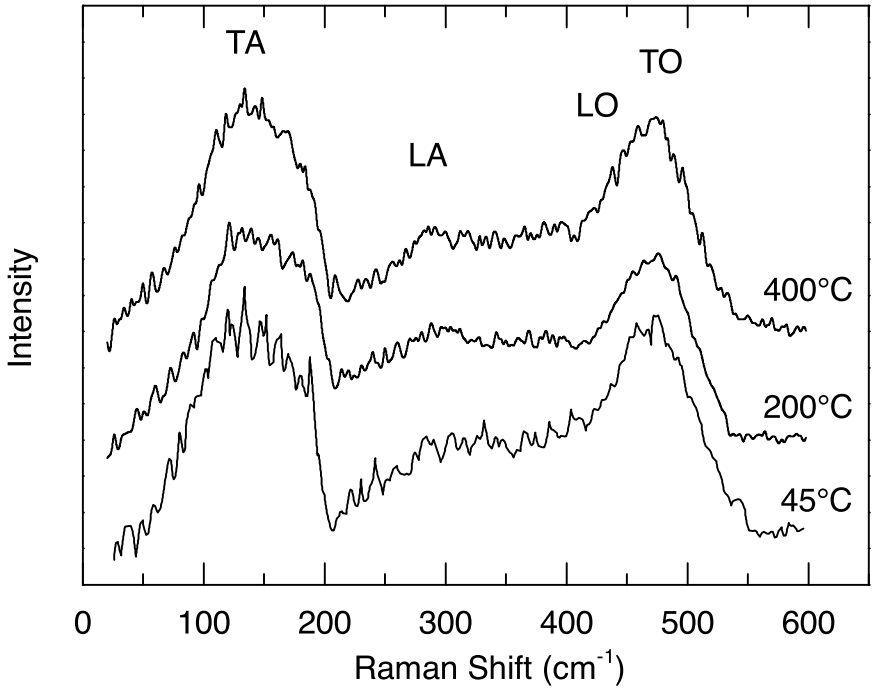

Figure 5.1: Raman scattering spectra for a-Si measured at room temperature with the Rayleigh scattered light subtracted. The film thicknesses are ~ 3000Å. The TA-like modes result in the Boson peak at 150cm^{-1} and the TO-like peak is visible at 475cm^{-1}. The TO and LA peaks sharpen with increasing T_S indicating that the local structural order in the film is increasing. The bond angle disorder is obtained by fitting the half-width of the TO-like peak as described in the text and shown in Table 5.1. There is no significant change in the TA peak with T_S.

compositions and thicknesses to account for the decrease in oxygen away from the surface of the film. The model was always constructed to use as few layers as possible to account for the oxygen concentration gradient. The summary of the modeled data is presented in Table 5.2. In all films, $\sim 10 - 30$Å at the surface could be attributed to SiO_2. The layer thicknesses were calculated assuming uniform total number density throughout the film. This assumption overestimates the thickness of the layers containing oxygen as these layers likely have a higher density due to the additional oxygen atoms. However, this overestimate is small since the oxygen in the bulk of the film was found to be only a few percent and decreases with increasing depth. This decrease in oxygen with depth is consistent with oxygen diffusion into the film after growth rather than during the growth which would result in a constant oxygen concentration through the film [98]. Higher growth temperature films were found to be denser and contain less oxygen. The mass density ρ of the film listed in

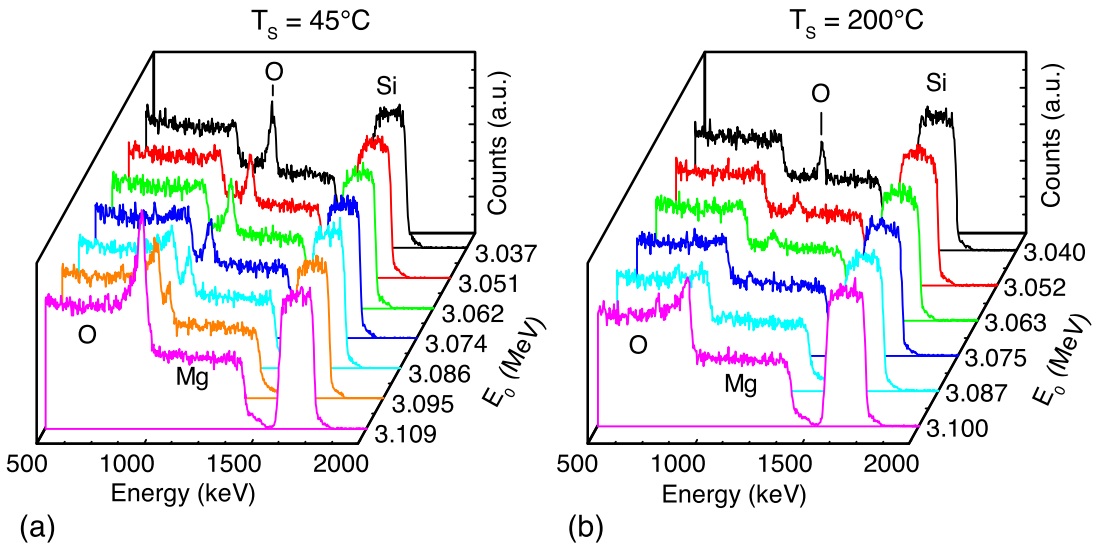

Figure 5.2: RBS spectra for films grown on MgO substrates at (a) 45°C and (b) 200°C as a function of incident energy E_0. The silicon number density in the film is determined from the area of the silicon peak which has an onset energy $\sim$ 1750keV. By setting the energy to $E_0 = 3.040$MeV α-particles resonantly scatter from oxygen in the top $\sim$ 50Å of the film. Increasing E_0 probes deeper in the bulk of the film at the oxygen resonant energy by compensating for the energy loss of the α-particles as they interact with the electrons in the film. The 45°C film has $\sim 2\%$ oxygen throughout the bulk of the film while the 200°C sample has only an oxide layer near the surface. Only a $\sim 10 - 30$Å surface layer can be attributed to a-SiO_2 and the remainder is due to an oxygen concentration gradient in the bulk of the film.

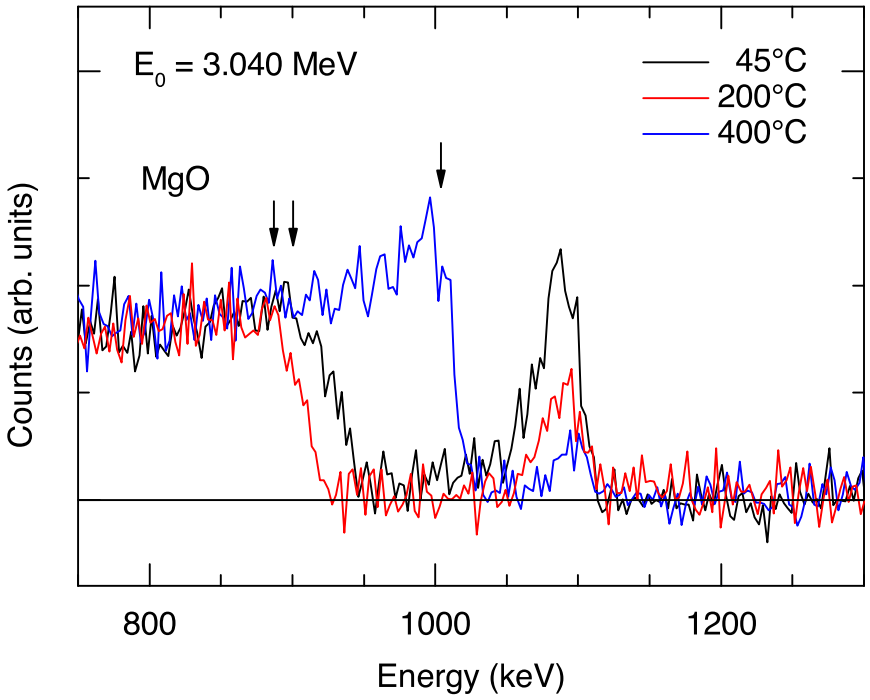

Figure 5.3: RBS Oxygen spectra for a-Si grown on MgO at 45°C (2775Å), 200°C (3191Å), and 400°C (1497Å) with the incident energy at the oxygen resonance $E_0 = 3.040$MeV. The oxygen spectrum is obtained by subtracting the model data for Si and Mg from the measured spectrum. The resonant peak is due to oxygen near the surface of the film. Films grown at higher temperature are found to have a higher Si density and lower oxygen content. The oxygen in the bulk of the film is measured by increasing E_0 as is shown in Fig. 5.2. The vertical arrows indicate the onset of the oxygen signal from the MgO substrate which shifts to lower energy due to increased energy loss in the thicker a-Si films.

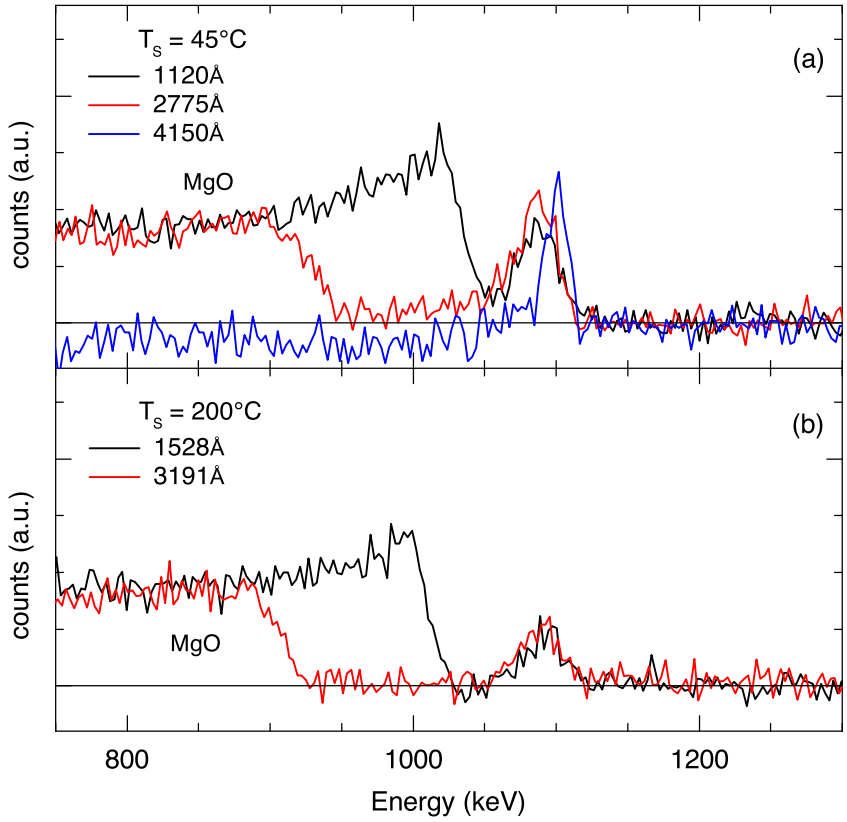

Figure 5.4: RBS oxygen spectra for *a*-Si grown on MgO at (a) 45°C and (b) 200°C for several different film thicknesses. The 4150Å film is the sample from Ref. [9] which only has a film is a 30Å surface layer of SiO_2 with no oxygen detected in the bulk of the film. This film is grown on a Si-N substrate and does not have an oxygen signal from the substrate. In the films prepared for this study the oxygen content decreases with increasing T_S.

Table 5.3 is calculated from the total areal densities of silicon and oxygen.

Figure 5.3 shows the oxygen spectra for several a-Si samples with $E_0 = 3.040$MeV which are obtained by subtracting the modeled spectra of the Si in the film and the Mg in the substrate from the measured spectrum. This plot shows that the oxygen content decreases with increasing growth temperature. The resonant peak comes from the surface oxide layer. Figure 5.4 compares the RBS oxygen spectra of films for various thicknesses with the same T_S. The oxygen spectra are similar for a given T_S indicating that the diffusion of oxygen into the films is similar for the thick and thin films. The oxygen content is likely a measure of the void density in the films. Foti *et al.* [98] demonstrated that e-beam evaporated a-Si is susceptible to diffusion of oxygen into the film through a connected network of microvoids. The RBS data in Fig. 5.3 and Fig. 5.4 show that higher T_S results in less oxygen being incorporated into the film. A notable exception is the 4150Å film grown at 45°C and reported in Ref. [9]. This film has only a ~ 30Å surface oxide with no oxygen in the bulk of the film and a mass density comparable to the higher growth temperature films. TEM measurements on this film showed no sign of voids or columnar microstructure. This film was grown in the same deposition system as the films prepared in this work and it is currently unclear why the density of this film is substantially higher. The film was found to be amorphous from x-ray and appeared uniform and dense in TEM with no sign of voids or microstructure. A TEM study is currently planned for the films reported here to investigate the microstructure further.

Figure 5.5 shows the temperature dependence of Q^{-1} for 3000Å thick a-Si films with varying T_S. The magnitude of the low temperature plateau is due to damping of acoustic waves by scattering from TLS: $Q^{-1} = \frac{\pi}{2}\left(\frac{\overline{P}\gamma^2}{\rho v_t^2}\right)$ where $\overline{P}$ is the density of TLS that are strongly coupled to acoustic waves with energy γ, ρ is the mass density, and v_t is the transverse sound velocity [14]. The magnitude of the Q^{-1} plateau decreases by orders of magnitude with increasing growth temperature. The Q^{-1} data for the 45°C film is comparable to a previously measured e-beam evaporated a-Si film grown at room temperature [10]. Also shown in Fig. 5.5 is the film grown at room temperature from Ref. [10] after annealing at 350°C for 5 hours. This annealed film is comparable to our film grown at 200°C. The shear modulus G of the film can be measured by comparing the total Q^{-1} of the double paddle oscillator before and after deposition of the film, from which $v_t = \sqrt{G/\rho}$ can also be determined [92]. As is shown in Tables 5.1, both G and ρ increase with growth temperature but their increase is small compared to the large decrease in Q^{-1} therefore $\overline{P}\gamma^2$ decreases with increasing T_S. The effect of annealing on Q^{-1} is currently under investigation.

Figure 5.6 shows v_l and v_t compared to the average of the [100] and [110] sound velocities of crystalline silicon calculated from the elastic constants [11]. The Debye temperatures are shown as a function of growth temperature in Fig. 5.7. The Debye temperature $\theta_D = \frac{\hbar v_D}{k_B}\left(6\pi^2 n\right)$ where n is the total atomic number density determined from RBS and $v_D = \left[\frac{1}{3}v_l^{-3} + \frac{2}{3}v_t^{-3}\right]^{-1/3}$.

The specific heat C_P of several 3000Å thick films is shown in Fig. 5.8 plotted as C_P/T^3 on a log-log scale to emphasize the deviation from the Debye T^3 specific heat at low temperatures which appears as a horizontal line on this plot. The films grown at 45°

Sample	T_S	t	layer 1		layer 2		layer 3		layer 4		ρ	n_{Si}
	°C	Å	Si/O	t_l(Å)	Si/O	t_l(Å)	Si/O	t_l(Å)	Si/O	t_l(Å)	g cm^{-3}	$\times 10^{22}$ cm^{-3}
T08-026	45	1120	0.33/0.67	12	0.95/0.05	485	0.97/0.03	623	-	-	1.99	4.14
T09-061	45	2775	0.33/0.67	11	0.93/0.07	856	0.96/0.04	1909	-	-	2.08	4.33
T09-063	400	1497	0.33/0.67	11	0.98/0.02	310	1.00/0.00	1175	-	-	2.09	4.47
T09-064	200	1528	0.33/0.67	11	0.94/0.06	253	0.98/0.02	528	1.00/0.00	735	2.01	4.26
T10-067	200	3191	0.33/0.67	11	0.96/0.04	341	0.98/0.02	568	1.00/0/00	2271	2.05	4.35
T11-012	400	2990	0.33/0.67	28	0.97/0.03	212	1.00/0.00	2751	-	-	2.20	4.69
T03-09	45	4150	0.33/0.67	33	1.00/0.00	4117	-	-	-	-	2.09	4.47

Table 5.2: Results from fits to the RBS spectra using SIMNRA. Samples are identified by run number. T_S is the growth temperature. t is the total film thickness. The data were modeled as multiple layers with decreasing oxygen content with layer 1 at the top and composed of SiO_2. The relative silicon and oxygen concentrations for a model layer are given along with the thickness of the layer t_l. The average number density of the film was used to calculate the model layer thicknesses. ρ is the mass density of the film and n_{Si} is the silicon number density.

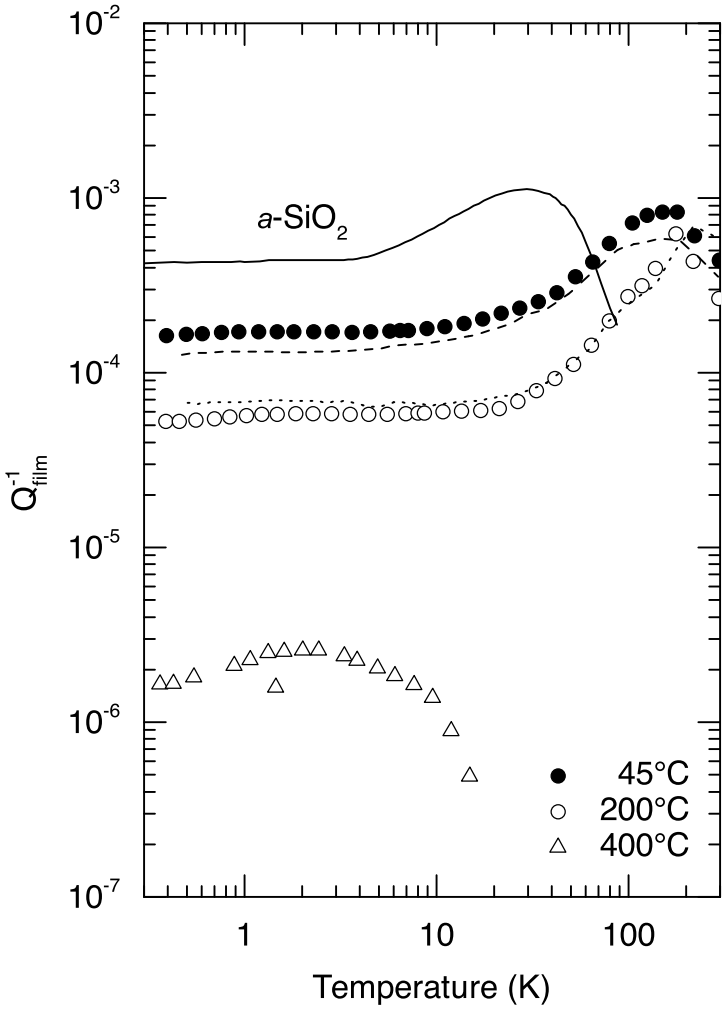

Figure 5.5: Internal friction Q^{-1} for several $\sim$ 3000Å evaporated a-Si films measured at 5500Hz. The plateau below 10K is due to those TLS with the appropriate energy splitting to scatter acoustic waves. Also shown is Q^{-1} from Ref. [10] for an e-beam evaporated a-Si film grown at room temperature (dashed line) and the same film after annealing at 350°C for 5h (dotted line).

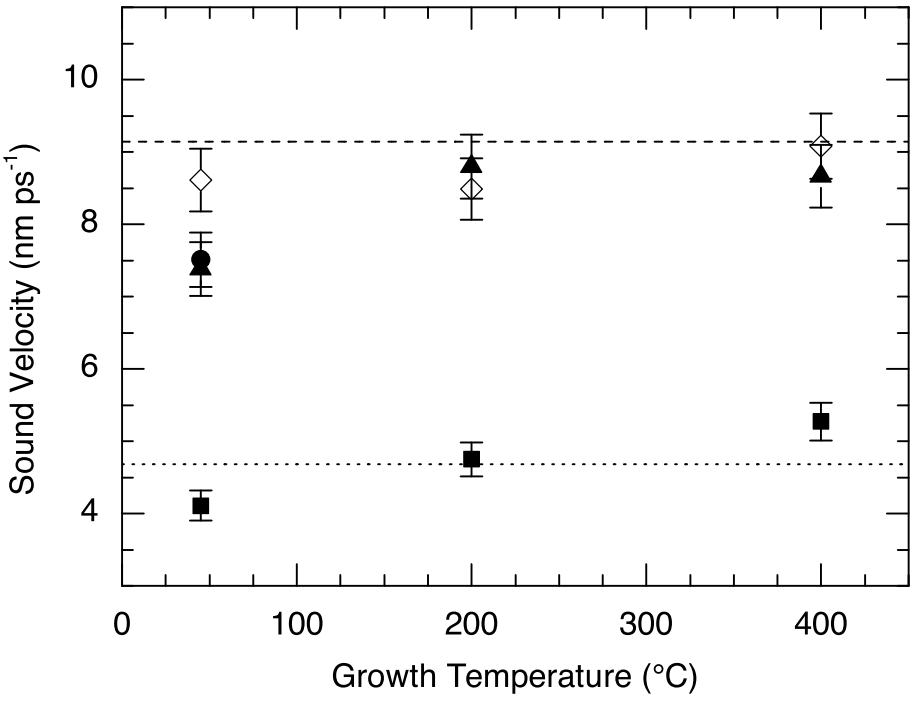

Figure 5.6: The transverse and longitudinal sound velocity of a-Si compared to the average of the [100] and [110] longitudinal (dashed line) and transverse (dotted line) sound velocities of crystalline silicon calculated from the elastic constants [11]. v_t (■) was determined from the shear modulus G and density ρ and are listed in Table 5.1. v_l was measured by an ultrasonic picosecond acoustic technique [12] v_l are shown for the thin (◇) and thick (▲) samples listed in Table 5.3. v_l for the sample from Ref. [9] is shown for comparison (●).

and 200°C both have C_P in excess of the Debye specific heat whereas the 400°C sample is close to the Debye value. Figure 5.9 shows the specific heat for films of different growth temperature and thickness plotted as C_P versus T on a log-log scale to emphasize the temperature dependence of the specific heat which decreases rapidly at low temperature. The 45°C films are compared to the results from Ref. [9] where the specific heat of a 4000Å thick e-beam a-Si film was found to agree well with the Debye specific heat. It is clear in Fig. 5.9 that the thinner films have a larger specific heat at low temperature than the thicker films. The room temperature specific heats of all films agree to within the error in thickness, confirming that the differences in the low temperature specific heat are not due to normalization errors. The excess heat capacity does not scale with the oxygen concentration as measured from RBS. The data below 12K have been fit to the form $C/T = c_1 + c_3T^2$ and the results are summarized in Table 5.3. Annealing at 200°C resulted in a reduction of c_1 by a factor of 2.5 for the 45°C film while there was no change in the $T_S = 200$°C film

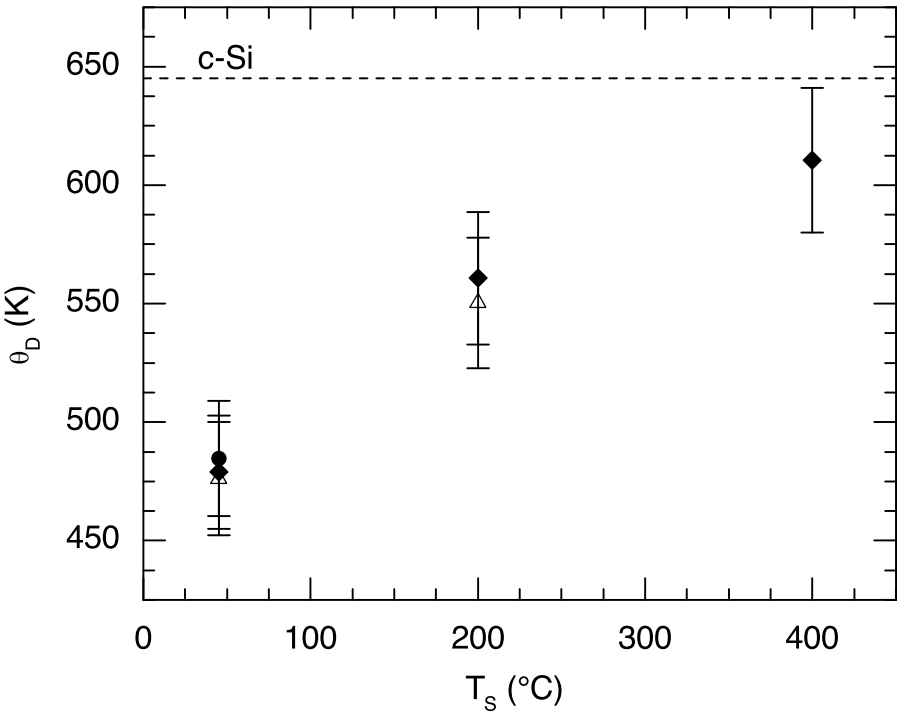

Figure 5.7: The Debye temperature θ_D as a function of growth temperature T_S for the thin ($\triangle$) and thick ($\blacklozenge$) a-Si films listed in Table 5.3. The Debye temperature is calculated from the measured transverse and longitudinal sound velocities and the total number density from RBS. Using only the silicon number density changes θ_D by $< 5\%$. The error bars are due to the uncertainties in film thickness and RBS areal density. The Debye temperature of crystalline silicon (- - -) with $\theta_D = 645$K and the film from Ref. [9] ($\blacksquare$) with $\theta_D = 487$K are shown for comparison.

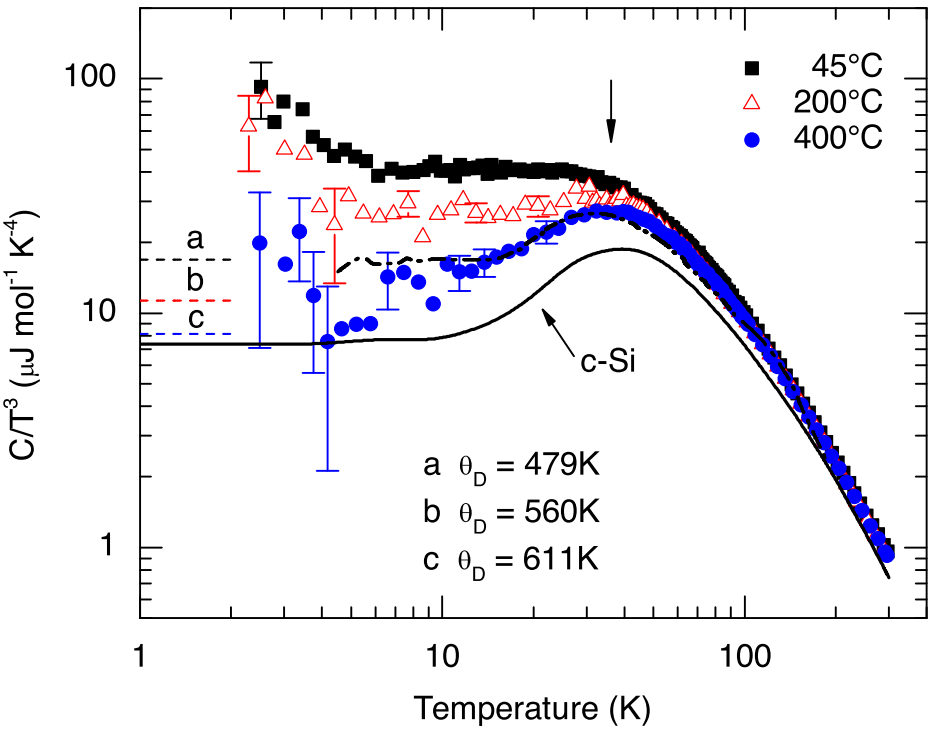

Figure 5.8: Specific heat of $\sim$ 3000Å thick a-Si films plotted as C/T^3 versus T for several growth temperatures. Only representative error bars are shown for clarity. The Debye heat capacities were calculated from the measured sound velocity as described in the text and at low temperature appear as a constant on this plot. The calculated θ_D are listed in the figure. The data for a-Si from Ref [9] (dashed-dotted line) and crystalline silicon (solid line) are shown as a reference [5]. θ_D = 645K for crystalline silicon. The specific heat of the 45°C and 200°C films is in excess of the Debye specific heat as is typical of an amorphous material while the 400°C sample is comparable to its Debye specific heat. The vertical arrow identifies the location of the Boson peak which shows no substantial dependence on T_S.

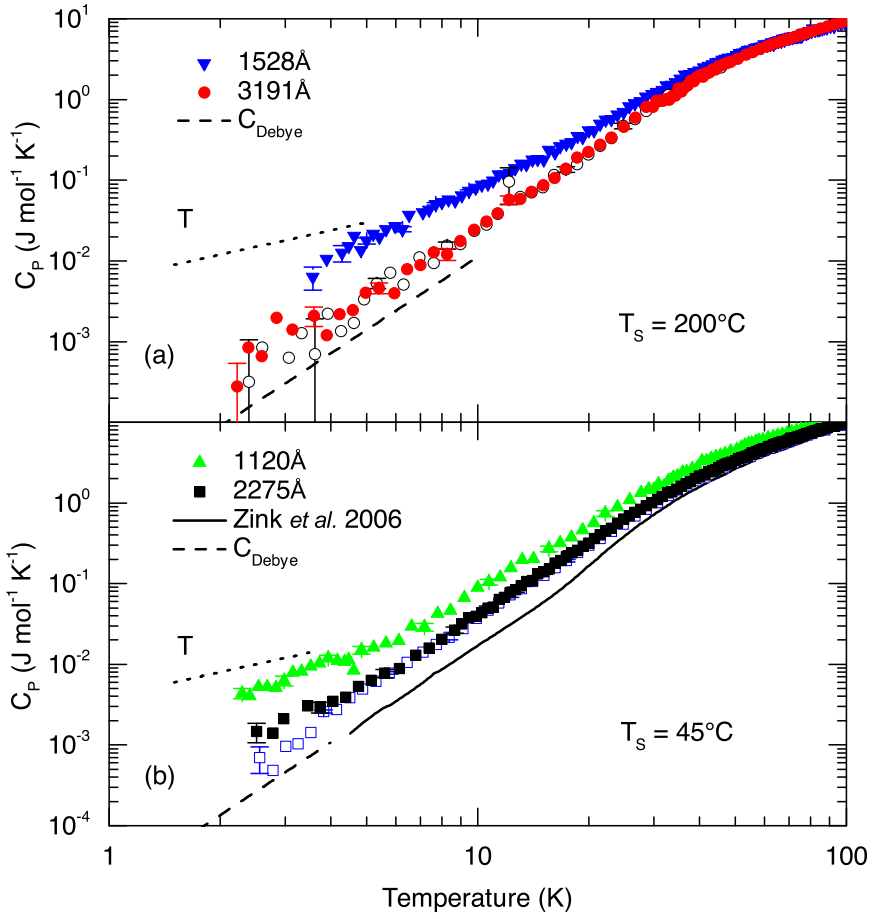

Figure 5.9: The specific heat of thick and thin films of a-Si grown at (a) 200°C and (b) 45°C. Closed symbols are as-prepared films. Only representative error bars are shown for clarity. The 200°C (3191Å) and 45°C (2775Å) films were annealed at 200°C (open symbols) for 10^4s. Annealing the 3191Å45°C at 200°C resulted in a decrease in n_0 by a factor of 2.5 but c_{ex} changed by less than 2%. Changes in the specific heat of the $T_S = 200$°C film after annealing were negligible. Also shown are the Debye specific heats (dashed line) calculated from the sound velocities of the $\sim$ 3000Å thick films. The data from Ref [9] are shown for comparison (solid line) which has film density ρ comparable to the 400°C sample (not shown) as seen in Table 5.3. A linear temperature dependence is shown for comparison (dotted line).

Sample	T_S	t	ρ	n_{Si} $\times 10^{22}$	v_l	θ_D	n_0 $\times 10^{46}$	c_{ex} $\times 10^{-5}$	n_{ESR} $\times 10^{18}$
	°C	Å	g cm^{-3}	cm^{-3}	nm ps^{-1}	K	J^{-1} m^{-3}	J mol^{-1}K^{-4}	cm^{-3}
T08-026	45	1120	1.98	4.14	8.61	476	36 ± 3	4.1 ± 0.4	6.6
T09-061	45	2775	2.08	4.33	7.38	479	4.6 ± 1.0	2.1 ± 0.1	6.0
T09-064	200	1528	2.01	4.26	8.49	550	53 ± 6	5.8 ± 0.5	6.7
T10-067	200	3191	2.04	4.36	8.80	560	4.3 ± 1.3	1.1 ± 0.2	5.8
T09-063	400	1497	2.09	4.47	9.08	-	-	-	5.1
T10-034	400	3100	2.09[a]	-	8.66	611	0.2 ± 0.7	0.4 ± 0.1	-
T03-09	45	4150	2.09	4.47	7.51	485	-	0 ± 0.8	~ 10

[a] The RBS sample for T10-034 was inadvertently used for another experiment so the density for T09-063 is used for the analysis of the heat capacity.

Table 5.3: Summary of data for heat capacity samples. T_S is the growth temperature. t is the sample thickness. ρ is the mass density determined from RBS and thickness measurements. v_l is the longitudinal sound velocity determined from picosecond acoustic measurements. θ_D is the Debye temperature calculated from the sound velocity. n_0 is the density of states of TLS as determined from heat capacity measurements. $c_{ex} = c_3 - c_{Debye}$ is the excess T^3 specific heat as explained in the text. n_{ESR} is the dangling bond defect density from ESR measurements. Sample T03-09 is the *a*-Si film reported in Ref. [9].

after annealing. Measurements were also made in high magnetic field for a film in the light soaked state and no significant field dependence was found. The results for the light soaked films will be discussed in Chapter. 7.

The heat capacity of the 2775Å film grown at $T_S = 45$°C is shown in Fig. 5.10 compared to the heat capacity of the oxide in the film assuming that all the oxygen has formed *a*-SiO_2 and has the bulk heat capacity of vitreous silica from Ref. [1]. The total number of oxygen atoms in the film determined from RBS is only 5% of the total number of atoms. The heat capacity of the SiO_2 is correspondingly small and cannot account for the increase in the low temperature heat capacity.

Figure. 5.11 shows n_0 and c_{ex}, which are determined from the fits to the low temperature heat capacity, versus the number density of silicon atoms in the film n_{Si}. Both n_0 and c_{ex} decrease with increasing n_{Si} suggesting that the increase in the low temperature specific heat is due to low energy excitations in either low density regions or voids in the film. There is no correlation when the data are compared to the oxygen content. The inset of Fig 5.11 shows that $\overline{P}\gamma^2$ decreases with increasing n_{Si} as well. n_0 versus c_{ex} is plotted in Fig. 5.12 where a correlation between the linear and excess T^3 specific heats is observed. This correlation suggests that these two features have the same origin.

5.4 Discussion

The specific heat measurements in Fig. 5.8 and Fig. 5.9 show that there are low energy excitations in evaporated *a*-Si. The density of these excitations is highest in films with a low silicon number density suggesting that they occur either in voids or low density

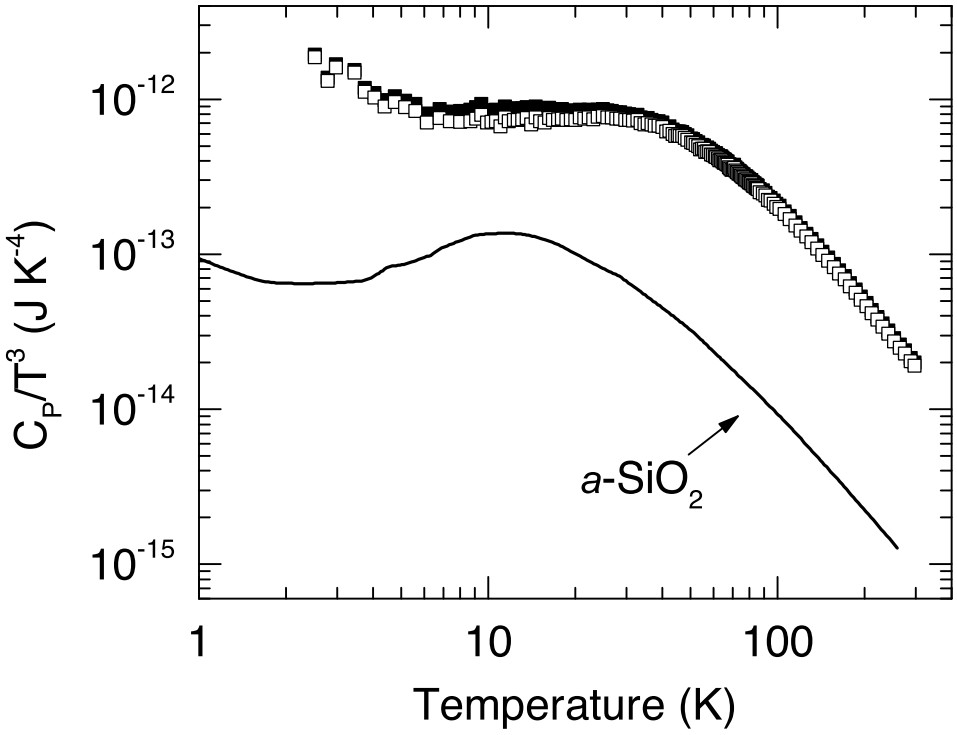

Figure 5.10: Heat capacity of the 2775Å film grown at $T_S = 45°$C plotted as C/T^3 compared to the heat capacity of a-SiO_2 assuming all of the oxygen in the film is in the form of a-SiO_2. The film is shown before (■) and after (□) subtracting the calculated heat capacity of a-SiO_2 (solid line). The bulk heat capacity of a-SiO_2 is from Ref. [1].

regions in the film and do not occur in the dense amorphous silicon network. High density films such as the 400°C film reported here and the 45°C film reported in Ref. [9] have specific heats that are close to the Debye specific heat. The Q^{-1} measurements in Fig. 5.5 show a similar decrease in the magnitude of the low temperature plateau which is consistent with a decrease in low energy excitations due to atomic TLS [10, 53]. We can compare n_0 from C_P to $\overline{P}$ from Q^{-1} to determine how strongly the TLS are coupled to the acoustic waves by using $\gamma = 0.36$eV as was found by Duquesne and Bellessa for a-Ge from the real part of the acoustic attenuation coefficient at high frequency [10, 99]. γ has been shown to increase with increasing elastic constant and by comparing to the T_S dependence of the shear modulus and sound velocity we estimate that γ increases by $20 - 30\%$ between $T_S = 45°$C and 400°C [100]. However, for this analysis we use $\gamma = 0.36$eV since Q^{-1} changes by several orders of magnitude which cannot be accounted for by an increase in γ. We find for the 3000Å films that $\overline{P}/n_0 \sim 0.01 - 0.04$ as compared to $\overline{P}/n_0 \sim 0.05 - 0.1$ as is reported for other glasses [100]. This suggests that most of the TLS measured by specific heat are weakly coupled to acoustic waves.

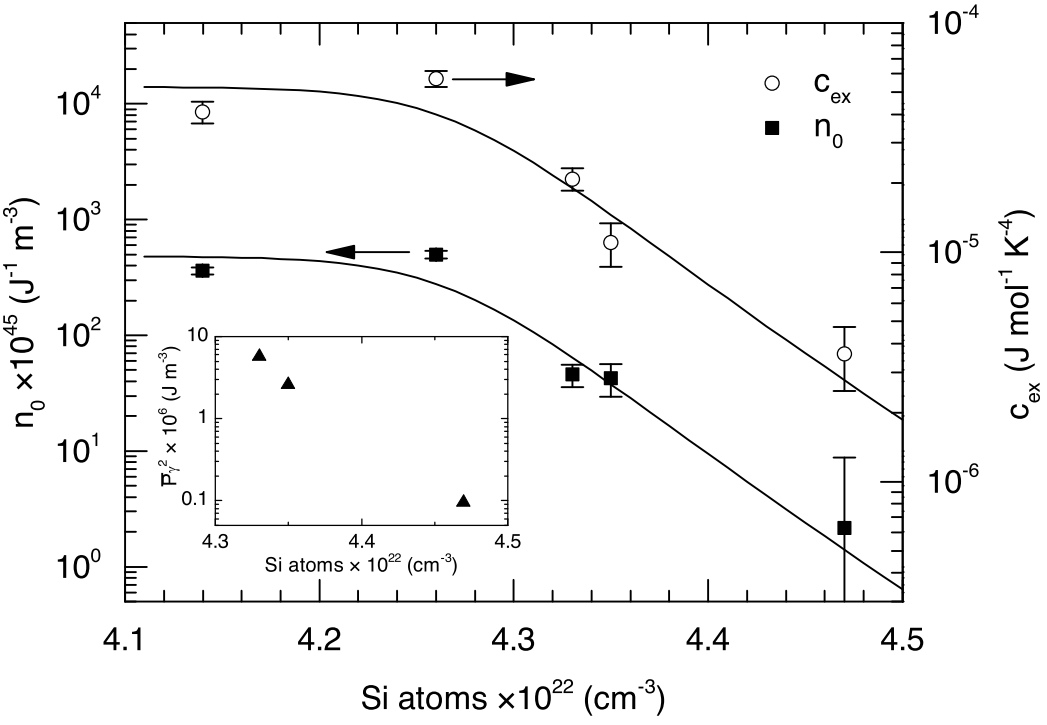

Figure 5.11: Specific heat fitting parameters n_0 (■) and $c_{ex} = c_3 - c_{Debye}$ (○) as a function of the Si number density as determined from RBS illustrating the correlation between the excess heat capacity and the silicon number density. There is no correlation when n_0 and c_{ex} are plotted against oxygen content. The lines are a guide to the eye. Inset: $\overline{P}\gamma^2$ from Q^{-1} plotted versus the silicon number density.

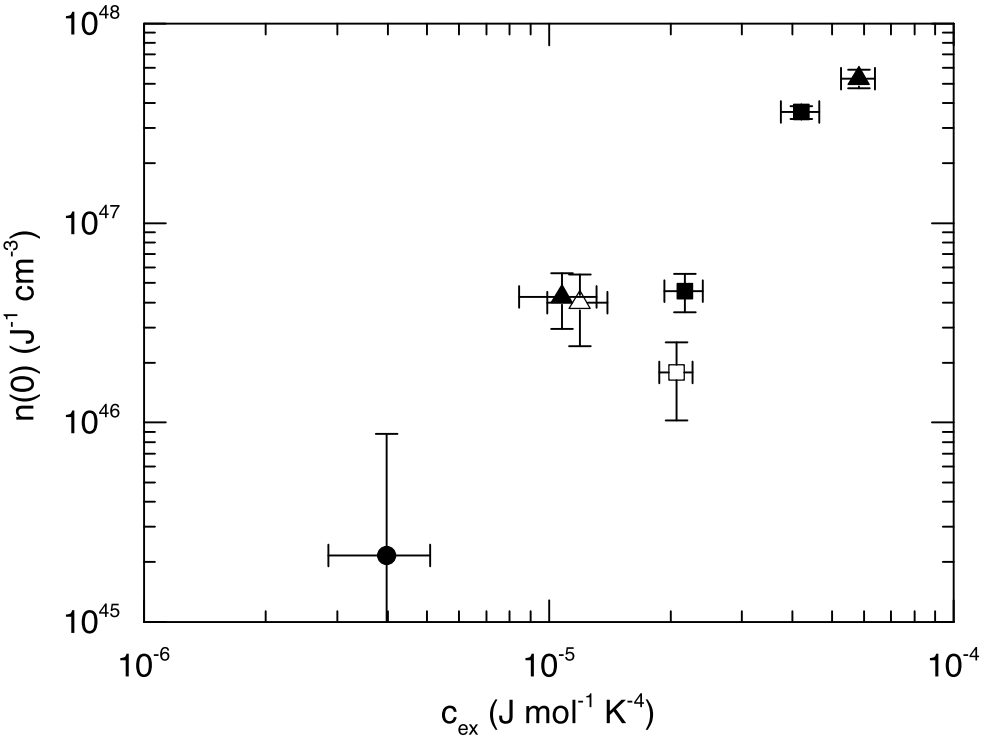

Figure 5.12: n_0 and c_{ex} determined from fits to the specific heat as described in the text. The data are identified by growth temperature 45°C (■), 200°C (▲), and 400°C (●). Open symbols are annealed samples. n_0 is the density of two-level systems (TLS) that are responsible for the linear heat capacity in amorphous materials. $c_{ex} = c_3 - c_{deb}$ is the excess T^3 specific heat presumably due to localized harmonic excitations.

Van den Berg *et al.* attributed an excess heat capacity below 1K in evaporated *a*-Si and *a*-Ge to dangling bonds [42]. The dangling bond density of the films reported here was found to be $5 - 7 \times 10^{18}\text{cm}^{-3}$ while the films from Ref. [42] had $\sim 10^{19}$ cm^{-3}. The excess heat capacity in these films does not come from dangling bonds since there is no significant difference in the dangling bond density and these measurements are above 1K and show no magnetic field dependence. Nor is it likely that the excess is due to oxygen. Figure 5.10 shows the heat capacity of the 2775Å film grown at $T_S = 45$°C after subtraction of the oxygen contribution. Bulk *a*-SiO_2 cannot account for the excess heat capacity nor can localized excitations due to oxygen atoms as neither n_0 nor c_{ex} scale with the oxygen content.

The film grown at 400°C reported here and the sample measured by Zink *et al.* grown at 45°C have specific heats that are comparable to the Debye specific heat. The density and composition from RBS shows that the film from Ref. [9] and the films grown at $T_S = 400$°C have 90% of the bulk number density and little oxygen in the film. Graebner *et*

al. found that the thermal conductivity of low density films of *a*-Ge had increased scattering from TLS and columnar voids. The increase in the specific heat found here and the decrease in the thermal conductivity reported in Ref. [49] suggests that TLS form in the low density regions and are not intrinsic to the amorphous tetrahedral network, as originally suggested by Phillips [3].

The TLS model assumes groups of atoms can change configurations by tunneling through an energy barrier. The tunnel splitting of the ground state energy gives rise to the linear temperature dependence but the model does not describe a mechanism for the excess T^3 term in the specific heat. It is clear from Figs. 5.11 and 5.12 that there is a correlation between n_0 and c_{ex} and that they both scale with the silicon number density. There is no generally accepted model for c_{ex} but evidence for an acoustic origin has been detected from inelastic neutron scattering and in some simulations. Low energy modes in excess of the Debye VDOS have been seen in the inelastic neutron scattering from a sputtered *a*-Si film [101]. Low energy modes have also been seen in inelastic neutron scattering measurements of vitreous silica and were attributed to excitations of localized acoustic modes [102]. However, Kamitakahara *et al.* speculated that the excess modes in *a*-Si were not intrinsic to the amorphous network but instead due to scattering from surface modes associated with microvoids in the film. The presence of additional modes due to surfaces is consistent with the increase in specific heat that we find in low density films. Numerical calculations of the eigenmodes of *a*-Si models made by Feldman *et al.* can account for much of the structure in the VDOS but they report no evidence of excess low frequency modes [103, 104]. A set of quasi-localized states found at low frequency in the calculation were attributed to finite size artifacts and not intrinsic to the amorphous network. The lack of excess modes in the amorphous silicon network is consistent with the Debye like heat capacity in the high density *a*-Si films reported here and in Refs. [9] and [46].

Molecular dynamics simulations have shown that the vibrational spectrum for an *a*-Si network with voids has low energy vibrational modes that can be associated with the voids and strained regions in the amorphous network [105]. These modes result in peaks in the low temperature heat capacity for $T \leq 2$K that depended on the void size. The simulations did not elucidate a clear mechanism for the appearance of the low energy states but the results suggest that the low energy modes are due to a subset of void geometries. For a distribution of void sizes, as would be found in an actual thin film, it seems likely that the structure of an individual peak would be lost resulting in an overall excess heat capacity. These simulations support our interpretation of the excess heat capacity resulting from low density regions or voids and not being intrinsic to the *a*-Si network.

5.5 Conclusions

We have shown with both heat capacity and internal friction measurements that low energy excitations are present only in evaporated *a*-Si with low Si number density. The low temperature heat capacity in high density films is comparable to the Debye specific heat. This suggests that these excitations form either in voids or low density regions and are not intrinsic to the tetrahedrally bonded amorphous network as was originally suggested by Phillips in his formulation of the TLS model. The low energy excitations have the form

of both TLS and excess harmonic modes as the linear and T^3 heat capacities both increase in the low density films. We have shown that there is a correlation between the density of TLS and the excess T^3 heat capacity.

We thank J. Karel for growing the *a*-Si films; K.M. Yu for assistance with the RBS measurements; J.W. Ager III for assistance with Raman scattering; D.G. Cahill for sound velocity measurements; D. Bobela for ESR measurements; X. Liu for the internal friction measurements and helpful discussions; the students and staff of the U.C. Berkeley Microlab for help with the design and fabrication of the nanocalorimeter; and J.L. Feldman, B.L. Zink, R.A. Street, I. Siddiqi, D.W. Cooke, and E. Helgren for fruitful discussions. The measurements and analysis were supported by the NSF under Grant No. DMR-0907724 and the film growth and nanocalorimeter development was supported by the Director, Office of Science, Office of Basic Energy Sciences, Materials Sciences and Engineering Division, of the U.S. Department of Energy under Contract No. DE-AC02-05CH11231.

Chapter 6

Specific heat of hydrogenated amorphous silicon prepared by the hot-wire CVD technique

In this chapter we report specific heat measurements from 2−300K of hydrogenated amorphous silicon (a-Si:H) prepared by the hot-wire chemical vapor deposition (HWCVD) technique. The low temperature heat capacity is significantly in excess of the Debye heat capacity calculated from the sound velocity. In the as-prepared films, a broadened Schottky anomaly is observed in the low temperature specific heat which is due to hydrogen located in metastable positions in the amorphous network. Annealing irreversibly reduces the heat capacity by over an order of magnitude below 12K. The films have a density of two-level systems (TLS) that is orders of magnitude larger than what is expected based on internal friction measurements. This large TLS density is suggested to result not from a local Si–H excitation but instead from the presence of local regions of high hydrogen density in the amorphous network. Hydrogen lowers the energy barriers for structural rearrangements resulting in the formation of TLS. The specific heat decreases at all temperatures upon annealing as the H diffuses away from the clustered regions and into the amorphous network. Comparison of the heat capacity to the internal friction suggests that the addition of H decouples the TLS from the acoustics waves.

6.1 Introduction

The low temperature thermodynamic properties of amorphous materials are known to be markedly different than their crystalline counterparts [1]. In addition to the T^3 Debye heat capacity calculated from the sound velocity, there is a T^3 contribution from excess harmonic modes and a linear term that dominates at low temperature. The low energy excitations responsible for the excess linear heat capacity are described by the phenomenological two-level systems (TLS) model [3, 4]. This model assumes that there are low energy excitations in an amorphous material due to single atoms or groups of atoms that have energetically similar spatial configurations. At low temperature, thermal activation over the energy barrier separating these configurations is no longer possible but a finite probability

exists to tunnel through the barrier and this splits the ground state energy. It is excitations of the tunnel split ground state energy that leads to the linear heat capacity. These states must be uniformly distributed in energy and space to correspond to the experimental observation of a linear low temperature heat capacity [1, 3, 4]. Phillips originally proposed that TLS could occur in open structures with low coordination where there was sufficient flexibility of the amorphous network to accommodate the rearrangements [3]. He also suggested that TLS should not occur in *a*-Si due to the over-constrained nature of tetrahedral bonding.

The low temperature specific heat of a glass has been found to fit well to the form [2]

$$C = c_1 T + c_3 T^3. \tag{6.1}$$

The coefficient of the linear term $c_1 = \frac{\pi^2}{6} k_B^2 n_0$ is due to the density of TLS n_0 present [3, 4]. In most glasses, $n_0 \sim 10^{45} - 10^{46} \mathrm{J}^{-1}\ \mathrm{m}^{-3}$ [2]. The T^3 term $c_3 = c_{Debye} + c_{ex}$ where c_{Debye} is the prefactor for the Debye heat capacity determined from the sound velocity and c_{ex} is an excess heat capacity found in all glasses [37]. $c_{ex} \approx 0.1 - 1 \times 10^{-4} \mathrm{J\ mol}^{-1}\ \mathrm{K}^{-4}$ and typically within an order of magnitude of c_{Debye} [2].

Several attempts have been made to find evidence of TLS in *a*-Si:H [40, 44]. Specific heat measurements below 5K have shown an excess heat capacity with n_0 similar to bulk quenched glasses and $c_{ex} \sim c_{Debye}$. The 5mg sample from Ref. [40] was grown by glow-discharge at room temperature and had low density $\rho = 1.5 \mathrm{g/cm}^3$ with 35 at.% H. A Schottky anomaly was found below 1 K due to a high density of dangling bond defects $n_{db} = 10^{18} \mathrm{cm}^{-3}$ and after annealing at 210°C n_{db} reduced by a factor of 10 and the heat capacity was reduced by a factor of 2. The 40mg sample from Ref [44] was prepared by glow-discharge at 230°C with density $\rho = 2.00\ \mathrm{g/cm}^3$, $n_{db} = 10^{16} \mathrm{cm}^{-3}$, and 17 at. % H. No Schottky anomaly was found in this film which suggests that the dangling bonds are responsible for the anomaly. Both films had a low temperature heat release due to conversion of molecular hydrogen H_2 from the $J = 1$ ortho-state to the $J = 0$ para-state [45, 106, 107, 108]. The equilibrium concentration of ortho molecules in H_2 is temperature dependent and saturates at 75% above 150K. The ortho concentration is dependent on the cooling history of the sample and rapid cooling is required to quench the ortho state to low temperatures. Graebner *et al.* demonstrated that rapid cooling increased the heat capacity below 5K due to an increase in ortho-state hydrogen. This increase in the heat capacity slowly decreased with time as the ortho state converted to the para state. Annealing *a*-Si:H at temperatures T_A above the growth temperature T_S increases the concentration of H_2 as weak Si-H bonds are broken with the atomic H forming H_2. The annealed *a*-Si:H film measured by Graebner was shown to have increased heat capacity due to additional H_2 in the ortho-state [108]. Both of these films have a high hydrogen content and neither is considered to be of device quality.

It was shown recently with internal friction Q^{-1} that the scattering of acoustic waves from TLS in amorphous silicon is strongly dependent upon sample preparation conditions with $Q^{-1} \sim 10^{-7} - 10^{-5}$ [19, 14]. This is unlike other bulk glasses where the scattering from TLS is found to be roughly of the same magnitude ($10^{-4} - 10^{-3}$) and independent of preparation technique for a given material [1, 19]. *a*-Si:H prepared by the hot-wire chemical vapor deposition (HWCVD) technique is of particular interest because

Q^{-1}, and presumably the density of TLS, is orders of magnitude lower than any other amorphous material when grown at high T_S. Q^{-1} increases toward the glassy regime with decreasing T_S.

It is well known that the electrical and structural properties of a-Si:H are dependent upon preparation conditions but little is known about how the thermal properties change [13]. Materials that are considered device quality have low densities of dangling bond defects and few band tail states [52]. The dangling bond defects are due to unpaired neutrally charged bonds that create states in the center of the gap. These states act as recombination centers for electron hole pairs and degrade device performance. Hydrogenation during growth passivates many of these bonds resulting in $n_{db} = 10^{16}\text{cm}^{-3}$ for hydrogenated films as opposed to 10^{19}cm^{-3} for pure a-Si films. The band tail states are localized electronic states resulting from disorder and have an exponential density of states that extends into the gap. These states are responsible for hopping transport of both electrons and hydrogen [52]. The lowest energy band tail states are due to weak Si–Si bonds that are easily broken with increasing measurement/annealing temperature. These broken bonds are stabilized by H diffusing into the site and forming a strong Si–H bond and a dangling bond. The dangling bond defects resulting from breaking of weak Si–Si bonds is in thermal equilibrium above a temperature $T_E \sim 200^\circ$ for undoped a-Si:H and result in an increase in n_{db} as the temperature is increased [109, 52, 110]. Below T_E, these thermally induced defects relax slowly with a stretched exponential time dependence as H is released from the broken bond sites of varying energy and the weak Si–Si bond is reformed. It is possible to freeze in the high temperature state by rapidly quenching through T_E [52].

In this chapter we report heat capacity measurements on thin films of a-Si:H prepared by the HWCVD technique from $2 - 300$K using a membrane-based calorimeter. In the as-prepared state, a large heat capacity with a sublinear temperature dependence is found below 12K that corresponds to the high temperature side of a peak that has a maximum at or below 2K. After annealing, the heat capacity is greatly reduced, the peak is no longer observed, and the linear temperature dependence due to TLS is decreased. We suggest that the remaining TLS are associated with clustered monohydride (Si–H) resulting in underconstrained Si atoms and annealing leads to a more homogeneous distribution of Si–H which reduces n_0. There is little change in c_{ex} upon annealing suggesting that the large value of n_0 in the as-prepared films has a different origin. The low temperature heat capacity is found to be independent of the cooling rate indicating that neither thermally induced dangling bonds nor ortho-H_2 are the source of the increase over the Debye heat capacity.

6.2 Experimental Procedure

Thin films of undoped a-Si:H were grown at various growth temperatures T_S by the HWCVD technique at the National Renewable Energy Lab (NREL) [22]. The samples are identified by the NREL run number. These films have been shown to consist of singly bonded Si–H with no polysilane SiH_x ($x = 2, 3$) detected in infrared absorption [25]. H content in the film decreases with increasing T_S as the thermal energy at the surface of the film increases the reaction rate between the impinging radicals and the bonded H.

Films prepared by HWCVD with $\sim 1-6$ at.% H ($T_S = 450-350$°C) are considered device quality and have previously been shown to habe $n_{db} \sim 10^{16}\text{cm}^{-3}$ and Urbach Edge parameter $E_U \approx 50$ meV [22]. E_U, determined from optical absorption, measures the slope of the exponential band tails and is a measure of the disorder in the film.

Both $\sim$ 700Å and $\sim$ 6000Å thick *a*-Si:H films were prepared by HWCVD on a variety of substrates including MgO, high resistivity silicon, oxide coated silicon, and nitride coated silicon. Heat capacity samples were $\sim$ 700Å thick and grown on *a*-Si-N membrane-based nanocalorimeters with 50nm thick membranes [70]. Typically films are deposited onto the nanocalorimeter using a micromachined shadow mask so that the thin film sample is confined the sample area in the center of the membrane preserving the weak thermal link through the membrane border. This method is suitable for a line of sight deposition as in PVD growth but is not effective at confining the reactive species during the CVD growth process. For these samples, the *a*-Si:H films were deposited across the entire membrane surface and the sample area was defined after the growth. A 200Å *a*-AlO_x film was sputtered onto the *a*-Si:H through a deposition mask followed by thermal evaporation of a 300Å Cu film. The Cu layer ensures that the sample area is isothermal. The *a*-AlO_x layer is used as a diffusion barrier between the *a*-Si:H and Cu films. Deposition of these two layers through the shadow mask defines the 1×1 mm^2 sample area. The unprotected *a*-Si:H on the border of the membrane was then etched with SF_6 in a reactive ion etcher at 50W until the *a*-Si:H on the device border was removed, typically after 30 seconds. There was no measurable etch rate for the Cu layer; the film did not appear rough or discolored after etching.

Heat capacity measurements were performed from $2-300$K in a LHe cryostat [94]. Details of the heat capacity measurement can be found in Chapter 4 and Refs. [70, 71, 77]. All annealing measurements were performed on the same sample after the initial heat capacity measurement in the as-prepared state. Films were annealed in the vacuum cryostat using the thin-film sample heater on the nanocalorimeter which allows a very rapid annealing cycle. Samples were annealed at $T_A = 200$°C and 300°C for 10^4 seconds with the silicon frame of the device thermally anchored to the copper sample block held at either 4.2K or 300K. Only $1-2$ mW of power was needed to heat the sample on the membrane from the base temperature (4.2K or 300K) to T_A which resulted in the copper sample block rising in temperature by $\approx$ 1K at room temperature and only by $\approx$ 2K with the sample block at 4.2K. For slow cooling, the sample heater current was incremented in 0.5μA steps for a cooling rate of $\approx$ 5K/min. For fast quenching through T_E after annealing, the current to the sample heater was set to zero and the sample cooled with an exponential temperature decay. Due to the low thermal mass and fast response time of the thin film calorimeter, the cooling rate through T_E was $\approx 10^4$K/s for the fast cooled sample which is sufficient to quench thermal defects and high temperature population of ortho-H_2. Annealing was always performed first at the lower T_A. Measurements were also made in high magnetic field for the film grown at $T_S = 430$°C in the light soaked state and no significant difference was found between zero field and 8T data for that film. The results for the light soaked films will be discussed in Chapter. 7.

Film thicknesses were measured with a KLA-Tencor Alphastep IQ profilometer with an error bar of $2-5$% depending on the film thickness. The uncertainty in film

Sample	T_S °C	v_l nm ps^{-1}	n $\times 10^{22}$ cm^{-3}	n_{Si} $\times 10^{22}$ cm^{-3}	ρ g cm^{-3}	c_H at.%
T3799	500	7.75 ± 0.39	4.56 ± 0.48	4.49 ± 0.47	2.09 ± 0.22	2
T3797	470	8.05 ± 0.40	4.39 ± 0.39	4.26 ± 0.38	1.99 ± 0.18	3
T3530	430	8.10 ± 0.40	5.04 ± 0.42	4.84 ± 0.40	2.26 ± 0.21	4
T3531	370	-	5.17 ± 0.49	4.84 ± 0.45	2.26 ± 0.21	7
T3533	300	7.92 ± 0.40	4.67 ± 0.43	4.25 ± 0.39	1.99 ± 0.16	9

Table 6.1: HWCVD a-Si:H results summary for 700Å samples. Samples are identified by their NREL run number. T_S is the substrate temperature during growth. v_l is the longitudinal sound velocity measured by the picosecond ultrasonic pump-probe technique. n_{Si} is the silicon number density determined from RBS. c_H is the hydrogen content determined from growth calibration and verified by RBS. n is the total number density and ρ is the mass density which are both calculated from n_{Si} and c_H. For crystalline silicon $n_{Si} = 5.00 \times 10^{22}$ atoms/cm^3 and $\rho = 2.33$g/cm^3. The error on c_H is $\pm 1\%$ and is estimated from the relative difference in the intensity of the hydrogen peak HFS as compared to the expected differences from the growth calibration. An absolute measure of c_H was not possible due to charging of the mylar film in the HFS detector.

thickness is the dominant source of error in all measurements except at low temperatures where the sample thermometers are susceptible to noise which leads to $> 5\%$ error bars. The atomic density of the films was determined by Rutherford Backstattering; oxygen resonant scattering was used to look for oxygen but none was detected in the films. The error in the incident flux of α particles is 3×10^{16} and leads to a large error bar in the number density for the thin films. Hydrogen content c_H is calculated from the growth calibration and verified by hydrogen forward scattering (HFS). Charging of the mylar film used in detector prevented an absolute measure of c_H but the relative values are consistent with the growth calibration values. (Table 6.1) 6000Å thick samples prepared for RBS measurements were annealed in a high vacuum chamber for 10^4 seconds to check for changes in H content and density after annealing at 200°C and 300°C. There was no change in either H content or density. Longitudinal sound velocities were measured at room temperature by a picosecond ultrasonic pump-probe technique for both the thick and thin samples and the room temperature thermal conductivity was measured by time-domain thermal reflectance on the thick samples [7]. A separate 1μm thick film was grown at $T_S = 370$°C on a single crystal double paddle oscillator (DPO) for internal friction measurements [38]. No sign of H_2 bubbles were found during inspection of the films under an optical microscope for films grown on amorphous substrates and calorimeters but the films grown on MgO did have visible bubbles and were not used for any measurements.

6.3 Results

The longitudinal sound velocity v_l for the 700Å and 6000Å thick as-deposited HWCVD a-Si:H films are reported in Table 6.1 and shown in Fig. 6.1 where they are

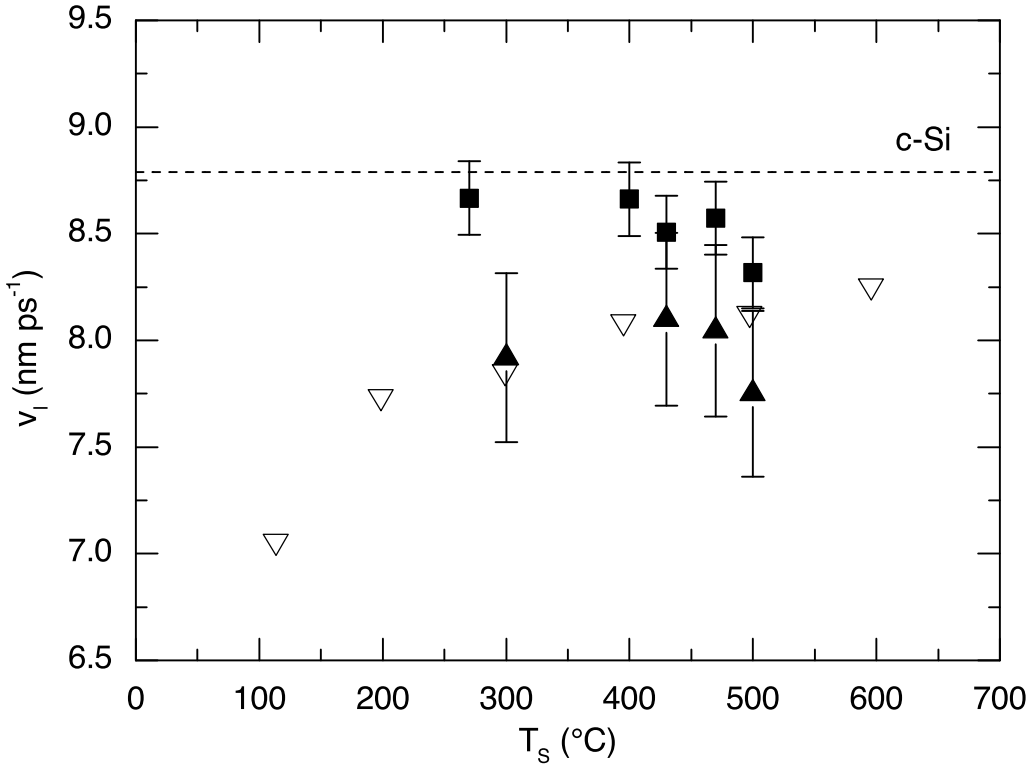

Figure 6.1: Longitudinal sound velocity measured at room temperature for several 700Å (▲) and 6000Å (■) thick HWCVD *a*-Si:H films prepared at NREL as a function of growth temperature T_S. The data from Ref. [13] for $\sim$ 2000 HWCVD films grown at UIUC (▽) are shown for comparison. The average longitudinal sound velocity of crystalline silicon is shown as a reference (- - -). The error bars are due to the uncertainty in the film thickness.

compared to the results from Ref. [13]. The error bars for v_l are from the uncertainty in film thickness. The crystalline longitudinal sound velocity is taken as the average of v_l in the [100] and [110] directions calculated from elastic constants [11]. v_l for the 700Å films agrees well with the HWCVD films reported in Ref. [13]. v_l for the 6000Å films is larger than the thinner films. The room temperature thermal conductivity is lower than the anomalously high value found in the previous films prepared at NREL that also had very low Q^{-1} [20, 26]. The thick and thin films were prepared 16 months apart and the differences are likely due to variability in the process due to conditioning of the chamber or tungsten filament.

The sound velocity v used to estimate the Debye heat capacity is calculated from $v = \frac{v_l}{v_l^c} v^c$ where v_l is the measured longitudinal sound velocity shown in Fig. 6.1 and v_l^c and v^c are the calculated longitudinal and average sound velocities respectively for crystalline silicon. The crystalline sound velocities are the average in the [100] and [110] directions calculated from elastic constants [11]. Table 6.2 lists the Debye temperatures $\theta_D = \frac{\hbar v}{k_B} \left(6\pi^2 n\right)^{\frac{1}{3}}$ where n is the total atomic density determined from RBS. (Shown in Table 6.1) v_l has been

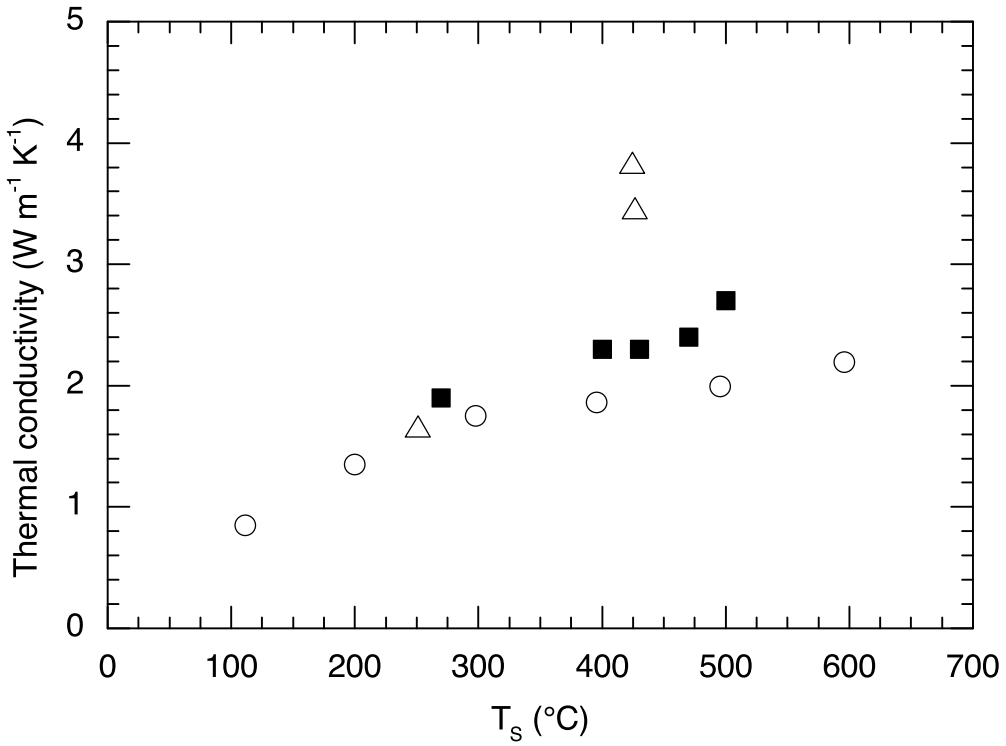

Figure 6.2: Room temperature thermal conductivity of 6000Å HWCVD *a*-Si:H films (■) prepared at NREL as a function of growth temperature T_S from this work. Shown for comparison are HWCVD films from UIUC (○) and NREL (△) from Ref. [13]. The two high thermal conductivity films are the low Q^{-1} films from Ref. [14].

assumed not to change upon annealing.

The specific heat of several a-Si:H films is shown in Fig. 6.3.a plotted as C/T^3 vs. T on a log-log scale. The specific heats of crystalline silicon [5] and vitreous silica [1] are shown for comparison along with the Debye specific heat calculated from the sound velocity and an e-beam evaporated film grown at $T_S = 400°$C. The contribution from the Boson peak is visible at ~ 35K and is negligible below ~ 12K in the e-beam a-Si film and it is assumed it is similarly small below 12K for the a-Si:H films reported here. The as-prepared a-Si:H films all have a very large non-T^3 contribution to the specific heat that is appreciable well above 1K. The heat capacity is non-monotonic in either T_S or hydrogen content. Theses films also have a sublinear temperature dependence below 7K which we suggest is the high temperature shoulder of a peak with a maximum either at or below ~ 2K since C must smoothly go to zero as $T \to 0$. This sublinear temperature dependence is clearly visible on the plot of C/T in Fig. 6.3.b where a peak at ~ 2K is possibly visible. The low temperature heat capacity of the as-prepared films was fit to a model using a Schottky anomaly and the usual glass form of Eq. 6.1

$$C(T) = c_1 T + c_3 T^3 + C_{Sch} \tag{6.2}$$

where c_1 and c_3 are the parameters described in Eq. 6.1 and C_{Sch} is the Schottky heat capacity for an ensemble of two-state systems with the same energy splitting δ,

$$C_{Sch} = n_{Sch}\ k_B\ g \left(\frac{\delta}{T}\right)^2 \frac{\exp\left(\frac{\delta}{T}\right)}{\left[1 + g \exp\left(\frac{\delta}{T}\right)\right]^2}. \tag{6.3}$$

where $g = 1$ is the ratio of the degeneracies of the states and n_{Sch} is the number of states per cm^3. Note that for a Schottky anomaly to occur in the heat capacity there must be a large density of systems with energy splitting δ whereas the TLS model assumes that each atomic TLS has a Schottky heat capacity that, when averaged over the uniform distribution of energy splittings, leads to a linear heat capacity. Figure 6.3.b shows the fits of the as-prepared films to Eq. 6.2 plotted as C/T versus T^2 to highlight the deviation from the temperature dependence of Eq. 6.1. The results for all of the a-Si:H films are summarized in Table 6.2. The density of systems responsible for the Schottky anomaly is on the order of the H content of the film.

C_{Sch} is less than 10% of the total specific heat by 7K. Fitting the as-prepared data from $2 - 12$K with Eq. 6.2 as opposed to fitting from $7 - 12$K using Eq. 6.1 results in n_0 and c_{ex} differing by $5 - 30\%$. There is considerable uncertainty in the fitting parameters for the anomaly as only part of the peak is visible. Measurements below 2K are required to better understand this feature. The value of n_0 obtained from the fit to Eq. 6.2 seems unreasonably large. A more realistic model that would provide a better estimate of n_0 is an ensemble of Schottky systems with a distribution of δ [111]. The high temperature tail on a fit of this form could account for the increase in c_1 and decrease in c_3 for the as-prepared state. Without more knowledge of the distribution of δ this type of fit is underconstrained and provides no more information than Eq. 6.2. Figure 6.5 shows n_{sch} as a function of T_S. Both the Urbach edge and dangling bond density show a similar minimum with growth temperature [24] which suggests that the Schottky states are associated with the disordered regions in the system. However, no decrease of E_u has been reported upon annealing.

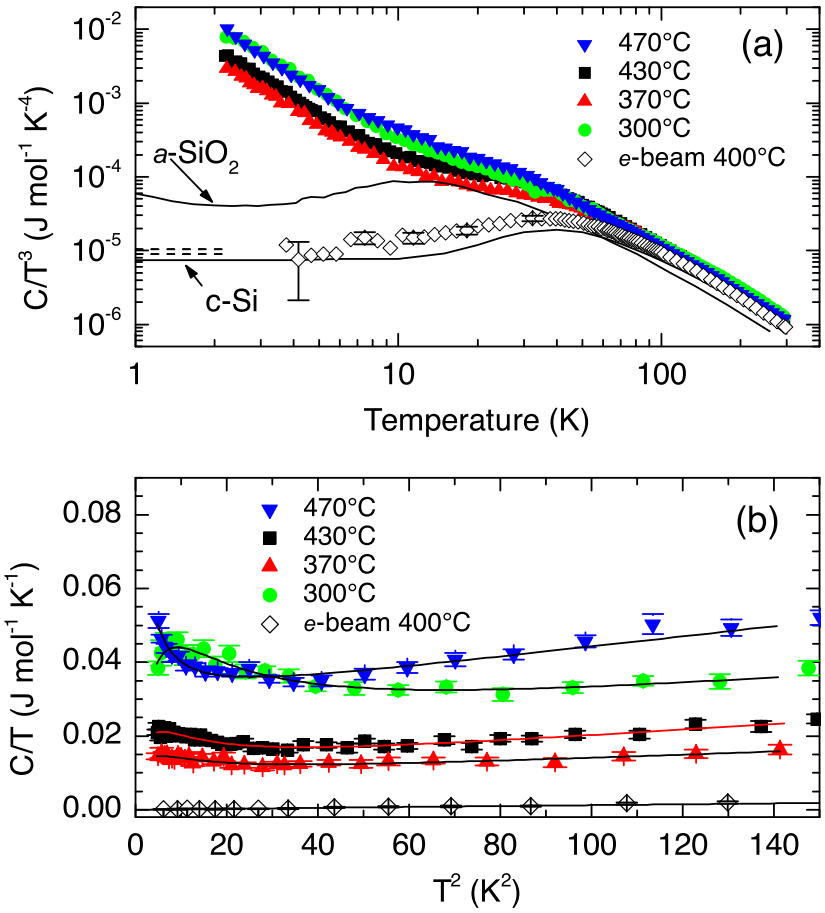

Figure 6.3: Specific heat of as-deposited HWCVD a-Si:H films for various growth temperatures. Plotted as (a) C/T^3 versus T to show the deviation from the Debye heat capacity and (b) C/T versus T^2 to show the sublinear temperature dependence. The error bars for the HWCVD samples are the same size as the data points and not shown. Increasing growth temperature corresponds to decreasing H content as shown in Table 6.1. Shown for comparison are the specific heats of c-Si [5], a-SiO_2 [1], and e-beam evaporated a-Si grown at $T_S = 400$°C ($\diamond$). The dashed lines in (a) are the maximum and minimum Debye heat capacities for the a-Si:H films shown and have been calculated from the measured longitudinal sound velocity as described in the text. The solid lines in (b) are a fit to Eq. 6.2 for the HWCVD films and Eq. 6.1 for the e-beam film.

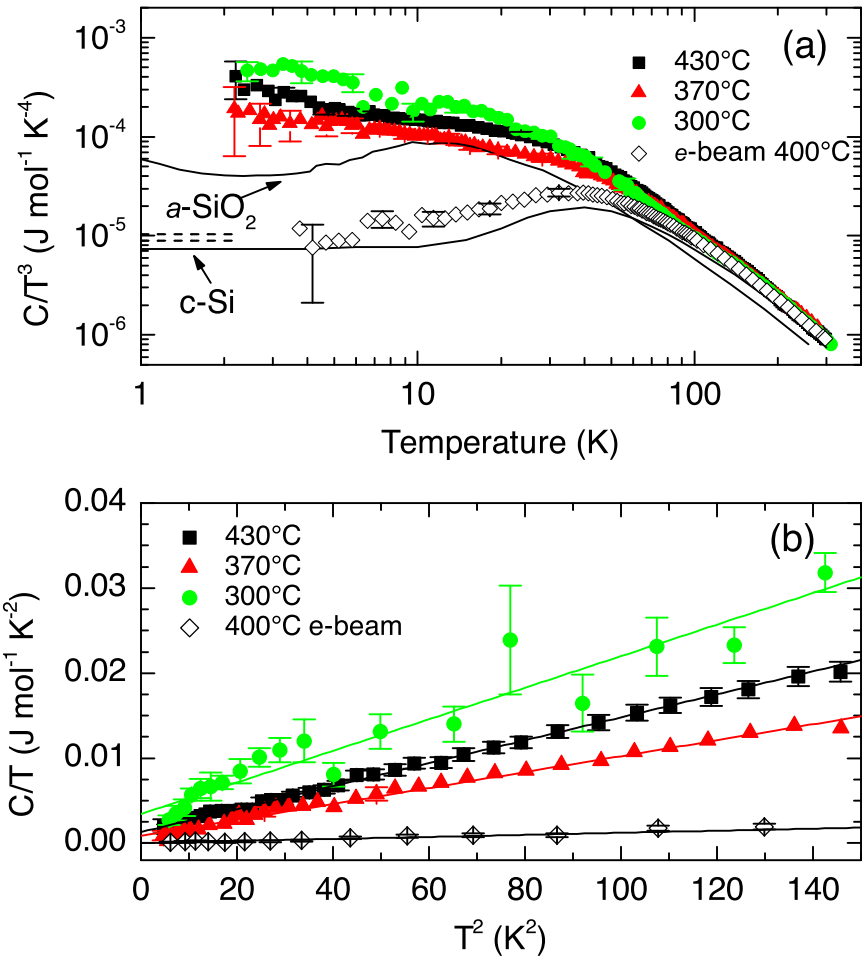

Figure 6.4: Specific heat of a-Si:H prepared at various T_S after annealing at $T_A = 200°$C. Only representative error bars are shown for clarity. Shown for comparison are the specific heats of c-Si [5], a-SiO_2 [1], and e-beam evaporated a-Si grown at $T_S = 400°$C ($\diamond$). The dashed lines are the maximum and minimum Debye heat capacities for the a-Si:H films shown and have been calculated from sound velocity as described in the text. The $T_S = 430°$C and 370°C films were fast quenched and the 300° film was slow cooled from $T_A = 200°$C. The dashed lines in (a) are the maximum and minimum Debye heat capacities for the a-Si:H films shown and have been calculated from sound velocity as described in the text. The solid lines in (b) are a fit to Eq. 6.1.

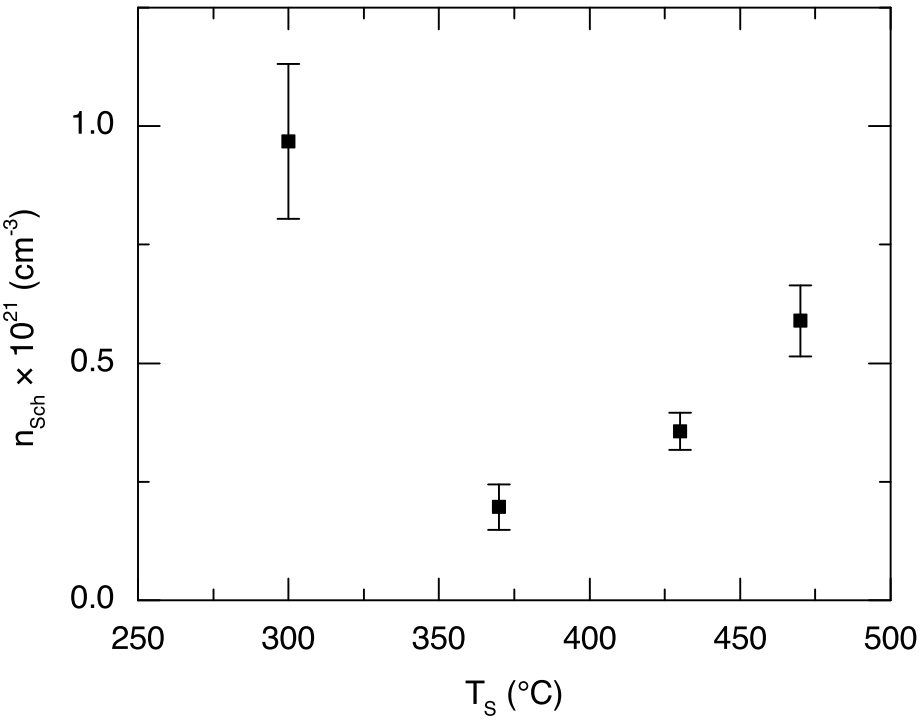

Figure 6.5: n_{Sch} versus T_S for as-prepared HWCVD films determined from the fit to Eq. 6.2.

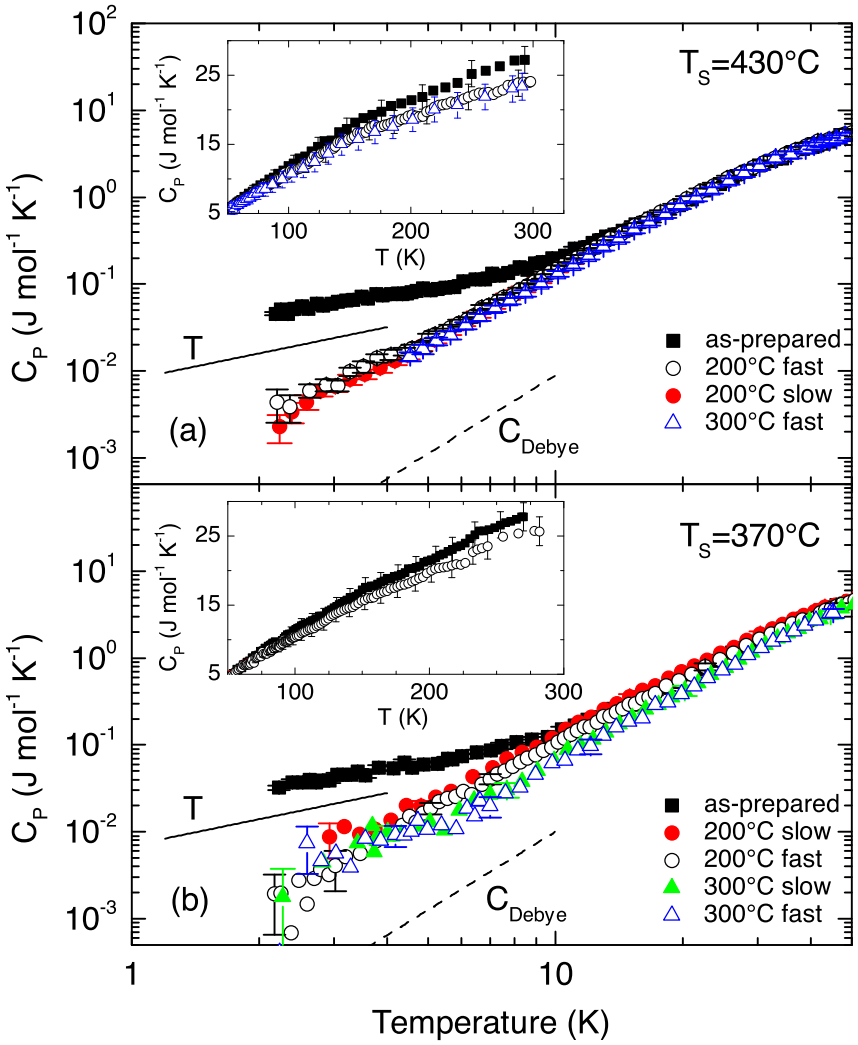

Figure 6.6: Specific heat of a HWCVD *a*-Si:H film grown at (a) $T_S = 430$°C (4 at.% H) and (b) $T_S = 370$°C (7 at.% H) in the as-prepared (■) and 200°C (●) and 300°C (▲)annealed states. The film was either fast-quenched (open symbols) or slow-cooled (closed symbols) after annealing as described in the text. The insets show the same data at high temperature on a linear scale. The Debye specific heat (- - -) is calculated from sound velocity measurements. The line labeled T is for comparison to a linear temperature dependence.

The specific heat after annealing the as-prepared films at $T_A = 200$°C is shown in Fig. 6.4. For all of the films, annealing removes the large sublinear anomaly at low temperature and greatly reduces the heat capacity. The data below 12K were fit to the TLS model of Eq. 6.1 and the results are shown in Table 6.2. Figure 6.6 shows the specific

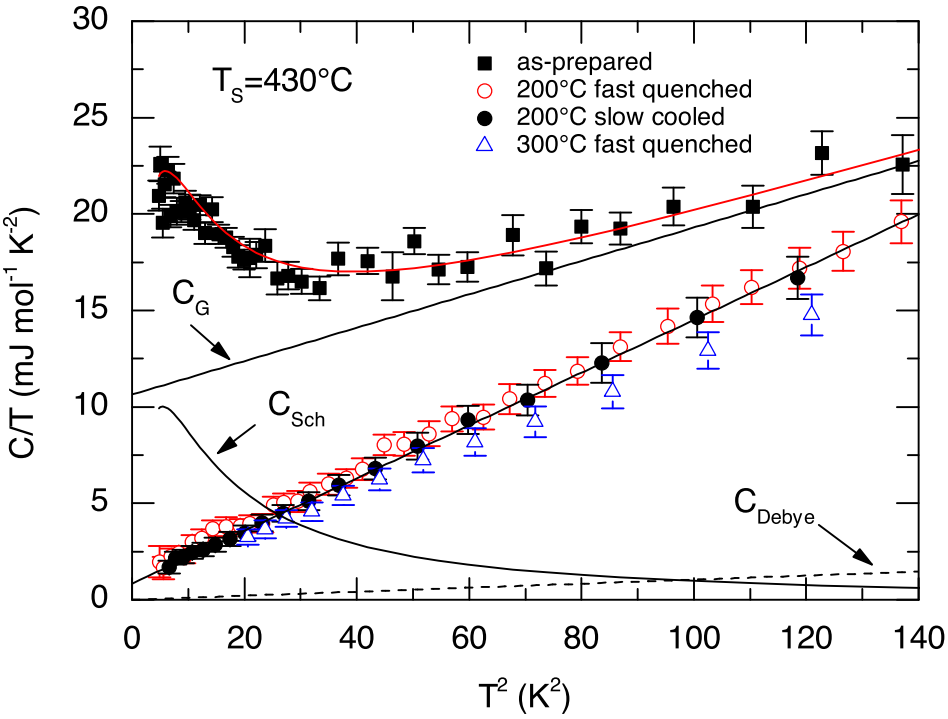

Figure 6.7: Specific heat of a HWCVD a-Si:H film grown at $T_S = 430$°C (4 at.% H) plotted as C/T versus T^2 in the unannealed (■) and 200°C (●) and 300°C (▲) annealed states. The film was either fast-quenched (open symbols) or slow-cooled (closed symbols) after annealing as described in the text. The Debye specific heat (- - -) is calculated from sound velocity measurements. All of the as-prepared films have a low temperature anomaly that has been fit to a Schottky anomaly. The as-prepared state is fit to Eq. 6.2 and is shown as the solid line through the data. The two contributions to the fit are also show separately and are labeled C_{Sch} for the Schottky term and $C_G = c_1T + c_3T^3$ for the glass term. There was no decrease in the total hydrogen content or density after annealing as measured by HFS and RBS. The annealed films are fit to Eq. 6.1 and the fit to the 200°C slow cooled state is shown.

heat of films grown at $T_S = 370$°C (7 at. % H) and $T_S = 430$°C (4 at % H) on a log-log scale for the as-prepared and annealed states. Figure 6.7 shows the low temperature specific heat of the $T_S = 430$°C (4 at % H) film plotted as C/T versus T^2.

The films were annealed and then cooled using either a slow ramp and fast quench of the sample heater as described above. After annealing at 200°C the specific heat is irreversibly reduced from the as-prepared state both at low temperature and room temperature. The sublinear term (broad Schottky anomaly) is no longer visible after annealing and the specific heat still has contributions from n_0 and c_{ex}. The low temperature data were fit to

Sample	state	label	T_S	T_A	P	T_b	θ_D	c_{Debye} $\times 10^{-5}$	n_0 $\times 10^{46}$	c_{ex} $\times 10^{-5}$	n_{Sch} $\times 10^{20}$	δ
			°C	°C	mW	K	K	J mol^{-1} K^{-4}	J^{-1} m^{-3}	J mol^{-1} K^{-4}	cm^{-3}	K
SiO_2							492	1.62	0.39	2.38		
T3798	i	a	470				570 ± 12	1.03	644±34	16±2	5.9 ± 0.8	3.5 ± 0.9
T3527	i	b	430				600 ± 3	0.90	284±25	7.8±1.0	3.7 ± 0.4	7.7 ± 0.3
	f	c		200	0.944	295		(0.90)	35±3	13±1		
	s	d		200	1.040	295		(0.90)	21±2	13±1		
	f	e		300	2.030	4.2		(0.90)	25±2	11±1		
T3528	i	f	370				592 ± 17	0.94	243±32	3.8±1.2	2.0 ± 0.5	7.6 ± 0.7
	f	g		200	0.928	295		(0.94)	24±2	8.4±0.5		
	s	h		200	0.950	295		(0.94)	53±5	9.7±0.6		
	s	j		300	1.980	295		(0.94)	35±3	4.3±0.4		
	f	k		300	2.280	4.2		(0.94)	28±4	3.9±4.0		
T3529	i	l	300				584 ± 45	0.98	473±34	9.2±3.1	9.7 ± 0.8	9.6 ± 0.3
	s	m		200	0.950	295		(0.98)	85±13	17±1		

Table 6.2: Summary of HWCVD *a*-Si:H heat capacity results. The data for *a*-SiO2 are taken from Ref. [2]. The samples are identified by the NREL run number. The sample state is listed as either the as-prepared state (i), the slow-cooled state (s), or the fast-quenched state (f). Samples are listed in the order that they were annealed. T_S is the growth temperature. T_A is the annealing temperature. P is the power applied to the sample heater during the anneal. T_b is the temperature of the sample block during the anneal. θ_D is the Debye temperature calculated from the measured longitudinal sound velocity and density for the as-prepared state as described in the text. c_{Debye} was assumed not to change upon annealing and these values are shown in parenthesis. n_0 is the density of TLS determined from the linear term in the specific heat. $c_{ex} = c_3 - c_{Debye}$ is the excess T^3 specific heat that is not due to phonons. n_{Sch} is the density of systems in the as-prepared films with energy splitting δ assuming that anomaly can be modeled as a Schottky anomaly. The as-prepared films were fit to Eq. 6.2 and the annealed films were fit to Eq. 6.1.

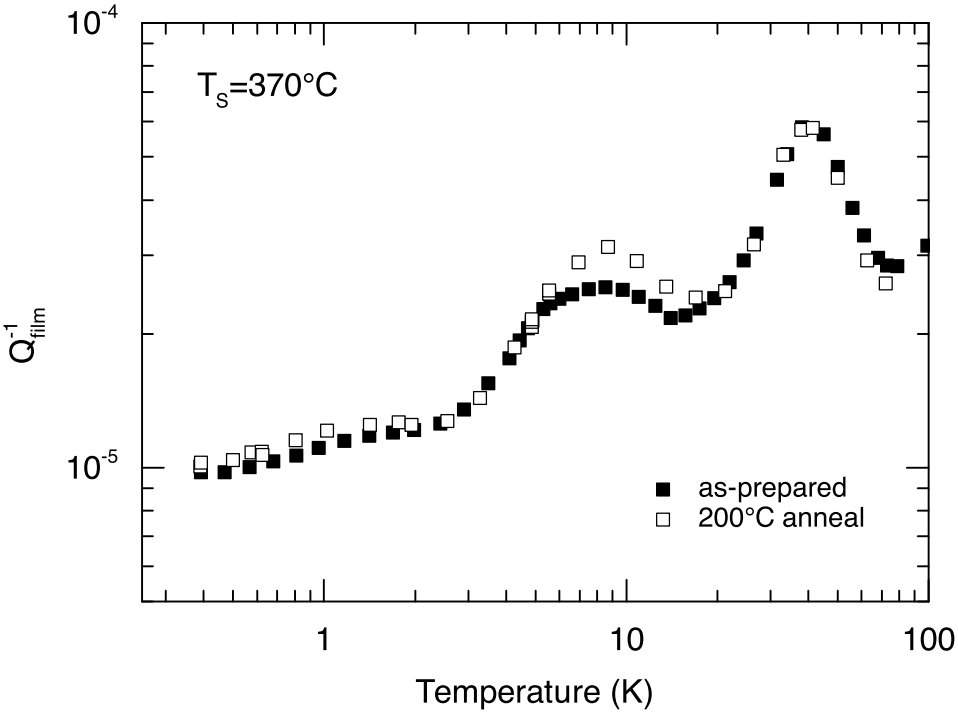

Figure 6.8: Q_{film}^{-1} of a 1μm thick HWCVD a-Si:H film grown at $T_S = 370$°C and measured with the antisymmetric mode of the double paddle oscillator at 5500Hz. The film is measured in the as-prepared and 200°C annealed states. The NREL run number for this film is T3536.

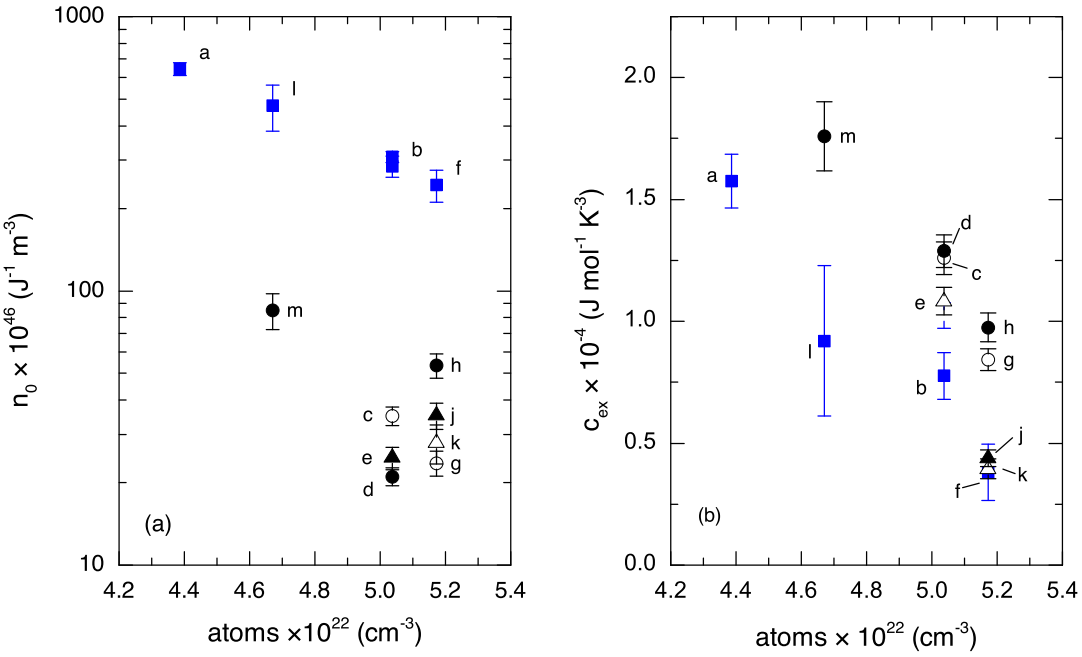

Figure 6.9: (a) n_0 and (b) c_{ex} versus total film density n as determined from RBS for HWCVD films in the as-prepared (■) fit to Eq. 6.2 and annealed states: 200°C (●) and 300°C (▲) fit to Eq. 6.1. The data point labels identify the values from Table 6.2. Open symbols correspond to fast quenching through T_E. n_0 is determined from the linear term in the specific heat and $c_{ex} = c_3 - c_{Debye}$ is the excess T^3 specific heat that is not due to phonons.

$C/T = c_1 + c_3T^2$ and the results are shown in Table 6.2. n_0 varies by up to a factor of 5 after annealing but is independent of the cooling rate and of T_A. c_{ex} also decreases and is independent of cooling rate and T_A. However, as stated above, the initial (as-deposited) values of n_0 and c_{ex} may be biased by the choice of fitting model.

Q^{-1} of a 1μm thick film grown at $T_S = 370$°C is shown in Fig. 6.8 in the as-prepared and annealed states. The peaks are due to increased damping of the acoustic waves and were previously shown to be due to H in the film since they disappear after annealing at 500°C to remove the H from the film [10]. The increase in the height of the 1K and 8K peaks after annealing indicates that H migrates to sites that are acoustically active without changing the background plateau due to damping by TLS. The magnitude of the TLS plateau is consistent with other HWCVD films prepared at the same T_S [10]. There is no indication of the H_2 triple point at $T = 13.8$K in either Q^{-1} or C which consistent with little molecular hydrogen in the film [92].

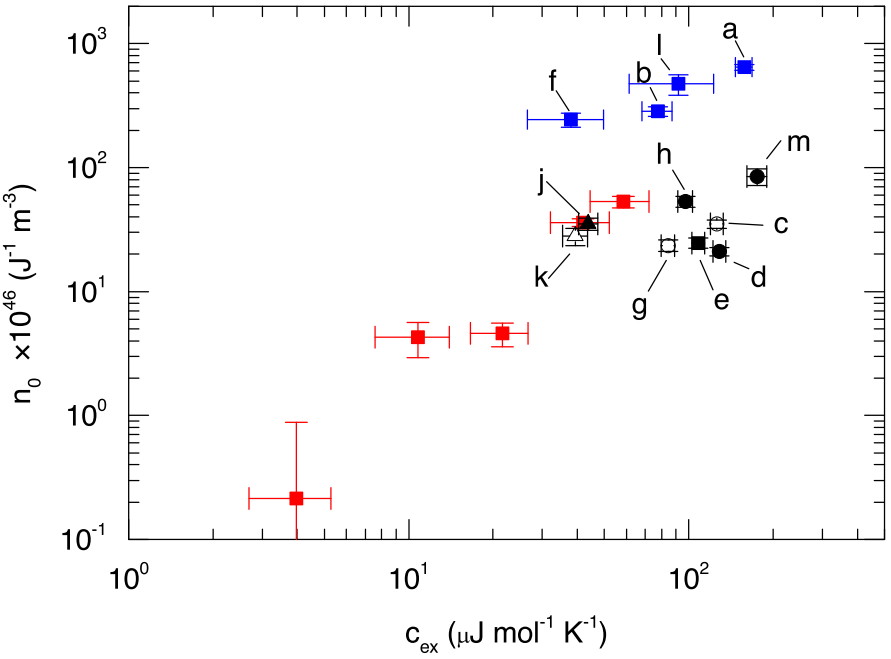

Figure 6.10: n_0 versus c_{ex} as determined from fits to the low temperature heat capacity as explained in the text. HWCVD films in the as-prepared (blue) and annealed (black) states are shown along with values for e-beam evaporated (red) films. The data are for films in the as-prepared (■) and annealed states: 200°C (●) and 300°C (▲). The data point labels identify the values from Table 6.2. Open symbols correspond to fast quenching through T_E. n_0 is determined from the linear term in the specific heat and $c_{ex} = c_3 - c_{Debye}$ is the excess T^3 specific heat that is not due to phonons.

The TLS model predicts the low temperature linear term in the heat capacity although not the magnitude of n_0 nor does it directly address the origin of c_{ex}. In the previous chapter, both n_0 and c_{ex} were shown to scale with each other and the silicon number density. From the RBS data shown in Table 6.1 we see that the Si number density n_{Si} is roughly the same for all T_S. Figure 6.9 shows n_0 and c_{ex} as a function of total number density n. The annealed films were fit to Eq. 6.1 and the as-prepared films were fit to Eq. 6.2. The correlation of n_0 and c_{ex} with n_{Si} found in a-Si and reported in Chapter 5 is not observed in the a-Si:H and the correlation with n shown in Fig. 6.9 is weak. In Fig. 6.10 we plot n_0 versus c_{ex} for the HWCVD a-Si:H films along with the a-Si films from Chapter 5. The correlation between n_0 and c_{ex} found in a-Si continues with the annealed a-Si:H films but little variation is observed between the a-Si:H films.

6.4 Discussion

In bulk quenched glasses, $n_0 \sim 10^{45}-10^{46}$ J^{-1} m^{-3} whereas $n_0 \sim 10^{47}-10^{48}$ J^{-1} m^{-3} in the annealed a-Si:H films and is larger than the evaporated a-Si films presented in Chapter 5 where $n_0 \sim 10^{45} - 10^{47}$ J m^{-3}. A similarly large value of n_0 was also found for a-Si-N and reported in Chapter 4. Lyon *et al.* found that the quasi-elastic scattering in Raman scattering due to TLS was higher in a-Si:H than in a-Si [112]. We do not attribute the low temperature heat capacity to dangling bonds as was suggested in Ref. [42] as $n_{db} \sim 10^{16}$cm^{-3} and is orders of magnitude lower in these films. In the a-Si film shown in Fig. 6.3 $n_{db} \sim 10^{18}$cm^{-3} and C is lower than in the hydrogenated films. The heat capacity due to dangling bonds has a Schottky anomaly below 1K and a strong magnetic field dependence [42, 43, 40]. Only a small increase in the heat capacity was found in an applied that was independent of the field strength. Both the insensitivity to n_{db} and lack of a strong magnetic field dependence suggest that dangling bonds do not play a role in the excess heat capacity above 2K in either a-Si or a-Si:H.

The mechanism responsible for the low temperature anomaly is currently unclear but it seems likely that it is due to H in a metastable state since it is readily removed by annealing. Graebner *et al.* found several peaks in the specific heat of a-Si:H below 5K and attributed them to the orientational-glass phase of molecular ortho hydrogen (H_2) trapped in the film [108]. The observed sublinear heat capacity is not due to the ortho state of H_2. Graebner demonstrated that the H_2 concentration, and also the heat capacity, increased upon annealing [108]. Annealing at moderate T_A ($200^\circ - 300^\circ$C which does not remove H) reduces the heat capacity so the concentration of H_2 would have to decrease if it were the source of the excess heat capacity. No hydrogen evolution from the film occurs below 400°C and T_A is too low to break the H_2 bond so the concentration of H_2 should remain constant. Liu *et al.* found a peak in Q^{-1} of HWCVD a-Si:H due to the triple point of H_2 at 13.8K in films that had macroscopic bubbles of molecular hydrogen [113]. There is no sign of the H_2 triple point in the heat capacity or macroscopic H_2 bubbles in the film. The population of the ortho-H_2 is temperature dependent and it is possible to freeze in a higher temperature population by cooling rapidly. The maximum cooling rate for the cryostat below 100K is 2.5 K/min and is sufficiently slow to allow thermal equilibrium of the ortho-state to be maintained [108]. The cooling cycle of the cryostat is reproducible and the ortho concentration should be consistent from run to run. If molecular H_2 is present in the film then rapidly quenching would maintain the high temperature ratio of 0.75 for ortho to para hydrogen and result in an increase in the heat capacity. We found that the specific heat did not increase upon fast quenching from 300°C to 4K as would be expected for an increase in the population of the ortho-state. NMR measurements have shown that $\sim 1\%$ of the hydrogen in HWCVD a-Si:H is bonded as H_2 with the remainder bonded as either isolated or clustered Si–H [114] which is consistent with our interpretation that there is little H_2 in these films.

The changes in C after annealing are suggested to be due to hydrogen diffusing to lower energy states in the amorphous network and *not* loss of H from the film. Hydrogen forward scattering measurements on 6000Å thick films annealed at 200°C and 300°C do not show any decrease in hydrogen content. The heat capacity films are capped with a-AlO_x and Cu films so H loss from the sample can only happen at the edge of the film. Since

the H content does not decrease upon annealing it is likely that the initial H in the film is in a metastable configuration resulting from the growth process. NMR measurements on annealed *a*-Si:H films grown by sputtering suggest that after annealing the distance between hydrogen atoms increases resulting in a more homogeneously distribution in the amorphous network [115]. Wu *et al.* interpreted the NMR spectra of as-prepared HWCVD *a*-Si:H to be from a highly heterogeneous distribution of hydrogen [114]. The large value of n_0 in the as-prepared films could be explained by a high local density atomic H that increases the probability of TLS formation. This would suggest that more than one H is required for the formation of a TLS. H can diffuse either as mobile H or by hopping transport through localized trap states [52]. These trap states are weak Si–Si bonds that form a dangling bond and Si–H when the H is trapped. The H continue to diffuse until they are trapped in a deep potential well [116]. The diffusion process then leads to structural relaxations that could explain the changes in n_0 and c_{ex} after annealing. The disappearance of the low temperature anomaly in the as-prepared films after annealing is likely due to a similar growth induced metastable H state that is removed as the H diffuses upon annealing.

The hydrogen atoms form states with an energy splitting of $3-8$meV that lead to the broadened Schottky anomaly. From the fit of the as-prepared heat capacity to Eq. 6.2, the number of systems that would give rise to the Schottky anomaly is a large fraction of the hydrogen in the film. The low temperature heat capacity of crystalline transition metals, such as Nb and Ta, and rare earth metals, such as Y and Sc, has a broadened Schottky anomaly due to tunneling of H [111]. These TLS are due to tunneling between potential minima created by interstitial O, N, and C dopant atoms. Peaks are also observed below 10K in Q^{-1} of these metallic systems. These peaks are much sharper than what we observe in the *a*-Si:H which is consistent with a distribution of potential energies in the amorphous material. Annealing *a*-Si:H increases the peaks in Q^{-1} and removes the broadened Schottky anomaly which indicates that the states that give rise to the increased damping in Q^{-1} are not the states causing the anomaly in C. A study of the heat capacity and internal friction of *a*-Si:D and hydrogenated crystalline silicon will provide insight into the behavior that we are seeing here.

The dangling bond defect density has been shown to be in thermal equilibrium with the amorphous network above $T_E \approx 200^\circ$C for undoped *a*-Si:H [110, 56]. As the measurement temperature is increased so does the dangling bond defect density as weak Si–Si bonds from the low energy band tail states are broken and stabilized by H [56]. The defect relaxation upon cooling below T_E obeys a stretched exponential behavior and, by fast quenching, it is possible to freeze in the higher temperature defect densities. ESR measurements have confirmed that the thermally induced defects are isolated dangling bonds with $g = 2.0055$ [52]. We performed heat capacity measurements after fast and slow cooling to test whether dangling bond defects are responsible for the excess heat capacity we see. As was stated above, there is little change in the heat capacity between the fast and slow cooling states. Thus, it is again shown that the TLS heat capacity is not due to dangling bonds but rather atomic TLS.

HWCVD *a*-Si:H was previously shown by Q^{-1} measurements to have TLS densities lower than other glasses [20, 19] whereas the specific heat of the HWCVD *a*-Si:H films reported here have TLS densities n_0 larger than typical glasses [2]. Only those TLS that

couple to the acoustic waves contribute to Q^{-1} and are a subset of the total TLS density n_0 that contributes to the heat capacity. As was found in the *a*-Si films, TLS in amorphous silicon couple very weakly to acoustic waves. In Chapter 5 we showed that only $0.01 - 0.1\%$ of the TLS in *a*-Si measured by heat capacity couple to the acoustic waves and lead to the damping measured by Q^{-1} [10]. For the *a*-Si:H films, n_0 in the annealed films is ~ 10 times larger and Q^{-1} is $10 - 100$ times smaller than other glasses suggesting that only $0.001 - 0.01\%$ of the TLS measured in C contribute to Q^{-1}. Liu *et al.* showed that by annealing at 500°C to remove the H from *a*-Si:H films leads to an increase in Q^{-1} by a factor of 10 [10]. This result combined with our heat capacity would suggest that the presence of H further decouples the TLS from the phonons. In the *a*-Si films reported in Chapter 5, both n_0 and c_{ex} decreased as the silicon number density increased. In the *a*-Si:H films reported here, the correlation of n_0 and c_{ex} with either n or n_{Si} is much weaker if present at all. Given that only certain H configurations are involved in the TLS formation it seems that the local H density in the film plays a more critical role. NMR measurements before and after annealing would provide insight into the changes in the H distribution. In Fig. 6.10 we show that the correlation between n_0 and c_{ex} that is found in both *a*-Si and is also found *a*-Si:H but changes very little for the annealed films. We believe that formation TLS in *a*-Si:H is catalyzed by the presence of H relaxes the bonding constraints on the Si atoms in addition to lowering the energy barriers between atomic configurations which allows additional TLS to be accessible. The low temperature heat capacity in the as-prepared films would be better understood by measuring C below 1K to resolve the entire anomaly.

6.5 Conclusions

We have shown that the density of TLS n_0 in *a*-Si:H determined from specific heat is $10 - 100$ times greater than what is found in the specific heat of bulk quenched glasses. The presence of H in the amorphous network increases the TLS density above pure *a*-Si. The film in the as-prepared state is metastable and the heat capacity substantially decreases upon annealing. A broadened Schottky anomaly is seen at low temperature in the as-prepared films and likely leads to an over-estimate of n_0 in the as-prepared state. Heat capacity measurements below 2K will clarify the nature of the low temperature anomaly. This anomaly is removed by annealing below the growth temperature which causes H to diffuse through the amorphous network. A corresponding increase in the peaks in Q^{-1} is also observed after annealing. Comparison of n_0 and Q^{-1} suggests that the presence of H decreases the coupling between acoustic waves and TLS.

We conclude that TLS in *a*-Si:H are atomic in origin and that the presence of H lowers the energy barrier for tunneling between atomic configurations. H diffuses through the amorphous network becoming sparsely distributed upon annealing and reduces the number of tunneling entities. This result suggest that more than one H is involved in the formation of a TLS. As was suggested by Phillips, the TLS do not occur in the full density regions that are over-constrained by tetrahedrally bonding but instead occur in regions where higher local densities of H catalyze the formation of TLS. Dangling bonds are not the source of the TLS in *a*-Si:H. We have shown that there is a correlation between n_0 and c_{ex} and suggest that a complete picture of the glassy state requires not only the tunneling

states but the harmonic excitations responsible for c_{ex}, as well.

We thank E. Iwaniczko for preparation of the *a*-Si:H films; K.M. Yu for assistance with the RBS measurements; D.G. Cahill for sound velocity and thermal conductivity measurements; X. Liu for the internal friction measurements and helpful discussions; the students and staff of the U.C. Berkeley Microlab for help with the design and fabrication of the nanocalorimeter; and J.L. Feldman, B.L. Zink, R.A. Street, J.A. Reimer, I. Siddiqi, Q. Wang, R.S. Crandall, D.W. Cooke and E. Helgren for fruitful discussions. This work was supported by the NSF under Grant No. DMR-0907724.

Chapter 7

Light induced thermodynamic metastability in amorphous silicon

In this chapter we present specific heat results from $2 - 300$K for light soaked pure and hydrogenated amorphous silicon. The heat capacity is found to increase at all temperatures after light soaking. Annealing at 200°C removes the light induced increase. The increase in heat capacity is due to metastable structural states and is related to the Staebler-Wronski effect. At low temperatures, this photo-induced effect is typical of the excess heat capacity that is characteristic of amorphous materials. At high temperatures, the photo-induced increase suggests that additional localized modes are present. The increase in heat capacity on light soaking and its vanishing on annealing is found in *a*-Si but is much weaker than in *a*-Si:H indicating that the presence of hydrogen is not required for the structural reconfigurations that lead to the Staebler-Wronski Effect, but facilitate it.

7.1 Introduction

Amorphous hydrogenated silicon (*a*-Si:H) photovoltaics undergo a loss in efficiency upon prolonged exposure to light [54]. This phenomena, known as the Staebler-Wronski Effect (SWE), is due to the light-induced creation of dangling bonds that act as recombination centers for electrons and holes. The density of dangling bonds n_{db} typically increases from 10^{16} cm^{-3} before light exposure to 10^{17} cm^{-3} afterward and can be reversibly removed by annealing at 150°C [54, 55]. The SWE limits the usefulness of *a*-Si:H for photovoltaic applications but *a*-Si:H remains an attractive system because it supports both *n*-type and *p*-type doping and can be prepared at low cost in thin-film form. It is important then to understand the mechanism that gives rise to the SWE.

The light-induced metastability is typically discussed in terms of the creation of the dangling bonds that degrade the electrical transport properties as this has direct implications on device performance. However, there is evidence that large scale structural rearrangements are occurring involving large groups of atoms as well as the creation of dangling bonds [60]. Masson *et al.* observed a shift upon light soaking in the X-ray photoelectron spectroscopy peak of the 2p Si state by 0.1eV without any line broadening [117]. The shift of the peak without broadening or developing a shoulder suggests that all Si atoms

have under gone some structural reconfiguration. It has also been shown that the volume of a-Si:H thin films increases upon light soaking ($\Delta V/V \sim 10^{-4}$) indicating a change in the local volume that is 20 times larger than a dangling bond [55, 118, 119]. The magnitude of the low temperature plateau in internal friction Q^{-1} of a-Si:H also increases upon light soaking [61]. The plateau in Q^{-1} is associated with the damping of acoustic waves by two-level systems (TLS) that are responsible for the low temperature properties of glasses. TLS are thought to be due to single atoms or groups of atoms that have structural configurations that are close in energy and can tunnel through the energy barrier separating these configurations [3, 4]. The possibility of an increase in TLS due to light soaking is particularly interesting since the TLS is due to groups of atoms and not a single dangling bond. Q^{-1} for e-beam evaporated a-Si, where $n_{db} \sim 10^{18}\text{cm}^{-3}$, was shown to be independent of magnetic field and suggesting that the TLS in amorphous silicon are atomic and not electronic in origin [53].

The low temperature specific heat of an insulating glass has been found to fit well to the form [2]

$$C = c_1 T + c_3 T^3. \tag{7.1}$$

The coefficient of the linear term $c_1 = \frac{\pi^2}{6} k_B^2 n_0$ is due to the density of TLS n_0 [3, 4]. For most glasses $n_0 \sim 10^{45} - 10^{46}\text{J}^{-1}\text{cm}^{-3}$ [2]. The T^3 term $c_3 = c_{Debye} + c_{ex}$ where c_{Debye} is the prefactor for the Debye heat capacity determined from the sound velocity and c_{ex} is an excess heat capacity found in all glasses [37]. $c_{ex} \approx 0.1 - 1 \times 10^{-4}\text{J mol}^{-1}\text{ K}^{-4}$ and typically within an order of magnitude of c_{Debye} [2].

The specific heat of dangling bonds in amorphous silicon and germanium have previously been measured [41, 42] and they result in an excess below 1K when $n_{db} \geq 10^{18}\text{cm}^{-3}$. The dangling bond specific heat has a strong magnetic field dependence and can be suppressed in fields larger than 6T [40, 44].

We present heat capacity measurements for as-prepared, light-soaked, and annealed thin films of a-Si prepared by e-beam evaporation and a-Si:H prepared by hot-wire chemical vapor deposition (HWCVD). In all films, the heat capacity increases upon light soaking and is removed by annealing at $T_A = 200°\text{C}$. The increase in the TLS density in pure a-Si indicates that hydrogen is not required for the formation of light induced metastable states. However, the density of light-induced TLS is larger in a-Si:H films indicating that H plays an important role in the light induced instability. Rapid quenching a-Si:H to create thermally induced dangling bonds does not result in an increase in the heat capacity. While the light induced and thermally induced dangling bonds are electrically identical and have approximately the same density (10^{17}cm^{-3}), they must therefore result from a different structural mechanism.

7.2 Experimental Procedure

Thin films of a-Si and a-Si:H were prepared on thin film, membrane-based nanocalorimeters by thermal evaporation and hot-wire chemical vapor deposition (HWCVD), respectively. Heat capacity measurements were made from $2 - 300\text{K}$. Details of the growth conditions are described in Chapter 3 and the measurement technique is described in Chapter 4. After growth of the sample on the transparent membrane, a 200Å thick a-AlO_x film

was sputter deposited onto the amorphous silicon film prior to deposition of the 300Å Cu conduction layer. The a-AlO_x film acts as a diffusion barrier between the Cu and Si films to prevent alloying. The film thicknesses were measured with a KLA-Tencor Alphastep profilometer and the densities were determined from Rutherford backscattering (RBS). The dangling bond densities in the evaporated a-Si films were found to be $\sim 10^{19}\text{cm}^{-3}$ from electron spin resonance (ESR) measurements. The dangling bond densities for HWCVD a-Si:H are $\sim 10^{16}\text{cm}^{-3}$ and has been reported elsewhere [22]. The longitudinal sound velocity v_l was measured at room temperature using a picosecond ultrasonic pump-probe technique [7].

The amorphous silicon samples were light soaked through the top surface of the transparent membrane under a PV Measurements Inc. small area AM1.5G solar simulator for 7 days [120, 61]. (See Figure. 4.1) The transmission through the calorimeter was measured at 633nm with a HeNe laser. The 500Å a-Si-N membrane was found to be 60% transmissive and the 500Å Pt film used for the heaters and leads was 50% transmissive. The heaters and thermomters cover $\sim 20\%$ of the sample area on the membrane and partially shadow the device during light soaking. This is partially compensated by reflection from the Cu conduction layer under the silicon film. The resistance of the sample heater was monitored during the light soaking and the temperature of the film remained below 30°C. Light soaking was performed on two a-Si:H films grown at $T_S = 370$°C (7 at.% H) and 430°C (4 at.% H) and two e-beam a-Si films grown at $T_S = 45$°C and 200°C. The light soaked samples were cooled to 77K within 1 day of light soaking and then to 2K by the second day. The heat capacity data was collected as the temperature was increased with the entire measurement taking approximately 10 days. After the light soaked measurement was complete, the samples were annealed for 10^4 seconds at 200°C in the high vacuum cryostat by using the device heater on the membrane and then cooled again to 2K. The heat capacity was found to be independent of cooling rate (5K/min versus 10^4K/s) during the anneal as discussed in Chapter 6.

7.3 Results

The heat capacity of a-Si:H grown at $T_S = 430$°C (4 at.% H) and $T_S = 370$°C (7 at.% H) is shown in Fig. 7.1. The $T_S = 430$°C film was measured in the as-prepared state, light soaked at room temperature for 7 days, and then remeasured. Subsequently, the film was annealed at 200°C to remove any light induced defects and then measured again. This was followed by additional light soaking and annealing measurements. The heat capacity is found to increase upon light soaking and then decrease after annealing. Subsequent light soaking does not return the film to the as-prepared state but annealing again at 200°C returns the heat capacity to the previous annealed state. The same light soaking and annealing behavior was found in the 370°C (7 at.% H) a-Si:H film. A decrease in the heat capacity after annealing the as-prepared state was found for all of the a-Si:H films whether or not they were light soaked. The Debye heat capacity is calculated from the measured density and sound velocity $v = \left[\frac{1}{3}v_l^{-3} + \frac{2}{3}v_t^{-3}\right]^{-1/3}$ where v_l and v_t are the longitudinal and transverse sound velocities, respectively. v_t for the a-Si was determined from elastic modulus measurements as reported in Chapter 5 and v_l was measured by a picosecond ultrasonic technique [7]. For the a-Si:H, v was assumed to be reduced from the

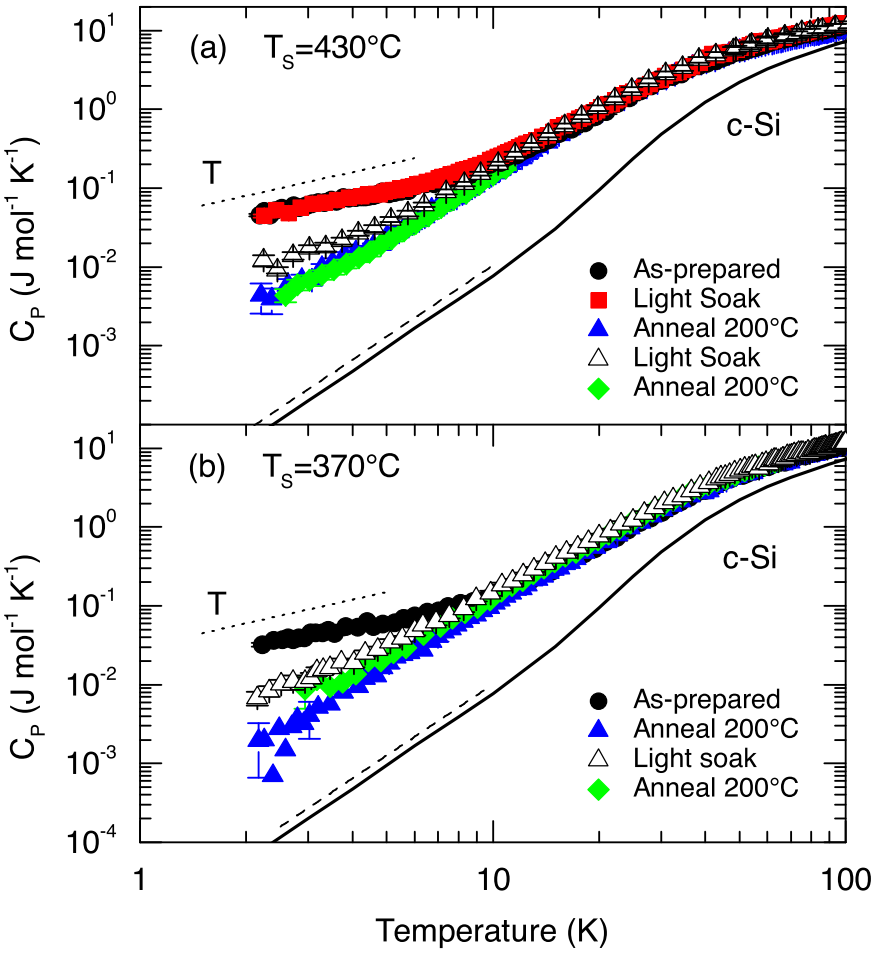

Figure 7.1: Heat capacity of a-Si:H grown by the HWCVD at (a) $T_S = 430°$C (4 at.% H) and (b) $T_S = 370°$C in the as-prepared, light soaked and annealed states. The film was either slow cooled (◆) by a controlled current ramp of the sample heater on the device or fast quenched (▲) by setting the sample heater current to zero. The photo and thermal treatments were performed in the order given in the legend. The Debye T^3 heat capacity (dashed line) is calculated from the measured longitudinal sound velocity as explained in the text and is assumed not to change upon light soaking and annealing. Crystalline silicon (heavy solid line) is shown as a reference [5]. The line labeled T is shown for comparison of the temperature dependence and is not a fit. The mole is defined as a mole of SiH_x where x is the hydrogen content in the film. The atomic density is determined from RBS.

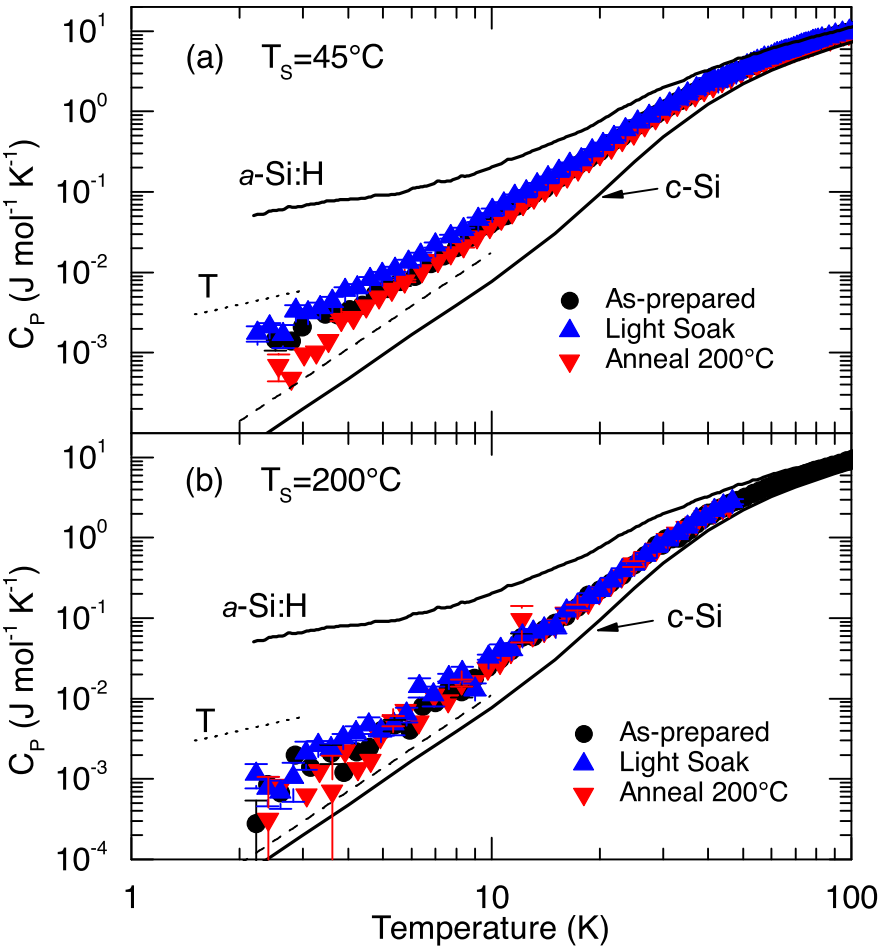

Figure 7.2: Heat capacity of an evaporated a-Si film grown at $T_S = 45$°C. The thermal and photo treatments were performed in the order listed in the legend. The film was cooled at 5K/min after annealing. The Debye heat capacity (dashed line) is calculated from the measured sound velocity. Crystalline silicon [5] and the as-prepared HWCVD film ($T_S = 430$°C) from Fig. 7.1 (heavy solid lines) are shown for reference. The line labeled T is shown for comparison of the temperature dependence and is not a fit. The mole is defined as a mole of SiO_x where x is the average concentration of oxygen in the film. The atomic density is determined from RBS.

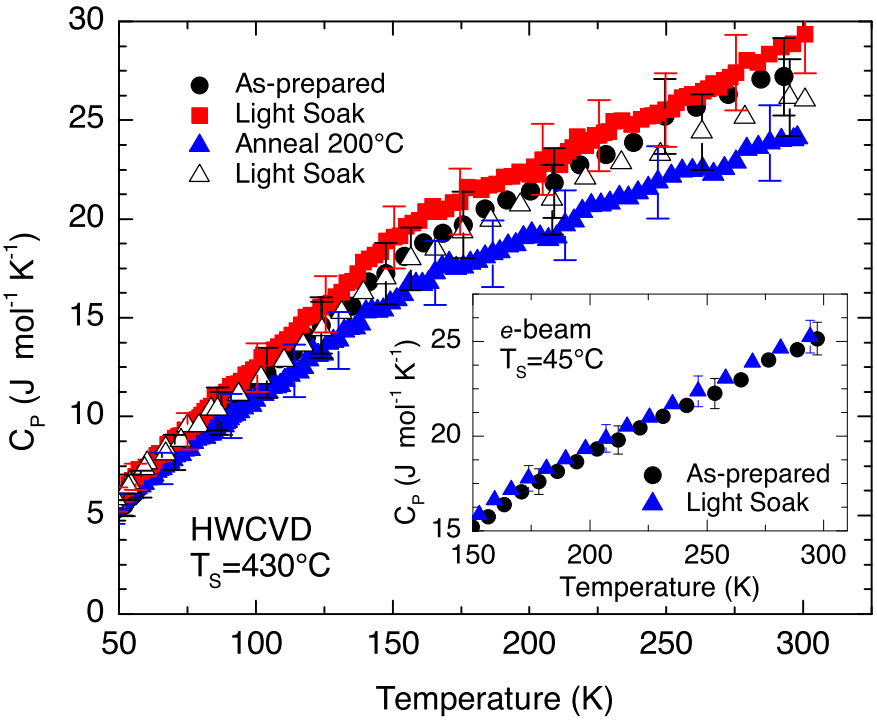

Figure 7.3: The high temperature specific heat of HWCVD a-Si:H grown at $T_S = 430°C$ and e-beam evaporated a-Si (inset) grown at $T_S = 45°C$. The order of the thermal and photo treatments is given in the legend.

crystalline value v^c by the same amount as the measured longitudinal sound velocity v_l as was seen in the evaporated a-Si films such that $v = \frac{v_l}{v_l^c} v^c$. v_l for the e-beam evaporated film grown at $T_S = 45°C$ was measured before and after light-soaking and no change was v_l was observed, suggesting no change in the Debye temperature.

Figure 7.2 shows the heat capacity of evaporated a-Si grown at $T_S = 45°C$ and 200°C in the as-prepared, light soaked, and annealed states. As with the a-Si:H films, the heat capacity of the pure a-Si film increases upon light soaking. After annealing to 200° the light induced excess heat capacity is removed and is reduced from the as-prepared value. A small increase in heat capacity upon light soaking is also seen in a film grown at 200°C; subsequent annealing at 200°C removes the light induced excess heat capacity.

For both the a-Si:H and a-Si films, the light induced increase in the heat capacity persists to room temperature. Figure 7.3 shows the room temperature heat capacity of the $T_S = 430°C$ a-Si:H and $T_S = 45°C$ a-Si films. The a-Si:H film was light soaked in the as-prepared and annealed states as described above. A small increase is also observed in the a-Si film. The excess specific heat of the light soaked state compared to the initial state ΔC is shown in Fig. 7.4. The increase in the room temperature heat capacity suggests

						Initial		Light soaked			
Sample		label	State	T_S	c_{Debye} $\times 10^{-5}$	n_0 $\times 10^{46}$	c_{ex} $\times 10^{-5}$	n_0 $\times 10^{46}$	c_{ex} $\times 10^{-5}$	Δn_0 $\times 10^{46}$	Δc_{ex} $\times 10^{-5}$
				°C	J mol^{-1} K^{-4}	J^{-1}m^{-3}	J mol^{-1}K^{-4}	J^{-1}m^{-3}	J mol^{-1}K^{-4}	J^{-1}m^{-3}	J mol^{-1}K^{-4}
T3527	HWCVD		AP	430	0.90	284 ± 33	3.7 ± 1.0	308 ± 14	10 ± 1	7.5 ± 20	3.8 ± 0.3
		1	AN		(0.90)	35 ± 3	13 ± 1	102 ± 7	14 ± 1	70 ± 5	2.1 ± 0.6
			AN		(0.90)	21 ± 2	13 ± 1				
T3528	HWCVD		AP	370	0.94	243 ± 32	3.8 ± 1.2				
		2	AN		(0.94)	24 ± 2	8.4 ± 0.5	89 ± 5	11 ± 1	66 ± 4	2.4 ± 0.3
			AN			53 ± 5	9.7 ± 0.6				
T09-061	*e*-beam	3	AP	45	1.77	4.6 ± 1.0	2.1 ± 0.1	14 ± 1	3.3 ± 0.1	8.7 ± 1.2	1.2 ± 0.1
			AN		(1.77)	1.8 ± 0.8	2.1 ± 0.1				
T10-067	*e*-beam	4	AP	200	1.11	4.3 ± 1.3	1.1 ± 0.2	7.3 ± 1.5	1.7 ± 0.2	3.0 ± 2.0	0.6 ± 0.2
			AN		(1.11)	4.0 ± 1.5	1.2 ± 0.2				

Table 7.1: Summary of low temperature heat capacity results from fits to Eq. 7.1. The unannealed *a*-Si:H films were fit to a modified form of Eq. 7.1 that includes a Schottky anomaly and is described in Chapter 6. Samples are identified by their run number, preparation technique, and the initial state before light soaking: as-prepared (AP) or annealed (AN) at 200°C. The labels identify the data points in the figures. The state of the sample is listed in the order that the light soaking and annealing occurred. T_S is the substrate temperature during growth. c_{Debye} is the Debye heat capacity calculated from the measured sound velocity as described in the text and values shown in parenthesis have been assumed not to change upon light soaking and annealing. n_0 is the density of TLS and $c_{ex} = c_3 - c_{Debye}$ is magnitude of the T^3 specific heat that is in excess of the Debye specific heat. Δn_0 and Δc_{ex} are the change in n_0 and c_{ex} between the light soaked and initial states.

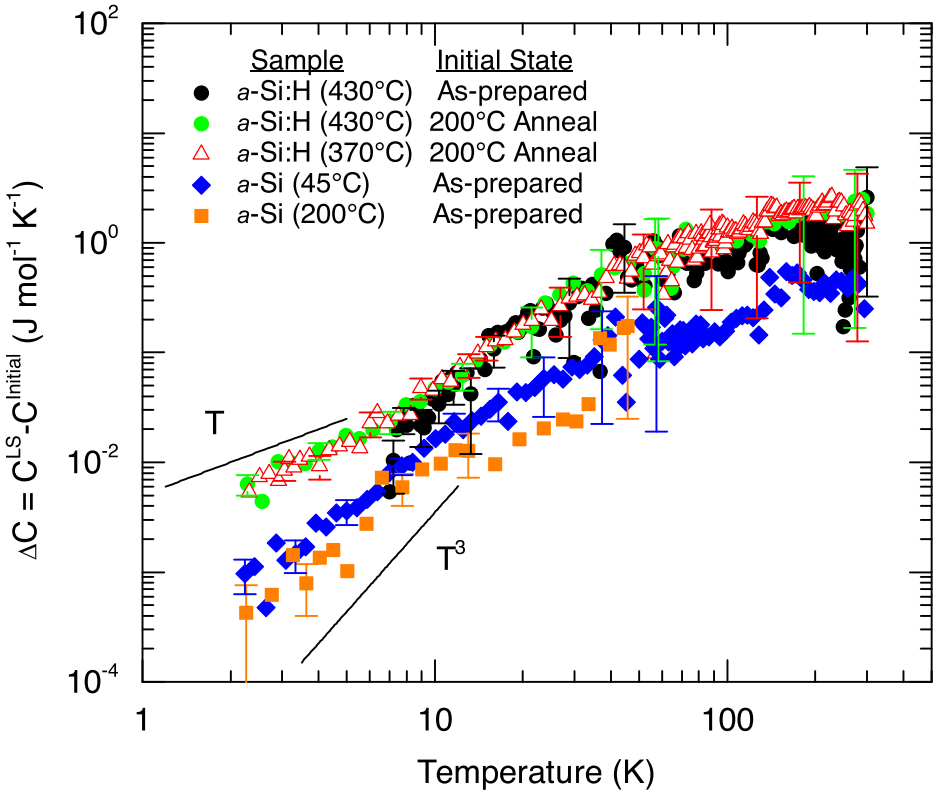

Figure 7.4: The excess specific heat $\Delta C = C^{LS} - C^{Initial}$ between the light soaked and initial states of HWCVD a-Si:H (T_S = 430°C and 370°C) and evaporated a-Si (T_S = 45°C and 200°C) upon light soaking. ΔC below 7K for the as-prepared T_S = 430°C is no dominated by error due to the large signal from the clustered H and is not shown. Samples were light soaked through the transparent membrane of the nanocalorimeter for 7 days under an AM1.5G solar simulator. The lines labeled T and T^3 are shown as a reference for the temperature dependence and are not fits.

that additional vibrational modes are present in the as-prepared and light soaked states. However, these must be localized modes as the sound velocity of the a-Si film did not change upon light soaking. At low temperatures the data fit well to the form $\Delta C = c_1 T + c_3 T^3$ where c_1 is the contribution from TLS [3, 4] and $c_3 = c_{Debye} + c_{ex}$ is due to the usual phonon heat capacity c_{deb} and an excess heat capacity c_{ex} due to localized modes. These results are summarized in Table 7.1. Both c_1 and c_3 increase upon light soaking. Below 7K, the specific heat of a-Si:H in the as-prepared state has an additional sublinear heat capacity that is believed to be a peak due to metastable H configurations and overwhelms the light induced heat capacity. Annealing causes H to diffuse through the amorphous network and away from the clusters that form during growth resulting in a more homogeneous distribution of H [115]. The linear temperature dependence of the heat capacity in amorphous materials

is due to the presence of TLS. Figure 7.5 shows Δn_0 and Δc_{ex} as a function of n_0 and c_{ex}, respectively. These data suggest that the light induced ΔC is larger in those films with a larger initial density of TLS. Figure 7.6 compares n_0 and c_{ex} for the a-Si and a-Si:H films from Chapters 5 and 6 to Δn_0 and Δc_{ex} between the light soaked and initial states. Δn_0 and Δc_{ex} show the same correlation as the n_0 and c_{ex} in the initial state suggesting that the light induced increase in TLS has the same origin as the TLS in the initial state of the films.

The magnetic field dependent specific heat is shown in Fig. 7.7 for the light soaked state of the $T_S = 45°$C a-Si and $T_S = 430°$C a-Si:H films. There is a small positive increase in the specific heat in field that is roughly temperature independent. This small increase is not due to a calibration error in the calorimeter as the heat capacity of the device has been shown to have no magnetic field dependence [121] and corrections to the calibration of the Cernox thermometer on the Cu block are small above 2K [122]. The increase does not scale with either the dangling bond density or the magnetic field. The calorimeters have been shown to have a magnetic field independent heat capacity [121] and Metcalf *et al.* did not find any increase in the Q^{-1} of evaporated a-Si in field. We do not attribute this small increase to dangling bonds due to the weak field dependence; the origin is not understood and it is almost within error bars of zero.

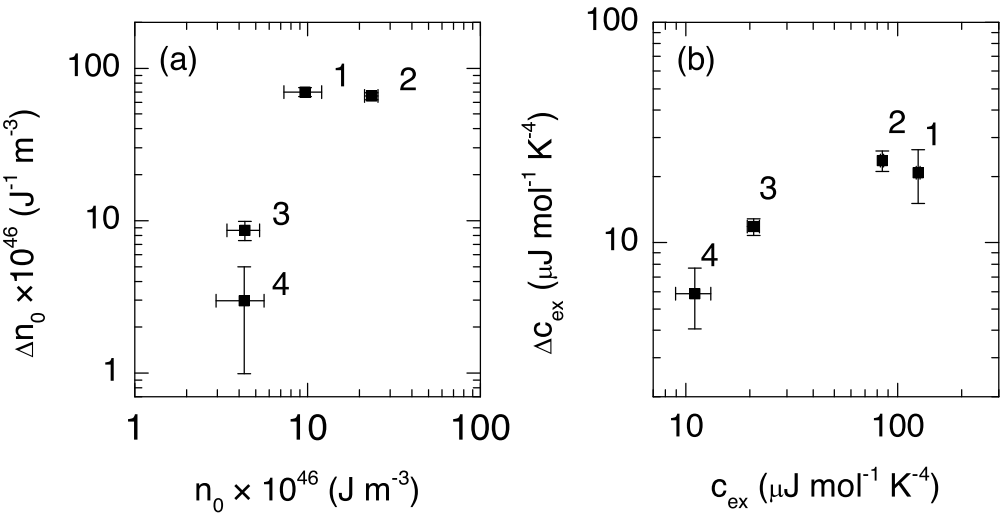

Figure 7.5: The change in (a) n_0 and (b) c_{ex} between the initial and light soaked states as a function of their initial values. The data points are identified by the labels given in Table 7.1. There is large uncertainty in n_0 and c_{ex} for the as-prepared HWCVD films due to the low temperature anomaly and the data is not shown. The annealed e-beam films were not light soaked.

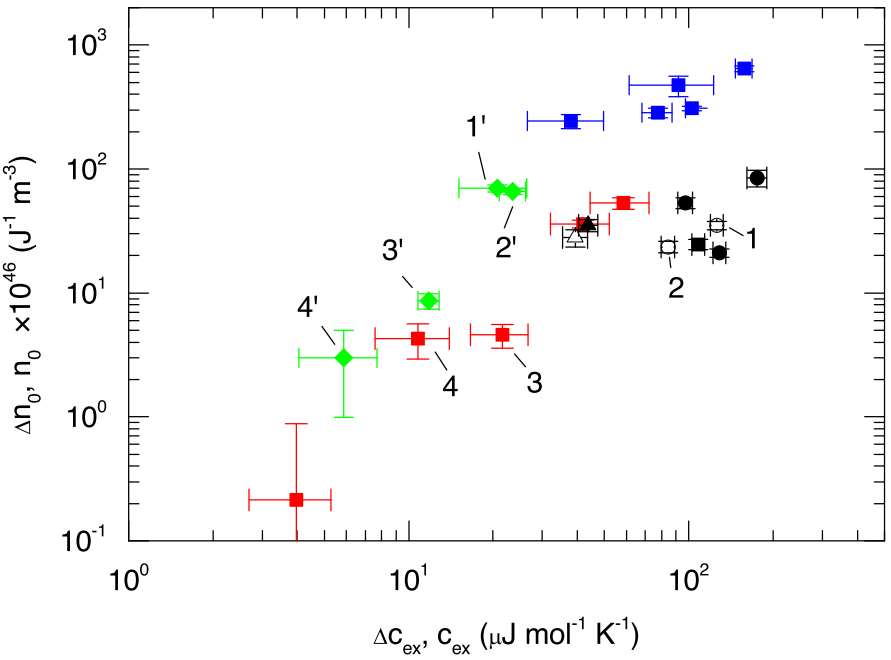

Figure 7.6: Δn_0 versus Δc_{ex} after light soaking (green) showing that light soaking increases the density of glassy excitations. The data points are identified by the labels given in Table 7.1 with the unprimed numbers identifying the initial state and the primed numbers the change upon light soaking. Shown on the same scale is n_0 versus c_{ex} for the HWCVD films in the as-prepared (blue) and annealed (black) states along with the e-beam evaporated (red) films. The data are for films in the as-prepared (■) and annealed states: T_A = 200°C (●) and 300°C (▲). Open symbols correspond to fast quenching as described in Chapter 6. n_0 is determined from the linear term in the specific heat and $c_{ex} = c_3 - c_{Debye}$ is the excess T^3 specific heat that is not due to phonons. There is large uncertainty in n_0 and c_{ex} for the as-prepared HWCVD films due to the low temperature anomaly and the data is not shown. The annealed e-beam films were not light soaked.

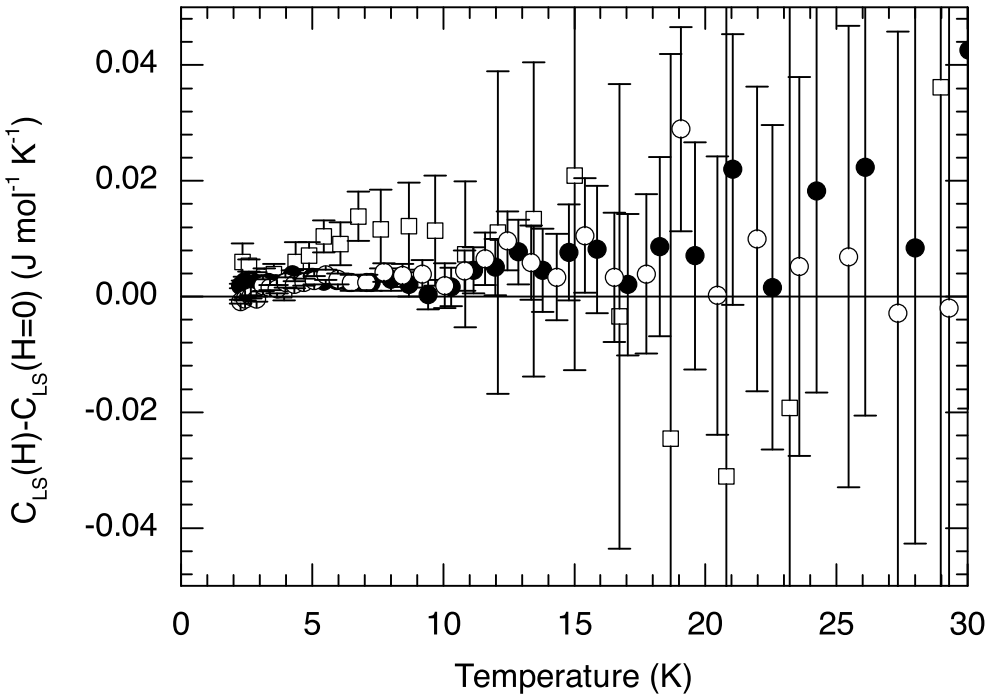

Figure 7.7: Magnetic field dependent specific heat of a-Si grown at $T_S = 45°$C in 4T (●) and 8T (○) along with a-Si:H grown at $T_S = 430°$C in 8T (□). The a-Si:H film was measured in field after the second light soaking step shown in Fig. 7.1.

7.4 Discussion

Figures 7.1 and 7.2 show that the specific heat in a-Si:H and a-Si increases upon light soaking. The increase in the low temperature specific heat is consistent with the creation of low energy excitations that lead to the excess linear and excess T^3 specific heat in glasses. The origin of the increase at high temperatures is less clear. Dangling bond generation has the same efficiency at 4.2K as it does at 300K so it is conceivable that there are structural states that are accessible higher in energy but they would not be tunneling entities as they only are found at low temperature. The temperature dependence of the high temperature excess is similar to a Debye like heat capacity suggesting that there is a decrease in the Debye temperature due to an overall softening of the amorphous network. However, a change in the Debye temperature θ_D by 200K would be required to account for the change in the T^3 specific heat at low temperature and the increase at room temperature. Such a large change in θ_D seems unlikely as this would require a change in the sound velocity of over 30%. There was no change in the longitudinal sound velocity or shear modulus of the e-beam a-Si grown at $T_S = 45°$C after light soaking so it seems unlikely that there would be a change in the sound velocity of the a-Si:H film.

In the as-prepared *a*-Si:H film, there is a growth induced metastable configuration of hydrogen in the amorphous network that increases the TLS density n_0 by lowering the energy barriers for tunneling between atomic configurations. This contribution dominates the low temperature heat capacity. An increase in the linear specific heat in the as-prepared film after light soaking cannot be resolved as it is within the error of the measurement. Annealing irreversibly reduces the heat capacity and we believe that H diffuses away from clustered regions and becomes more homogeneously distributed in the amorphous network as was discussed in Chapter 6. No loss of H from the film was detected in RBS measurements after annealing to 200°C. Fitting the low temperature specific heat of the annealed film to Eq. 7.1 shows a significant linear term. Light soaking increases both the linear and T^3 heat capacities and this increase is reversibly removed by a subsequent anneal at 200°C. It can be seen from Figure 7.4 that ΔC from light-soaking in *a*-Si:H is independent of T_S and hence also of % H.

Figure 7.2 shows that the light induced heat capacity occurs in *a*-Si as well as *a*-Si:H. Both the linear and T^3 heat capacities increase upon light soaking and this effect is reversibly removed by annealing. The light soaking effect appears much weaker in the *a*-Si films but would also require a 30% decrease in the Debye temperature to account for the change in the T^3 heat capacity. No such change is observed in the sound velocity of the $T_S = 45$°C film after light soaking. Figure 7.5 compares Δn_0 and Δc_{ex} to the values of n_0 and c_{ex} determined from the as-prepared and annealed states. It is clear the increase in the low temperature heat capacity is due to the creation of additional low energy excitations that are ubiquitous to glasses. The high temperature increase in the heat capacity could be due to the localized vibrational modes that are responsible for c_{ex}.

The light induced specific heat above 2K reported here is not due to the electronic states of the dangling bond since these leads to an excess heat capacity below 1K that has a strong magnetic field dependence up to 2K where we find only a weak, if any, increase in field [42, 40]. Light soaking then must be creating metastable structural states and these are the source of the dangling bonds. It is these structural states that are the source of the increased heat capacity. At low temperatures, n_0 and c_{ex} both increase indicating glassy TLS excitations that form upon light-soaking as the constraints on the amorphous network decrease. Generally it is thought that a weak Si–Si bond is broken upon absorption of a photon and that H migrates to the broken bond site to stabilize it resulting in the formation of a Si–H bond and a dangling bond at the weak bond site. Thus local metastable structural relaxations can occur after the formation of a dangling bond by relaxation of local bonding constraints. By measuring the deflection of a cantilever coated with *a*-Si:H after light soaking, Nomonura *et al.* demonstrated a volume increase $\Delta V/V \sim 10^{-6}$ that correlated with the dangling bond density. However, this increase required a volume 20 times the size of a single dangling bond. In *a*-Si, metastable states are associated with low density regions in the amorphous network and, in *a*-Si:H, the addition of H further lowers the energy barriers for transitions between atomic configurations. An increase in volume due to a local structural relaxation and associated dangling bond creation is consistent with TLS forming in underconstrained regions. It is not clear whether the structural relaxation leads to the dangling bond formation or vice versa. Models for the SWE typically consider mechanisms for the generation of dangling bonds but structural relaxations have not been

considered [55, 123, 124].

In addition to light soaking, dangling bonds are created in a-Si:H by heating to high temperatures and then cooling rapidly through the equilibration temperature $T_E = 200°$C the dangling bonds density can be frozen in [109, 110]. In a-Si:H, $n_{db} \sim 10^{17}$ for both light induced and thermally induced dangling bonds. It has been suggested that weak Si–Si bonds in the band tail states are thermally excited and form neutral dangling bonds that trap H to stabilize the broken bond [56]. It was shown in Chapter 6 that cooling through T_E at both 5K/min and 10^4K/s resulted in little change in the specific heat. The thermally and light induced dangling bond densities are comparable and thus the generation of dangling bonds alone is not sufficient for the creation of the structural states which lead to the increase in specific heat on light soaking [24, 110]. A structural change which also creates a dangling bond must be occurring upon light soaking.

7.5 Conclusions

In this chapter we have shown that the specific heat from $2 - 300$K of a-Si and a-Si:H increases upon light soaking and that this increase is reversibly removed by annealing at 200°C. The low temperature increase is typical of the low energy excitations that are characteristic of glasses that are due to atomic TLS and localized vibrational modes. The increase in heat capacity is the result of light induced excitation of metastable structural configurations which lead to dangling bond formation. These states anneal away at the same temperature as the SWE and a common mechanism must be responsible for both. The light induced change in the heat capacity is not directly due to dangling bond defects as they are known to result in an excess heat capacity below 1K with strong magnetic field dependence. Rather it is due to metastable structural changes that result in the formation of atomic TLS and dangling bonds. The high temperature increase in the specific heat is not due to a change in the θ_D but rather to localized excitations. It has been shown that the creation of thermally induced dangling bonds does not affect the specific heat above 2K. ΔC is largest in those films that initially have a large density of TLS but it is currently unclear if this is true for the as-prepared state where the low temperature C is dominated by H clustering. The generation of TLS upon light soaking is consistent with recent evidence that the SWE effect is the result of large scale structural reconfigurations affecting most atoms in the amorphous network and that dangling bonds are just one manifestation of this process. This is the first result that demonstrates light-induced metastablity in pure a-Si.

Chapter 8

Conclusions

Since the first reports of non-Debye like heat capacity in insulating glasses over 40 years ago, it has remained an open question as to what physical mechanism gives rise to the low energy excitations that are found in all glasses [1]. Our understanding of these low energy states remains very limited even after decades of active research. At low temperatures, there is a contribution to the heat capacity that is linear in temperature in addition to a T^3 contribution that is in excess of the Debye heat capacity calculated from the sound velocity [1, 11]. The excitations responsible for this behavior are ubiquitous to the glassy state and occur in roughly the same density ($10^{45} - 10^{46}\mathrm{J}^{-1}\ \mathrm{m}^{-3}$) in all glasses [1, 2, 19]. The two-level systems (TLS) model offers a mechanism to describe the scattering of acoustic waves seen in thermal conductivity and internal friction Q^{-1} and the linear temperature dependence to heat capacity [4, 19, 125]. The states proposed in the TLS model must be broadly distributed in energy and space. This broad distribution has made identifying a single TLS a very challenging task. However, there is evidence to suggest that the TLS description is correct. For example, it is possible to saturate the damping due to TLS in intense acoustic fields [126]. There is currently no widely accepted description of the excess T^3 heat capacity. The physical interpretation of the phenomenological TLS model is that groups of atoms have structural configurations that are nearly degenerate in energy and, at low temperature, there is a finite probability to tunnel through the energy barrier separating these configurations causing a splitting of the lowest energy levels which leads to a heat capacity which is linear in T. It was suggested by Phillips in his original paper on the TLS model that amorphous silicon would be over-constrained by its tetrahedral bonding and not support the formation of TLS [125].

We have found that TLS are indeed present in some *a*-Si and *a*-Si:H and that they can occur in higher densities than found in other glasses. However, Phillips' original intuition appears to be correct. As we reported in Chapter 5, the density of TLS in *a*-Si is highest in low density films and becomes unobservably small in *a*-Si films with full density. So the TLS are likely associated with strained or under-constrained regions of the amorphous network which occur in and around voids. In Chapter 6, we demonstrated that hydrogen plays a key role in increasing the density of TLS and suggest that H lowers the height of the energy barrier between structural configurations. The heat capacity of *a*-Si:H in the as-prepared state was shown to be metastable with a broad peak below 7K which

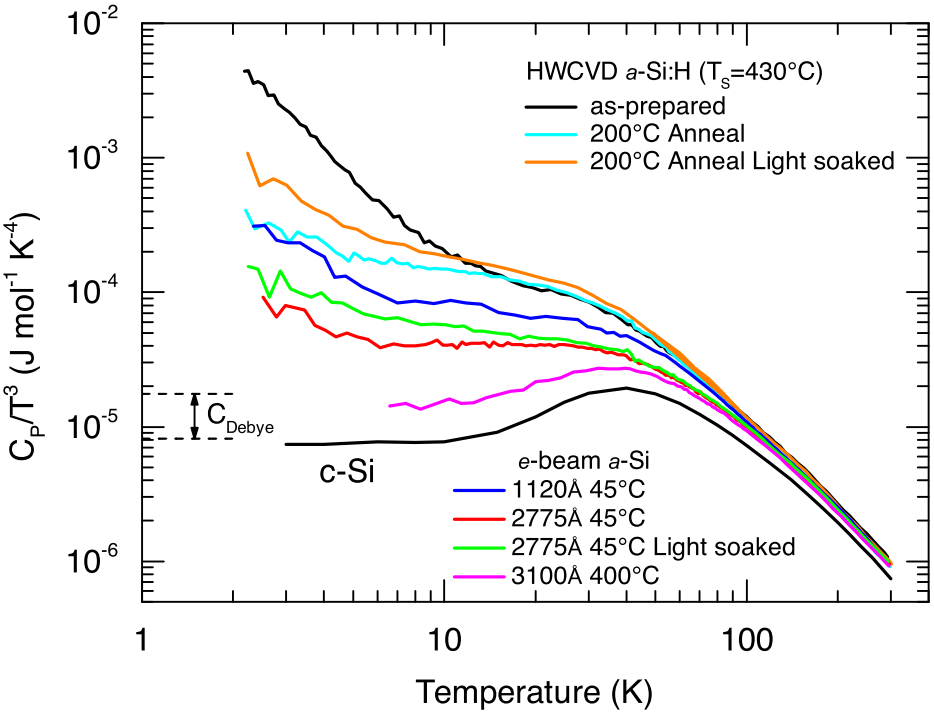

Figure 8.1: Specific heat of HWCVD a-Si:H and e-beam evaporated a-Si are plotted as C/T^3 versus T. The HWCVD sample was grown at $T_S = 430$°C and is shown in the as-prepared and the 200°C annealed states. The annealed film is shown both before and after light soaking. The evaporated films shown were grown at $T_S = 45$°C and 400°C. The films grown at $T_S = 45$°C are shown for two thicknesses: 1120Å (1.98 g/cm^3) and 2775Å (2.08 g/cm^3). The 2775Å film is shown in the as-prepared and light soaked states. The $T_S = 400$°C film (2.09 g/cm^3) is in the as-prepared state. The dashed lines are the maximum and minimum Debye heat capacities for the samples shown. The Debye specific heats are calculated from the sound velocity. The maximum Debye specific heat ($\theta_D = 480$K) is from the 2775Å $T_S = 45$°C evaporated a-Si film. The minimum Debye specific heat ($\theta_D = 620$K) is from the $T_S = 400$°C evaporated a-Si film. $\theta_D = 570$K for the HWCVD film. Crystalline silicon is shown as well ($\theta_D = 645$K) [5].

irreversibly decreases upon annealing. We suggest that this is due to regions of clustered H that form during growth and then diffuse upon annealing. In Chapter 7, an increase in the heat capacity upon light soaking was reported for both a-Si and a-Si:H. This result suggests that the Staebler-Wronski Effect is due to a structural excitation that results in the creation of TLS and that the dangling bonds that limit device performance are a consequence of the metastable structural states. Furthermore, the presence of a light induced increase in the heat capacity in pure a-Si suggests that the Staebler-Wronski Effect is intrinsic to the

amorphous silicon network. In all of the films, we find that there is a correlation between the density of TLS and the excess T^3 heat capacity.

The density of TLS n_0 from heat capacity is found to be considerably higher than what is expected based on Q^{-1} measurements. Typically for glasses, only 5–10% of the TLS measured by heat capacity contribute to the damping of acoustic waves measured by Q^{-1} [100]. We find for *a*-Si that only 1–4% of TLS measured by specific heat contribute to Q^{-1} which suggests that the coupling of TLS to acoustic waves is very weak. This coupling must be much weaker in *a*-Si:H as we find very high TLS densities ($10^{47} - 10^{48}$) from the heat capacity but these films have also been shown to have a very low Q^{-1} [20].

Amorphous silicon is thus a unique system for studying the origin of TLS in glasses because it is the only system where the TLS can be tuned over a wide range [19]. We have found that both the film density and hydrogen play a key role in not only in TLS formation. The TLS model does not address the origin of the excess T^3 specific heat, but in Figure 6.10 we have shown that the density of TLS n_0 is correlated with c_{ex} over several orders of magnitude for both *a*-Si and *a*-Si:H.

We conclude with Figure 8.1 which compares the range of low temperature specific heats found in *a*-Si and *a*-Si:H. This figure illustrates the variability of the low temperature specific heat of amorphous silicon due to excitations that we attribute to non-tetrahedrally coordinated regions in the amorphous network. The TLS model provides valuable insight into the low energy excitations in amorphous materials but fails to capture the all aspects of this phenomena. With this tunability it should be possible to further elucidate the nature of the amorphous state.

Bibliography

[1] R. C. Zeller and R. O. Pohl, "Thermal conductivity and specific heat of noncrystalline solids," *Physical Review B*, vol. 4, pp. 2029–2041, 1971.

[2] R. B. Stephens, "Low-temperature specific heat and thermal conductivity of noncrystalline dielectric solids," *Physical Review B*, vol. 8, pp. 2896–2905, 1973.

[3] W. A. Phillips, "Tunneling states in amorphous solids," *Journal of Low Temperature Physics*, vol. 7, no. 3-4, pp. 351–360, 1972.

[4] P. W. Anderson, B. I. Halperin, and C. M. Varma, "Anomalous low-temperature thermal properties of glasses and spin glasses," *Philosophical Magazine*, vol. 25, pp. 1–9, 1972.

[5] C. LLC, "Thermophysical Properties of Matter Database, Version 5.0."

[6] B. L. Zink, B. Revaz, J. J. Cherry, and F. Hellman, "Measurement of thermal conductivity of thin films with a Si-N membrane-based microcalorimeter," *Review of Scientific Instruments*, vol. 76, p. 024901, 2005.

[7] T. Lee, K. Ohmori, C. S. Shin, D. G. Cahill, I. Petrov, and J. Greene, "Elastic constants of single-crystal $TiN_x(001)(0.67 \leq x \leq 1.0)$ determined as a function of x by picosecond ultrasonic measurements," *Physical Review B*, vol. 71, p. 144106, 2005.

[8] S. Wenzel, *Applications of ultrasonic lamb waves*. PhD thesis, University of California, Berkeley, 1992.

[9] B. Zink, R. Pietri, and F. Hellman, "Thermal Conductivity and Specific Heat of Thin-Film Amorphous Silicon," *Physical Review Letters*, vol. 96, p. 055902, Feb. 2006.

[10] X. Liu and R. Pohl, "Low-energy excitations in amorphous films of silicon and germanium," *Physical Review B*, vol. 58, pp. 9067–9081, Oct. 1998.

[11] C. Kittel, *Introduction to Solid State Physics*. New York: Wiley, 7th ed., 1996.

[12] S. Lee, D. G. Cahill, and T. H. Allen, "Thermal conductivity of sputtered oxide films," *Physical Review B*, vol. 52, no. 1, pp. 253–257, 1995.

[13] H.-S. Yang, X. Liu, J. L. Feldman, R. S. Crandall, B. a. Sperling, and J. R. Abelson, "Anomalously high thermal conductivity of amorphous Si deposited by hot-wire chemical vapor deposition," *Physical Review B*, vol. 81, p. 104203, 2010.

[14] X. Liu, D. M. Photiadis, H.-D. Wu, D. B. Chrisey, R. O. Pohl, and R. S. Crandall, "Disorder in tetrahedrally bonded amorphous solids," *Philosophical Magazine Part B*, vol. 82, pp. 185–195, Jan. 2002.

[15] C. A. Angell, "Formation of glasses from liquids and biopolymers," *Science*, vol. 267, no. 5206, pp. 1924–1935, 1995.

[16] S. Sastry and C. A. Angell, "Liquid-liquid phase transition in supercooled silicon.," *Nature materials*, vol. 2, pp. 739–43, Nov. 2003.

[17] C. A. Angell, R. D. Bressel, M. Hemmati, E. J. Sare, and J. C. Tucker, "Water and its anomalies in perspective: tetrahedral liquids with and without liquid-liquid phase transitions," *Physical Chemistry Chemical Physics*, vol. 2, no. 8, pp. 1559–1566, 2000.

[18] J. Phillips, "Structural model of two-level glass states," *Physical Review B*, vol. 24, no. 4, pp. 1744–1750, 1981.

[19] R. Pohl, X. Liu, and E. Thompson, "Low-temperature thermal conductivity and acoustic attenuation in amorphous solids," *Reviews of Modern Physics*, vol. 74, pp. 991–1013, Oct. 2002.

[20] X. Liu, B. White, Jr., R. Pohl, E. Iwanizcko, K. Jones, A. H. Mahan, B. Nelson, R. Crandall, and S. Veprek, "Amorphous Solid without Low Energy Excitations," *Physical Review Letters*, vol. 78, pp. 4418–4421, June 1997.

[21] X. Liu, "Lattice vibration of amorphous and disordered crystalline silicon," *Physica B: Condensed Matter*, vol. 280, pp. 251–252, May 2000.

[22] A. H. Mahan, J. Carapella, B. P. Nelson, R. S. Crandall, and I. Balberg, "Deposition of device quality, low H content amorphous silicon," *Journal of Applied Physics*, vol. 69, no. 9, pp. 6728–6730, 1991.

[23] A. H. Mahan, Y. Chen, D. L. Williamson, and G. D. Mooney, "The structure of *a*-Si:H by small angle x-ray scattering," *Journal of Non-Crystalline Solids*, vol. 137 & 138, pp. 65–70, 1991.

[24] A. Mahan and M. Vanecek, "A reduction in the Staebler-Wronski effect observed in low H content a-Si: H films deposited by the hot wire technique," in *AIP Conference Proceedings*, vol. 234, p. 195, 1991.

[25] A. H. Mahan, L. M. Gedvilas, and J. D. Webb, "*a*-Si:H bonding in low hydrogen content amorphous silicon films as probed by infrared spectroscopy and x-ray diffraction," *Journal of Applied Physics*, vol. 87, p. 1650, 2000.

[26] X. Liu, J. Feldman, D. Cahill, R. Crandall, N. Bernstein, D. Photiadis, M. Mehl, and D. Papaconstantopoulos, "High Thermal Conductivity of a Hydrogenated Amorphous Silicon Film," *Physical Review Letters*, vol. 102, pp. 1–4, Jan. 2009.

[27] D. Polk, "Structural model for amorphous silicon and germanium," *Journal of Non-Crystalline Solids*, vol. 5, pp. 365–376, 1971.

[28] R. Zallen, *The physics of amorphous solids*. Weinheim: Wiley-VCH, 2004.

[29] E. Gopal, *Specific heats at low temperatures*. New York: Plenum Press, 1966.

[30] X. Liu and H. V. Löhneysen, "Specific-heat anomaly of amorphous solids at intermediate temperatures (1 to 30 K)," *Europhysics Letters*, vol. 33, pp. 617–622, 1996.

[31] R. B. Stephens, "Intrinsic low-temperature thermal properties of glasses," *Physical Review B*, vol. 13, pp. 852–865, 1976.

[32] V. Narayanamurti and R. Pohl, "Tunneling states of defects in solids," *Reviews of Modern Physics*, vol. 42, no. 2, pp. 201–236, 1970.

[33] R. Pohl, "Lattice vibrations of solids," *American Journal of Physics*, vol. 55, p. 240, 1987.

[34] E. Merzbacher, *Quantum Mechanics*. New York: Wiley, third ed., 1998.

[35] S. Hunklinger, "The universality of the density of states of low-energy excitations in glasses," *Philosophical Magazine Part B*, vol. 56, pp. 199–211, Aug. 1987.

[36] M. P. Zaitlin, L. M. Scherr, and A. C. Anderson, "Boundary scattering of phonons in noncrystalline materials," *Physical Review B*, vol. 12, pp. 4487–4492, 1975.

[37] W. Phillips, ed., *Amorphous Solids Low Temperature Properties*. New York: Springer-Verlang, 1981.

[38] B. White Jr and R. Pohl, "Internal Friction of Subnanometer a-SiO_2 Films," *Physical review letters*, vol. 75, no. 24, pp. 4437–4439, 1995.

[39] H. Löhneysen and H. Schink, "Specific Heat of Amorphous Germanium at Very Low Temperatures," *Physical Review Letters*, vol. 48, no. 16, pp. 1121–1124, 1982.

[40] H. Löhneysen, "Specific heat of amorphous Ge and Si at very low temperatures," *Journal of Non-Crystalline Solids*, vol. 59 & 60, p. 1087, 1983.

[41] H. J. Schink, H. V. Löhneysen, and B. Schröder, "Specific heat of neutron-irradiated crystalline and of vapor-deposited amorphous silicon," *Applied Physics A Solids and Surfaces*, vol. 36, pp. 15–18, Jan. 1985.

[42] R. van den Berg, H. Löhneysen, and H. Schink, "Calorimetric investigation of a-Si and a-Ge in high magnetic fields," *Journal of Non-Crystalline Solids*, vol. 77, pp. 1339–1342, 1985.

[43] R. Van den Berg and H. Löhneysen, "Magnetic excitations in amorphous germanium studied by high-field calorimetry," *Physical review letters*, vol. 55, no. 22, pp. 2463–2466, 1985.

[44] J. Graebner, B. Golding, L. Allen, J. Knights, and D. Biegelsen, "Thermal properties of a-Si:H at low temperatures," *Physical Review B*, vol. 29, no. 6, pp. 3744–3746, 1984.

[45] I. F. Silvera, "The solid molecular hydrogens in the condensed phase: Fundamentals and static Properties," *Reviews of Modern Physics*, vol. 52, no. 2, pp. 393–452, 1980.

[46] M. Mertig, G. Pompe, and E. Hegenbarth, "Specific heat of amorphous silicon at low temperatures," *Solid State Communications*, vol. 49, pp. 369–372, Jan. 1984.

[47] H. Löhneysen and F. Steglich, "Low-Temperature Thermal Conductivity of Amorphous Germanium," *Physical Review Letters*, vol. 39, no. 22, pp. 1420–1423, 1977.

[48] J. Graebner and L. Allen, "Tunneling systems in amorphous germanium," *Physical Review Letters*, vol. 51, no. 17, pp. 1566–1569, 1983.

[49] J. Graebner and L. Allen, "Thermal conductivity of amorphous germanium at low temperatures," *Physical Review B*, vol. 29, no. 10, pp. 5626–5633, 1984.

[50] X. Liu, P. Vu, R. Pohl, F. Schiettekatte, and S. Roorda, "Generation of Low-Energy Excitations in Silicon," *Physical Review Letters*, vol. 81, pp. 3171–3174, Oct. 1998.

[51] X. Liu, C. Spiel, R. Merithew, R. Pohl, B. Nelson, Q. Wang, and R. Crandall, "Internal friction of amorphous and nanocrystalline silicon at low temperatures," *Materials Science and Engineering: A*, vol. 442, pp. 307–313, Dec. 2006.

[52] R. Street, *Hydrogenated amorphous silicon*. Cambridge: Cambridge University Press, 1991.

[53] T. Metcalf, X. Liu, and R. Pohl, "Internal friction of amorphous silicon in a magnetic field," *Physical Review B*, vol. 61, pp. 9902–9905, Apr. 2000.

[54] D. Staebler and C. Wronski, "Reversible conductivity changes in discharge-produced amorphous Si," *Applied Physics Letters*, vol. 31, no. 4, pp. 292–294, 1977.

[55] H. Fritzsche, "Development in understanding and controlling the Staebler-Wronski effect in *a*-Si:H," *Annual Review of Materials Research*, vol. 31, pp. 47–79, 2001.

[56] R. Street and K. Winer, "Defect equilibria in undoped a-Si: H," *Physical Review B*, vol. 40, no. 9, pp. 6236–6249, 1989.

[57] A. Mahan, D. Williamson, and T. Furtak, "Observations of improved structural ordering in low H content, Hot Wire deposited *a*-Si:H," *Materials Research society symposium proceedings*, vol. 467, pp. 657–662, 1997.

[58] R. Crandall, "Deep electron traps in hydrogenated amorphous silicon," *Physical Review B*, vol. 24, p. 7457, 1981.

[59] D. Lang, J. Cohen, and J. Harbison, "Observation of a reversible field-induced doping effect in hydrogenated amorphous silicon," *Physical Review Letters*, vol. 48, p. 421, 1982.

[60] H. Fritzsche, "Photo-induced structural changes associated with the Staebler-Wronski effect in hydrogenated amorphous silicon," *Solid State Communications*, vol. 94, no. 11, pp. 953–955, 1995.

[61] X. Liu, C. Spiel, R. Pohl, E. Iwaniczko, and R. Crandall, "Low temperature internal friction study of light-induced structural instability in hydrogenated amorphous silicon," *Journal of Non-Crystalline Solids*, vol. 266-269, pp. 501–505, May 2000.

[62] A. Mahan, J. Carapella, and A. Gallagher, "Deposition of device quality low H content, amorphous silicon films," Mar. 1995.

[63] A. Mahan, B. Nelson, S. Salamon, and R. S. Crandall, "Deposition of device quality, low H content a-Si: H by the hot wire technique," *Journal of Non-Crystalline*, vol. 138, pp. 657–660, 1991.

[64] R. Nemanich, E. Buehler, Y. Legrice, R. Shroder, G. Parsons, C. Wang, G. Lucovsky, and J. Boyce, "Raman scattering from microcrystalline Si films: Considerations of composite structures with different optical absorption properties," *Materials Research society symposium proceedings*, vol. 164, pp. 265–270, 1990.

[65] R. Shuker and R. Gammon, "Raman-scattering selection-rule breaking and the density of states in amorphous materials," *Physical Review Letters*, vol. 25, no. 4, pp. 222–225, 1970.

[66] Y. K. Koh, S. L. Singer, W. Kim, J. M. O. Zide, H. Lu, D. G. Cahill, A. Majumdar, and A. C. Gossard, "Comparison of the 3ω method and time-domain thermoreflectance for measurements of the cross-plane thermal conductivity of epitaxial semiconductors," *Journal of Applied Physics*, vol. 105, no. 5, p. 054303, 2009.

[67] D. G. Cahill, W. K. Ford, K. E. Goodson, G. D. Mahan, A. Majumdar, H. J. Maris, R. Merlin, and S. R. Phillpot, "Nanoscale thermal transport," *Journal of Applied Physics*, vol. 93, no. 2, p. 793, 2003.

[68] Y. Takahashi, H. Ishii, and J. Murota, "New platinum silicide formation method using reaction between platinum and silane," *Journal of Applied Physics*, vol. 58, no. 8, pp. 3190–3194, 2009.

[69] O. Beckstein, J. E. Klepeis, G. L. W. Hart, and O. Pankratov, "First-principles elastic constants and electronic structure of α-Pt 2 Si and PtSi," *Physical Review B*, vol. 63, p. 134112, 2001.

[70] D. Queen and F. Hellman, "Thin film nanocalorimeter for heat capacity measurements of 30 nm films.," *The Review of Scientific Instruments*, vol. 80, p. 063901, June 2009.

[71] D. Denlinger, E. Abarra, K. Allen, P. Rooney, M. Messer, S. Watson, and F. Hellman, "Thin film microcalorimeter for heat capacity measurements from 1.5 to 800K," *The Review of scientific instruments*, vol. 65, p. 945, June 1994.

[72] S. L. Lai, G. Ramanath, L. H. Allen, P. Infante, and Z. Ma, "High-speed (10^4C/s) scanning microcalorimetry with monolayer sensitivity (J/m^2)," *Applied Physics Letters*, vol. 67, no. 9, p. 1229, 1995.

[73] P. Allen, J. Feldman, J. Fabian, and F. Wooten, "Diffusons, locons and propagons: Character of atomic vibrations in amorphous Si," *Philosophical Magazine Part B*, vol. 79, pp. 1715–1731, Nov. 1999.

[74] D. Kim, B. L. Zink, F. Hellman, and J. M. D. Coey, "Critical behavior of $La_{0.75}Sr_{0.25}MnO_3$," *Physical Review B*, vol. 65, p. 214424, 2002.

[75] D. Cooke, K. Michel, and F. Hellman, "Thermodynamic measurements of submilligram samples using a membrane-based 'calorimter on a chip'," *Review of Scientific Instruments*, vol. 79, p. 053902, 2008.

[76] S. Lai, J. Guo, V. Petrova, G. Ramanath, and L. Allen, "Size-Dependent Melting Properties of Small Tin Particles: Nanocalorimetric Measurements.," *Physical review letters*, vol. 77, pp. 99–102, July 1996.

[77] B. Revaz, B. Zink, and F. Hellman, "Si-N membrane-based microcalorimetry: Heat capacity and thermal conductivity of thin films," *Thermochimica Acta*, vol. 432, pp. 158–168, July 2005.

[78] B. Revaz, B. L. Zink, D. ONeil, L. Hull, and F. Hellman, "Numerical simulation of the heat transfer in amorphous silicon nitride membrane-based microcalorimeters," *Review of Scientific Instruments*, vol. 74, no. 10, p. 4389, 2003.

[79] B. Zink and F. Hellman, "Specific heat and thermal conductivity of low-stress amorphous Si-N membranes," *Solid State Communications*, vol. 129, pp. 199–204, 2004.

[80] M. Sekimoto, H. Yoshihara, and Ohkubo, "Silicon nitride single-layer x-ray mask," *Journal of Vacuum Science and Technology*, vol. 12, p. 1017, 1982.

[81] The FOM is the response of the bridge to a given ΔT. The bridge response $\Delta V \propto I_{th}\Delta R$. The choice of I_{th} is a compromise between the signal-to-noise ratio and errors from the $I_{th}^2 R$ self heating in the thermometers. (see footnote [86]) In the small ΔT method, $P = K\Delta T$ so that $I_{th} = \left(\frac{K\Delta T_{sh}}{R_{th}}\right)^{\frac{1}{2}}$. The off-null voltage of the bridge can then be written as $\Delta V = \left(\frac{K\Delta T_{sh}}{R_{th}}\right)^{\frac{1}{2}} \frac{\mathrm{d}R}{\mathrm{d}T}\Delta T$. Both ΔT and ΔT_{sh} are constants during the measurement and proportional to T. Thus, the figure of merit FOM $= \left(\frac{t_m}{t_{th}}\right)^{1/2} \frac{T^{3/2}}{\rho^{1/2}} \frac{\mathrm{d}\rho}{\mathrm{d}T}$.

[82] D. W. Hoffman, "Perspectives on stresses in magnetron-sputtered thin films," *Journal of Vacuum Science and Technology A*, vol. 12, p. 953, 1994.

[83] D. Querlioz, E. Helgren, D. R. Queen, F. Hellman, R. Islam, and D. J. Smith, "Beneficial effects of annealing on amorphous NbSi thin-film thermometers," *Applied Physics Letters*, vol. 87, no. 22, p. 221901, 2005.

[84] W. Fan and D. Zhang, "A simple approach to convex corner compensation in anisotropic KOH etching on a (100) silicon wafer," *Journal of Micromechanics and Microengineering*, vol. 16, pp. 1951–1957, Oct. 2006.

[85] R. Bachmann, F. DiSalvo, T. Geballe, R. Greene, R. Howard, C. King, H. Kirsch, K. Lee, R. Schwall, H. Thomas, and R. B. Zubeck, "Heat capacity measurements on small samples at low temperatures," *Review of Scientific Instruments*, vol. 43, no. 2, pp. 205–214, 1972.

[86] Typically, $\Delta T_{sh} = I_{th}^2 R/K$ is kept below $0.03 - 0.1\%$ of T_0 to minimize the error in the temperature calibration of the sample thermometer. Variations in ΔT_{sh} over the temperature interval ΔT lead to errors in K and τ. The error in K is proportional to $I_{th}^2 dR/dT$ and is $< 0.02\%$ for the a-Nb_xSi_{1-x} and $< 0.01\%$ for the Pt thermometer for a typical $\Delta T < 2\%T_0$. A self heating correction to the time dependant measurement can be made as well, $\tau = C/(K - \alpha P_{sh})$ where $\alpha = dlnR/dT$. For $\Delta T < 2\%T_0$, this correction is negligible: $\alpha P_{sh}/K \leq 1 \times 10^{-5}$ [85].

[87] C. H. Mastrangelo, Y.-C. Tai, and R. S. Muller, "Thermophysical properties of low-residual stress, Silicon-rich, LPCVD silicon nitride films," *Sensors and Actuators A: Physical*, vol. 23, pp. 856–860, Apr. 1990.

[88] X. Liu, T. H. Metcalf, Q. Wang, and D. M. Photiadis, "Elastic Properties of Several Silicon Nitride Films," *Materials Research society symposium proceedings*, vol. 989, pp. 0989–A22–01 – 0989–A22–06, 2007.

[89] C. Yu and J. Freeman, "Thermal conductivity and specific heat of glasses," *Physical Review B*, vol. 36, no. 14, pp. 7620–7624, 1987.

[90] D. Parshin, "Interactions of soft atomic potentials and universality of low-temperature properties of glasses," *Physical Review B*, vol. 49, no. 14, pp. 9400–9418, 1994.

[91] V. Lubchenko and P. G. Wolynes, "The origin of the boson peak and thermal conductivity plateau in low-temperature glasses.," *Proceedings of the National Academy of Sciences of the United States of America*, vol. 100, pp. 1515–8, Feb. 2003.

[92] X. Liu, E. Iwaniczko, R. Pohl, and R. Crandall, "Molecular hydrogen in Hot-wire hydrogenated amorphous silicon," *Materials Research Society Symposium Proceedings*, vol. 507, p. 595, 1998.

[93] R. Paroli and I. Butler, "A Handy Indicator of Resolution in Raman Spectroscopy," *Applied Spectroscopy*, vol. 44, no. 8, pp. 1414–1415, 1990.

[94] E. Swartz, "Efficient 4He cryostats for storage Dewars," *Review of Scientific Instruments*, vol. 57, pp. 2848–2853, 1986.

[95] R. Alben, D. Weaire, J. Smith Jr, and M. Brodsky, "Vibrational properties of amorphous Si and Ge," *Physical Review B*, vol. 11, pp. 2271–2296, 1975.

[96] D. Beeman, R. Tsu, and M. Thorpe, "Structural information from the Raman spectrum of amorphous silicon," *Physical Review B*, vol. 32, no. 2, pp. 874–878, 1985.

[97] L. Feldman and J. Mayer, *Fundamentals of surface and thin films analysis*. New York: Elsevier Science Publishing Co., 1986.

[98] G. Foti, J. C. Bean, J. M. Poate, and C. W. Magee, "Effect of structure and impurities on the epitaxial regrowth of amorphous silicon," *Applied Physics Letters*, vol. 36, no. 10, p. 840, 1980.

[99] J. Y. Duquesne and G. Bellessa, "Ultrasonic study of tunnelling defects in amorphous Se, Ge and Se-Ge compounds," *Philosophical Magazine Part B*, vol. 52, pp. 821–842, Oct. 1985.

[100] J. Berret and M. Meissner, "How universal are the low temperature acoustic properties of glasses," *Zeitschrift für Physik B*, vol. 70, pp. 65–72, 1988.

[101] W. Kamitakahara, C. Soukoulis, H. Shanks, U. Buchenau, and G. Grest, "Vibrational spectrum of amorphous silicon: Experiment and computer simulation," *Physical Review B*, vol. 36, pp. 6539–6542, 1987.

[102] U. Buchenau, N. Nücker, and A. Dianoux, "Neutron scattering study of the low-frequency vibration in vitreous silica," *Physical Review Letters*, vol. 53, p. 2316, 1984.

[103] J. Feldman, M. Kluge, P. Allen, and F. Wooten, "Thermal conductivity and localization in glasses: Numerical study of a model of amorphous silicon," *Physical Review B*, vol. 48, pp. 12589–12602, 1993.

[104] J. L. Feldman, P. B. Allen, and S. R. Bickham, "Numerical study of low-frequency vibrations in amorphous silicon," *Physical Review B*, vol. 59, no. 5, pp. 3551–3559, 1999.

[105] S. Nakhmanson and D. Drabold, "Low-temperature anomalous specific heat without tunneling modes: A simulation for a-Si with voids," *Physical Review B*, vol. 61, pp. 5376–5380, Feb. 2000.

[106] H. Löhneysen, H. Schink, and W. Beyer, "Direct experimental evidence for molecular hydrogen in amorphous Si: H," *Physical Review Letters*, vol. 52, no. 7, pp. 549–552, 1984.

[107] J. Graebner, B. Golding, and L. Allen, "Solid Hydrogen in hydrogenated amorphous silicon," *Physical Review Letters*, vol. 52, no. 7, pp. 553–556, 1984.

[108] J. Graebner, L. Allen, and B. Golding, "Solid H_2 in *a*-Si:H at low temperatures," *Physical Review B*, vol. 31, no. 2, pp. 904–912, 1985.

[109] R. Street, J. Kakalios, C. Tsai, and T. Hayes, "Thermal-equilibrium processes in amorphous silicon," *Physical Review B*, vol. 35, no. 3, pp. 1316–1333, 1987.

[110] Z. Smith, S. Aljishi, D. Slobodin, V. Chu, S. Wagner, P. Lenahan, R. Arya, and M. Bennett, "Thermal-equilibrium defect processes in hydrogenated amorphous silicon," *Physical review letters*, vol. 57, no. 19, pp. 2450–2453, 1986.

[111] P. Esquinazi, ed., *Tunneling Systems in Amorphous and Crystalline Solids*. Springer, 1998.

[112] S. Lyon and R. Nemanich, "Raman scattering from hydrogenated amorphous silicon," *Physica B+C*, vol. 117-118, pp. 871–873, Mar. 1983.

[113] X. Liu, R. O. Pohl, and R. S. Crandall, "Structural origin of bulk molecular hydrogen in hydrogenated amorphous silicon," *Materials Research Society Symposium Proceedings*, vol. 557, p. 323, 1999.

[114] Y. Wu, J. T. Stephen, D. X. Han, J. M. Rutland, R. S. Crandall, and A. H. Mahan, "New Hydrogen Distribution in a-Si:H: An NMR Study.," *Physical review letters*, vol. 77, pp. 2049–2052, Sept. 1996.

[115] J. A. Reimer, R. W. Vaughan, and K. J. C, "Proton NMR studies of annealed plasma-deposited amorphous Si:H films," *Solid State Communications*, vol. 37, pp. 161–164, 1980.

[116] H. M. Branz, "The hydrogen collision model of light-induced metastability in hydrogenated amorphous silicon," *Solid State Communications*, vol. 105, pp. 387–391, 1998.

[117] D. Masson, A. Ouhlal, and A. Yelon, "Long-range structural relaxation in the Staebler-Wronski effect," *Journal of Non-Crystalline Solids*, vol. 190, p. 151, 1995.

[118] S. Nonomura, T. Gotoh, M. Nishio, T. Sakamoto, M. Kondo, A. Matsuda, and S. Nitta, "Photoinduced expansion in hydrogenated amorphous silicon," *Materials Research Society Symposium Proceedings*, vol. 557, p. 337, 1999.

[119] E. Stratakis, E. Spanakis, H. Fritzsche, and P. Tzanetakis, "Stress and internal friction associated with light-induced structural changes of a-Si:H deposited on crystalline silicon microcantilevers," *Journal of Non-Crystalline Solids*, vol. 266-69, pp. 506–510, 2000.

[120] M. Stutzmann, W. Jackson, and C. Tsai, "Light-induced metastable defects in hydrogenated amorphous silicon: A systematic study," *Physical Review B*, vol. 32, no. 1, pp. 23–47, 1985.

[121] B. L. Zink, B. Revaz, R. Sappey, and F. Hellman, "Thin film microcalorimeter for heat capacity measurements in high magnetic fields," *Review of Scientific Instruments*, vol. 73, pp. 1841–1844, 2002.

[122] B. Brandt, D. Liu, and L. Rubin, "Low temperature thermometry in high magnetic fields. VII. Cernox sensors to 32 T," *Review of scientific instruments*, vol. 70, p. 104, 1999.

[123] R. Biswas and Y.-P. Li, "Hydrogen Flip Model for Light-Induced Changes of Amorphous Silicon," *Physical Review Letters*, vol. 82, pp. 2512–2515, Mar. 1999.

[124] L. Wagner and J. Grossman, "Microscopic Description of Light Induced Defects in Amorphous Silicon Solar Cells," *Physical Review Letters*, vol. 101, p. 265501, 2008.

[125] W. Phillips, "Phonon Scattering in Polyethylene at Low Temperatures," *Physical Review B*, vol. 3, no. 12, p. 4338, 1971.

[126] S. Hunklinger, W. Arnold, S. Stein, R. Nava, and K. Dransfeld, "Saturation of the ultrasonic absorption in vitreous silica at low temperatures," *Physics Letters A*, vol. 42, p. 253, 1972.

[127] K. Williams, K. Gupta, and M. Wasilik, "Etch rates for micromachining processing-part II," *Journal of Microelectromechanical Systems*, vol. 12, pp. 761–778, Dec. 2003.

[128] E. Abarra, K. Takano, F. Hellman, and A. Berkowitz, "Thermodynamic measurements of magnetic ordering in antiferromagnetic superlattices," *Physical review letters*, vol. 77, pp. 3451–3454, Oct. 1996.

[129] D. Cooke, F. Hellman, J. Groves, B. Clemens, S. Moyerman, and E. Fullerton, "Calorimetry of epitaxial thin films," *Review of Scientific Instruments*, vol. 82, p. 023908, 2011.

Appendix A

Surface roughness of silicon nitride membranes

In this appendix we report surface roughness measurements for various oxide and nitride films that are used in the fabrication of the nanocalorimeter. The low-pressure chemical vapor deposition (LPCVD) process results in the conformal deposition of low stress nitride. The roughness of the oxide underlayer will be a template for the growth surface for membranes grown on this oxide. The roughness of the membrane is found to be the same as the oxide underlayer except for smooth films where large pits are found. We suspect that these pits are either due to the formation of bubbles of H_2 gas that are trapped under the nitride film during growth or compositional inhomogeneities that are preferentially etched by KOH and BHF.

A.1 Sample Preparation

All samples are grown on p-type prime (100) Si wafers obtained from the U.C. Berkeley Microlab. New wafers were cleaned for ten minutes in piranha before going into the furnaces. After film growth, the wafers are coated in photoresist to protect the surface from Si particles generated during the dicing process. The photoresist was stripped in PRS-3000 and then the wafers were cleaned again in piranha.

Thermal oxide: A wet grown thermal oxide was prepared by diffusion oxidation of a crystalline silicon wafer at 1000°C in a Tystar furnace at atmospheric pressure in an O_2 gas and water vapor environment. The oxide was prepared in Tystar 4 with recipe `4WETOXA` using 100 SLM of O_2 gas and 3ml/min water vapor. This process consumes the upper surface of the silicon wafer and results in a dense oxide with a low etch rate [127].

Low temperature oxide (LTO): A low pressure chemical vapor deposited (LPCVD) oxide grown at 450°C in Tystar12 using recipe `12SULTOA`. This is the standard undoped oxide recipe using 200sccm SiH_4 and 200sccm O_2 gases. During the growth process, SiH_4 and O_2 gases react to form SiO_2 on the surface of the wafer.

Annealed LTO: This is film is deposited at the same time as the LTO sample and then transferred to Tystar4 for a 100 minute anneal at 1000°C in N_2 at atmospheric pressure. Annealing increases the density of the film.

Low stress nitride (LSN): LSN is an LPCVD film deposited at 835°C in Tystar 17 using recipe LSNSTDA. The film can be used to fabricate thin membranes if the film stress is below 200MPa. For the low stress film grown at 835°C, $SiCl_2H_2$ and NH_4 are mixed at a ratio of 4:1. The process pressure and flow rates in the tube change with the pump package that is on the furnace and current process monitoring measurements should be consulted before growth. The flow rate of the gas in the furnace is important for achieving a reproducibly low stress film with no particulates. LSN films were prepared both on blank and oxide coated silicon wafers.

Silicon nitride membranes: Membranes are released by etching the silicon wafer for $\sim$ 8 hours in KOH at 80° and then removing the oxide using a 5:1 BHF. Details of the membrane preparation are discussed in Chapter 4. The following films were measured: DQ05L3 is an 1800Å LSN film deposited on a 1.2μm LTO layer, DQ05L6 is an 1800Å LSN film deposited on a 5300Å thermal oxide under layer, and two membranes prepared on bare silicon in 2006 and 1993.

A.2 Experimental procedure

All film thicknesses were determined using optical reflectometry with the Nanometrics Nanospec in the U.C. Berkeley Microlab. The film thickness is calculated by comparing interference spectra for normal incidence light to a standard of known thickness and index of refraction. The surface roughness of the films was measured with a Seiko Nanopics 2100 atomic force microscope (AFM) in non-contact mode. Using the AFM in non-contact mode allowed measurement of both the front and back surfaces of the delicate membranes. The average R_a and RMS R_{RMS} surface roughnesses were determined by analyzing the AFM images after removing the background curvature. The curvature was removed by using the Flat function in the Nanograin analysis package. The Flat function subtracts the average of two line scans in either the x or y directions. An isotropic low pass filter was applied to the data to remove the high frequency random noise. R_a and R_{RMS} are defined as,

$$R_a = \frac{1}{S_0} \int |F(x,x) - Z_0| \, dxdy, \tag{A.1}$$

and,

$$R_{RMS}^2 = \frac{1}{S_0} \int [F(x,x) - Z_0]^2 \, dxdy, \tag{A.2}$$

where, $F(x,y)$ is the height,S_0 is the area of the scan, Z_0 is the average height in the scan area. The standard deviation σ of the surface roughness is defined as,

$$\sigma = \sqrt{R_{RMS}^2 - R_a^2}. \tag{A.3}$$

A.3 Results and Discussion

Table A.1 lists the results of the surface roughness analysis of the oxide and nitride films and the front and back surfaces of the nitride membranes. The thermal oxide is considerably smoother than the LTO as is to be expected from the growth mechanism.

Sample	thickness Å	R_A Å	R_{RMS} Å	σ Å
Bare Si	-	0.6	0.9	0.7
Thermal Oxide	5300	2.3	2.9	1.8
LSN	440	4	5.4	3.6
LSN	2300	41	52	32
LTO	12000	12.2	16	10
LTO - Annealed	12000	12.4	16	10
Membrane - LTO	-	15	20	13
Membrane - thermal oxide	-	4.6	5.8	3.5
Membrane - 1993	-	9	10	4.4
Membrane - 2006 back	-	22	30	20
Membrane - 2006 front	-	118	149	91

Table A.1: Summary of film roughness results. Film thicknesses were measured by reflectometry. Roughnesses were determined from the analysis of AFM images. All of the membrane roughnesses were measured on the back surface of the membrane unless otherwise noted.

During the thermal oxidation process oxygen diffuses into the polished silicon wafer which consumes the surface of the silicon wafer whereas the LTO likely has an island growth mechanism as the gaseous species react on the substrate surface depositing SiO_2. The two films differs in roughness by a factor of ten. Annealing the LTO at 1000°C has no effect on the roughness. The LSN films are also an island growth mechanism with thicker films having larger surface roughness.

Comparing the roughness of the oxide to the back surface of the released membrane it is clear that the membrane roughness is the result of the oxide underlayer acting as a template for the nitride deposition. The roughness data listed in the table are only for the uniform regions on the back of the membrane. The membranes grown directly on Si or on the thermal oxide have large areas of low roughness but also have deep pits that are $\sim 40 - 400$Ådeep that are not seen on the LTO underlayer films. This pitting is either due to the formation of H_2 bubbles under the LSN during growth or the pits form during the etching in either KOH or BHF. Comparison of the front and back surfaces of the membrane show that the front surface is much rougher than the back which suggests that the LSN is weakly etched by the KOH. The front surface is exposed the KOH for ~ 8 hours where as the back surface is only etched for ~ 30 minutes if there is no oxide underlayer. If there is an oxide layer then the back surface is never exposed to KOH but it is exposed to BHF during the oxide etch. LSN is known to have a low etch rate in BHF [127]. Comparing the front and back surfaces of the membrane from 2006 which did not have an oxide layer it is clear that some of the etching happens very rapidly. A controlled study of the etch rates of LSN in BHF and KOH will clarify the large discrepancies in the membrane surface roughnesses.

A.4 Conclusions

We have found that the surface roughness of LSN membranes depends on the choice of oxide underlayer and details of the etchants during the release of the membrane. This information is important for applications where smooth interfaces are required such as multilayers [128] or epitaxial growth after the deposition of a crystalline template layer using ion beam assisted deposition [129].